



저작자표시-변경금지 2.0 대한민국

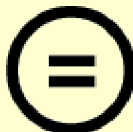
이용자는 아래의 조건을 따르는 경우에 한하여 자유롭게

- 이 저작물을 복제, 배포, 전송, 전시, 공연 및 방송할 수 있습니다.
- 이 저작물을 영리 목적으로 이용할 수 있습니다.

다음과 같은 조건을 따라야 합니다:



저작자표시. 귀하는 원 저작자를 표시하여야 합니다.



변경금지. 귀하는 이 저작물을 개작, 변형 또는 가공할 수 없습니다.

- 귀하는, 이 저작물의 재이용이나 배포의 경우, 이 저작물에 적용된 이용허락조건을 명확하게 나타내어야 합니다.
- 저작권자로부터 별도의 허가를 받으면 이러한 조건들은 적용되지 않습니다.

저작권법에 따른 이용자의 권리와 책임은 위의 내용에 의하여 영향을 받지 않습니다.

이것은 [이용허락규약\(Legal Code\)](#)을 이해하기 쉽게 요약한 것입니다.

[Disclaimer](#)



공학박사학위논문

Mechanical and Electrochemical
Behavior of Silicon Anode for
Li-ion Batteries on Soft Substrate

유연기판상에서의 리튬이차전지용
실리콘 음극전극의 기계적, 전기화학적
거동에 관한 연구

2014년 8월

서울대학교 대학원

재료공학부

정민석

유연기판상에서의 리튬이차전지용 실리콘 음극전극의 기계적, 전기화학적 거동에 관한 연구

MECHANICAL AND ELECTROCHEMICAL BEHAVIOR OF SILICON ANODE FOR LI-ION BATTERIES ON SOFT SUBSTRATE

지도교수: 주영창

이 논문을 공학박사 학위논문으로 제출함

2014년 8월

서울대학교 대학원

재료공학부

정민석

정민석의 박사학위 논문을 인준함

2014년 7월

위 원 장 할 흥 남 (인)

위 월 강 기 석 (월)

위 월 죄 일 석 (으)

ABSTRACT

Mechanical and Electrochemical Behavior of Silicon Anode for Li-ion Batteries on Soft Substrate

Min-Suk Jung

Department of Materials Science and Engineering

The Graduate School

Seoul National University

Nowadays, there is an increasing demand for full bendable and wearable electronic devices. To meet this need, soft substrate is a promising candidate for those next-generation electronics. For miniaturization and high integration of current device, high-capacity electrode materials are necessary for operation of those devices. Among many active materials for anode electrode, alloying types (Si, Sn, Ge, As, Al, etc) are widely known due to their high gravimetric and volumetric capacity than any other electrodes. However, these alloying types of anode materials undergo large volume expansions, inducing huge internal stress. This intrinsic stress lead to mechanical degradations of the electrodes and decaying the drastic capacity fading. When the electrodes were subjected to mechanical deformation, such as bending, twisting, and stretching, the electrodes shows fatal failures. Therefore, relieving these intrinsic and extrinsic stress become very important to improve the performance of alloying type anodes for the bendable Li-ion batteries.

In this study, we have introduced novel designs of Si anode to overcome the two main limitations of Si: largest volume expansion and brittle nature. This is because, if the drawbacks of Si can be solved, any electrode can be employed. From the fundamental understandings of Si thin film anode during charge and discharge process, we first observed certain mechanical failures (buckle, delamination) of the thin-film-type Si anode on soft substrate, which resulted in rapid capacity decay. Post analysis of the buckles led us to estimate the interface toughness of lithiated Si, which were 6.52 ± 0.14 J/m² from circular buckles and 5.89 ± 0.27 J/m² from telephone cord buckles.

To improve the adhesion strength between Si and Cu, as well as to relieve the intrinsic and extrinsic stress, we introduced a nano-hairy structure on a polyimide (PI) substrate and successfully developed a robust Si anode electrode for PI-substrate-based Li-ion batteries. Through *in-situ* SEM observation, we elucidated the working mechanism of the nanostructured amorphous Si anode. A direct lithiation process revealed that, the stress due to Si volume expansion was released via the inter-spacing between the nano-hairy Si anodes and by the compliant nature of the polymer nanowire. Subsequently, using a coin-cell test, the nano-hairy Si anode exhibited a much longer cycle life and higher capacity (1573 mAh/g at 100th cycle). In the C-rate test, outstanding response and high capacity recovery (when returning to the initial current value) from a high rate charge/discharge test was obtained to compare with a Si thin-film electrode. Solid-electrolyte-interphase (SEI) was found to form over the nano-hairy Si, and to release the internal stress, cracks appeared in the SEI with very uniform crack length below the critical delamination length, thereby, further delaminations were prevented.

For flexible and bendable applications, we also evaluated mechanical resistance to cyclic sliding for a current collectoor and cyclic bending for a full-pouch battery. Cu on nano-hairy PI showed extremely low change (<10%) in electrical resistance up to

500,000 cycles, whereas Cu on pristine PI showed over 300% change. With a full-pouch battery, we successfully turned on the back light unit and maintained 3.7 V under 3000 bending cycles on a 12.7 mm-bending radius. Even, excellent C-rate was also observed under the bent state.

For further study of electrochemical and electrical properties, we introduced O₂ gas, and successfully obtained very thin and long nano-hairy PI. Using this structure, we were able to improve the electrochemical performance, higher capacity and excellent rate capability due to the larger surface area. In cyclic bending fatigue test for Cu current collector, O₂-nano-hairy Cu showed lower change in electrical resistance than both CF₄-nano-hairy and pristine PI under 4% strain condition. We also introduced graphene oxide (GO) dispersed conductive polymer composites to replace the Cu current collector. From the results of electrochemical test, Si on nano-hairy conductive PI showed the typical capacity of Si in the lower C-rate region. These results can suggest the potential of fabric or polymer (with low conductivity) based Li-ion battery system to understand the limit of the charge or discharge current.

This study demonstrated the direct integration of Si anode on a polymer substrate for bendable Li-ion battery and attempted to address all of the challenges of Si by designing a core-shell Cu/a-Si nano hairs. One aspect that stands out is the ability to use bendable polymer substrate to integrate any active electrodes. We believe that our study would widen the choice of the materials and open up the option of using polymer substrate-based bendable batteries.

Keywords: Si anodes, bendable batteries, bending fatigue, polymer nanostructures, interface toughness

Student Number: 2008-22861

Table of Contents

Abstract.....	i
Table of contents.....	v
List of Tables.....	viii
List of Figures.....	ix

Chapter 1. Introduction

1.1. The need for bendable Li-ion batteries on soft substrate	1
1.2. Reliability issues in bendable batteries	4
1.2.1. Intrinsic stress due to volume expansion	7
1.2.2. Extrinsic stress due to bending deformation	11
1.3. Objective of the thesis	12
1.4. Organization of the thesis	15

Chapter 2. Theoretical Background

2.1. Electrochemical and mechanical properties of silicon during charge/discharge	16
2.1.1. Lithiation of silicon	18
2.1.2. Delithiation of silicon	23
2.2. Mechanical failure in thin film	25

2.2.1. Energy release rate and Griffith criterion	25
2.2.2. Nucleation and growth of buckles in thin films	30
2.2.2.1. Circular buckle	35
2.2.2.2. Linear/nonlinear buckle	35
2.2.3. Nucleation and growth of cracks in thin films	41
2.2.3.1. Minimum crack spacing	43
2.2.3.2. Critical delamination length	45
2.2.3.3. Mechanical failure due to fatigue	51

Chapter 3. Electrochemical and mechanical behavior of Silicon thin film anode on soft substrate

3.1. Introduction	53
3.2. Experimental procedure	54
3.3. Results	60
3.3.1. Material characteristics of Si	60
3.3.2. Failures of Silicon film after first lithiation	62
3.3.3. Interface toughness of lithiated Silicon	66
3.4. Summary	75

Chapter 4. Electrochemical and mechanical behavior of nano-hairy Silicon anode on soft substrate

4.1. Introduction	76
4.2. Fabrication of nano-hairy Silicon	78
4.3. Experimental procedure	86
4.4. Results	93

4.4.1. <i>In-situ</i> lithiation of nano-hairy Silicon	93
4.4.2. Improvement of electrochemical performance	99
4.4.3. Improvement of electrical stability	112
4.4.4. Improvement of mechanical stability	113
4.5. Summary	127
Chapter 5. Engineering of soft substrate	
5.1. Introduction	128
5.2. Geometric modification of nano-hairy structure	129
5.2.1. Enhancement of electrical stability	132
5.2.2. Enhancement of electrochemical performance	137
5.3. Electrical modification of soft substrate	145
5.3.1. Enhancement of electrochemical performance	148
5.4. Summary	153
Chapter 6. Conclusion	
6.1. Summary of results	154
6.2. Future work and suggested research	157
References	158

LIST OF TABLES

- Table 1.1** Various methods for the synthesis of Si nanowires
- Table 2.1** Commonly observed crack patterns with a dimensionless driving force Z^{68}
- Table 3.1** Various kinds of soft substrates and their detail specifications.
- Table 3.2** Onset stress and interface toughness of circular and telephone cord buckles.
- Table 3.3** Values of interface toughness between Si and Cu

LIST OF FIGURES

- Figure 1.1** Wearable and bendable electronic devices based on soft substrates. To run these devices, electrochemical and mechanical stabilities are required.
- Figure 1.2** (a) A simplified Ragone plot for various energy storage domains
(b) specific power versus specific energy of rechargeable energy storage devices
- Figure 1.3** Gravimetric and volumetric capacities of various active anode materials
- Figure 1.4** (a) Stress evolution by volume-change induced-intrinsic stress and mechanical-deformation induced-extrinsic stress
- Figure 1.5** List of conducted studies to minimize the mechanical degradations through designing of nano-structure Si anodes and fabrication of Si anodes below the critical failure size
- Figure 2.1** A phase diagram of Li with Si. Five distinct silicide phases LiSi , $\text{Li}_{12}\text{Si}_7$, Li_7Si_3 , $\text{Li}_{13}\text{Si}_4$ and $\text{Li}_{22}\text{Si}_5$ have been observed

Figure 2.2 (a) The first galvanostatic lithiation curve of SiNW (b) Phase transformation of crystalline Si during lithiation.

Figure 2.3 (a) Charge and discharge curve between 1.2 and 0.01 V vs. Li/Li⁺ at C/4 (b) Stress in the Si thin film (250 nm) calculated from the substrate curvature by Stoney equation via MOS technique

Figure 2.4 Surface morphologies after 30 cycles. (a) 250 nm-thick Si film (b) 1 μm -thick Si thin film (c) Cracking does not directly cause any capacity decay from a 250 nm-thick Si film. However, rapid capacity decay was seen for a 1 μm Si thin film due to delamination of the film²²

Figure 2.5 (a) The first galvanostatic delithiation curve of SiNW (b) Phase transformation from crystalline Si to amorphous phase during lithiation.

Figure 2.6 A through-the-thickness crack in an infinitely wide plate subjected to a remote tensile stress

Figure 2.7 (a) Edge delamination and (b) Buckle delamination with the minimum flaw sizes necessary to debond the film from the substrate

Figure 2.8 Various buckle configurations (a) Circular (b) Straight-sided, and (c) Telephone-cord buckle

Figure 2.9 A schematic of thin film shape (a) under the pre-stress, σ_0 , and (b) under the resultant stress, σ . Buckle configurations lead to delamination between the film and the substrate.

Figure 2.10 The geometry parameters in straight buckle

Figure 2.11 Buckle configurations from straight (left), varicose (middle), and telephone-cord (right). Bifurcation is determined from the Poisson's ratio and σ_c/σ_0 using the finite element code, ABAQUS.

Figure 2.12 Buckle configurations from straight (left), varicose (middle), and telephone-cord (right). Bifurcation is determined with a Poisson's ratio and σ_c/σ_0 using the finite element code, ABAQUS.

Figure 2.13 Dimensionless groups of system parameters, $\frac{\sigma_m^2 h_f}{E_f \Gamma_f}$ is plotted as a function of Γ/Γ_f with Γ/Γ_s (<0.26 : upper, >0.26 : lower) For $D_l=0$ (Dundurs parameter, $D_l = \frac{\overline{E}_f - \overline{E}_s}{\overline{E}_f + \overline{E}_s}$), the Γ/Γ_s ratio is approximately 0.26)

Figure 2.14 A comparison between no interfacial sliding model and interfacial sliding model.

Figure 2.15 Changes in elastic energy in the Si film and surface energy as a function of the crack a with respect to l

Figure 2.16 Illustration of crack initiation and propagation regimes with three different region by plotting da/dn versus $\log^{\Delta}K$

Figure 3.1 The relation from equation (3.1) between (a) substrate and film thickness with bending radius (b) ideal range for the aim of this research

Figure 3.2 Deposition sequence of Cu and Si for the battery anode system. Surface morphology is below the schematics captured by FE-SEM

Figure 3.3 Coin-cell assembling. Cu (200 nm) was deposited onto the PI substrate, and Si (300 nm) was subsequently deposited using a metal mask with an area of 1 cm^2 . Cu tape was used to attach the sample and electrically connect the same with the coin cell.

Figure 3.4 (a) XRD pattern of the deposited thin film on PI substrate, (b) XPS studies of the thin film before (black) and after (red) sputtering.

Figure 3.5 (a) Failure morphologies of lithiated Si after lithiation. Telephone cord and circular buckle are observed. (b) Discharge profile of Si thin film down to 0.001 V (c) quantitative stress study of Si thin film during cycling.

Figure 3.6 Cross-sectional view of a telephone cord buckle sectioned by FIB technique. (a) the interface between lithiated Si and Cu layer (b) enlarged image of (a). The Pt (protecting layer) was re-deposited during FIB sectioning. The Cu and lithiated Si is clearly separated by compressive stress.

Figure 3.7 Measurements of different parameters— (a) radius of circular buckle and (b) thickness. (c) width of telephone cord buckle and (d) thickness

Figure 3.8 Delamination of Si thin film after lithiation. EDS analysis of Cu, C, and Si. Si is mainly peeled off from Cu layer. However, Cu is well attached onto the PI substrate.

Figure 4.1 (a) Schematic design of the dense and pliable nano-hairy structures on a polyimide substrate. Cartoon schematics of the Si-coated polyimide nanowires (PINWs) (b) before lithiation and (c) after lithiation. (d) The delamination of SiNWs due to mismatch between SiNWs and the current collector during charging/discharging. (e) The partial breaking of SiNWs by crack initiation and propagation. (f) The long travelling distance of an electron from the Si NWs to the current collector.

Figure 4.2 Schematic of plasma-enhanced CVD (PECVD) mechanism (a) Formation of residues. (b) a real equipment during etching process

Figure 4.3 Various nanostructures from (a) Si wafer (b) polystyrene bid (c) polyimide substrate

Figure 4.4 Direct integration of nano-hairy Si anode on a nanorod array polymer substrate: (a) Pristine PI substrate before CF₄ etching, (b) Well-arrayed PI nano-hairy structures after CF₄ PECVD etching on pristine PI, (c) Cu (200 nm) as the current collector deposited by thermal evaporation, (d) Si deposited (300 nm) as the active material by thermal evaporation on the sample (c), (e) A cross-sectional image of sample (c), and (f) A cross-sectional image of sample (d), both prepared by FIB cutting after Pt coating

Figure 4.5 (a) *In-situ* manipulator in the chamber providing SEM and FIB function. (b) Freely moving probe by a controller to all of the directions.

Figure 4.6 **Figure 4.6.** (a) Image of bending fatigue equipment (b) Free diagram: sliding motion of the metal thin film on PI (c) Applied strain and sequence by the sliding motion in the regions A,B, and C

Figure 4.7 Full-cell assembling. (a) Dimension of cathode and anode electrode (b) Full packaging battery with Si anode and NCA cathode, assembling process is co-operated with ROCKET ELECTRONIC Inc.

Figure 4.8 (a) Bending fatigue test using a supporting steel bar. Non-bending state (left) and bending state (right). (b) Schematic image of bending and non-bending state of a full battery

Figure 4.9 *In-situ* investigation of the lithiation process of *In-situ* Si lithiation test on nano-hairy PI through contact with bulk Li, (a) before Si lithiation and during the process of lithiation (b)-(f).

Figure 4.10 Schematic images and pictures of (a) before lithiation (b) after lithiation. Dimensional change in length during the lithiation process by the contact-lithiation method. We observed increased Si on the tip of the nanorod from the top view (represented by black dots) (c) before and (d) after the lithiation test and edited these images using an image analyzer. For selected round and independent Si heads, the change in diameter was measured.

Figure 4.11 (a) In-situ lithiation test of nano-hairy Si. Si is expanded one by one from #1 to #3 for 19 seconds. (b) Literature values of diffusivity of Li^+ in amorphous Si. The current result is comparable with the reported values.

Figure 4.12 Coin-cell test: (a) Capacity on delithiation step of Si on pristine and nano-hairy PI tested using a half-cell, and surface morphologies after the first lithiation test and EDS mapping results (b) on pristine PI with buckles (i and ii) and Si delamination of the Si film (iii) and (c) on a nano-hairy PI

Figure 4.13 Discharge capacity of (a) Si on nano-hairy PI, (b) thin-film Si on Cu foil and (c) thin-film Si on pristine PI up to 140 cycles.

Figure 4.14 (a) A rate capability test and (b) charge/discharge profiles (of the last cycle at the same C-rate) at various C-rates for the Si on nano-hairy PI. (c) A rate capability test and (d) charge/discharge profiles (of the last cycle for the same C-rate) at various C-rates for the Si on pristine PI.

Figure 4.15 First and second charge-discharge profile of Si. The lithiation potential has a sloping profile between 0.1 and 0.01 V, reflecting the behavior of amorphous silicon. A plateau was also observed at approximately 0.4 V at the first discharge graph, corresponding to SEI layer formation.

Figure 4.16 Morphology observation after the rate capability test. (a) A SEI layer (dark green) covers the polymer/Si core/shell structures without any delamination events on the nano-hairy PI substrate. (b) The Si film was severely peeled off, and the exposed Cu layer (yellow) was wider than the Si islands, thus indicating a loss of active material.

Figure 4.17 A rate capability comparison of electrochemical and mechanical responses with the pouch-cell batteries made of a nano-hairy Si anode (orange) and a thin film Si anode (navy) on PI substrates.

Figure 4.18 Electrochemical impedance spectroscopy (EIS) results for Si on nano-hairy PI (orange square) and Si on pristine PI (navy circle) (a) in a high frequency region and (b) low frequency region.

Figure.4.19 Change of electrical resistance versus number of cycles in a bending fatigue test of Cu on pristine PI and on nano-hairy PI.

Figure 4.20 (a) Cracked surface of SEI/Si body and EDS mapping results of Cu and Si after the lithiation test. No delamination of Cu and Si was detected (b) SEI covered nanostructured Si (SEI/Si body) on the Cu layer by filling the free space above the Si nano-hairs and covering trend illustrated with a schematic image (inset) (c) compositional analysis of SEI/Si body

Figure 4.21 Delamination of nano-hairy Si after lithiation. EDS analysis of Cu, C, and Si. Cu is mainly peeled off from PI substrate. Si is well attached onto the PI substrate unlike the Si on pristine PI

Figure 4.22 (a) Uniform crack initiation on Si on nano-hairy PI. Thick SEI layer covers the entire surface. No delamination had occurred because the average crack length was below the critical delamination length ($105.8 \mu m$). However, onset of delamination was observed when the crack length was above the critical delamination length.

Figure 4.23 (a) A back light unit (BLU) was kept on during the bending cycles of the bendable pouch cell battery in which the nano-hairy Si anode was used as an anode and (b) the voltage of the pouch cell battery, which was maintained at 3.74 volts during non-bending (left) and bending (right) cycles.

Figure 4.24 (a) Bending fatigue test using a supporting steel bar (b) voltage retention test during a cyclic bending fatigue test at 1 Hz. A full cell using a Si on pristine PI maintains the voltage at 3.7 without bending fatigue (inset)

Figure 4.25 (a) Plot of discharge capacity per unit area (left y-axis) and per weight (right y-axis) versus cycle number of Si (300 nm) on the nano-hairy PI in a full pouch-cell at various C-rates. Charge and discharge was conducted from 3.0 to 3.9 V (b) under the bending status on a steel bar ($R_c=12.7$ mm)

Figure 5.1 Tilted and top morphology of nano-hairy PI fabricated by CF_4 gas plasma etching process (left column) and by O_2 gas plasma etching process (right column)

Figure 5.2 Cu deposition on (a) pristine PI (b) CF_4 -nano hairy PI (c) O_2 -nano hairy PI

Figure 5.3 Results of bending fatigue test under 2% strain of (a) Cu on pristine PI, CF_4 -nano hairy PI and O_2 -nano hairy PI (b) enlarged graph of CF_4 -nano hairy PI and O_2 -nano hairy PI

Figure 5.4 Results of bending fatigue test under 4% strain of Cu on CF₄-nano hairy PI and O₂-nano hairy PI

Figure 5.5 Images of Si on Cu coated (a) O₂-nano hairy PI (b) CF₄-nano hairy PI and (c) pristine PI

Figure 5.6 Rate capability test of Si on O₂-nano hairy PI, CF₄-nano hairy PI and pristine PI with a half-cell.

Figure 5.7 Plot of capacity vs C-rate for various types of SiNWs

Figure 5.8 Rate capability test of Si on O₂-nano hairy PI, CF₄-nano hairy PI and pristine PI with a full-cell.

Figure 5.9 EIS results of Si on O₂-nano hairy PI, CF₄-nano hairy PI and pristine PI with a full-cell

Figure 5.10 Graphene oxide (GO) dispersed in conductive polymer composites.

Figure 5.11 (a) conductive PI having different conductivity controlled by GO (b) conductivity of various materials and conductive PI with different GO portion.

Figure 5.12 (a) Nano-hairy PI/GO (20 wt.%) by CF₄ plasma etching (b) Si deposition on (a) (c) Nano-hairy PI/GO (30 wt.%) by CF₄ plasma etching (d) Si deposition on (c)

Figure 5.13 (a) Rate capability test for Si on nano-hairy PI/GO (20 wt.%) and PI/GO (30 wt.%) by CF₄ plasma etching (b) sheet resistance of both the samples

Figure 5.14 Surface morphologies after lithiation of (a) Si on nano-hairy PI/GO (20 wt.%) and PI/GO (30 wt.%).

CHAPTER 1

Introduction

1.1. The Need for bendable Li-ion batteries on soft substrates

When designing of fully flexible electronics is almost impossible to achieve with hard substrates, such as rigid wafer-based substrates,¹⁻³ soft substrates come as the most promising solution to this problem and at the same time, to meet the demands for the next generation electronic devices. Nowadays, there is an increasing demand for bendable, lightweight and cost-effective polymer substrate-based electronics. However, such full bendable and wearable electronic devices, e.g. RFID tags, smart chip cards, e-paper, and biomedical circuits,⁴⁻⁶ should be met with stable power sources and highly reliable mechanical stability as shown in Figure 1.1.

There are many types of energy storage devices from capacitors to fuel cells (Figure 1.2), used for various levels of powering, e.g. watches (0.1-0.5 Wh), mobile phones (2-4 Wh), laptop computers (30-100 Wh), electric vehicles, such as cars (5-10 kWh) or buses (~100 kWh) and uninterrupted power supply (UPS) for a city (~MWh).⁷ Among them, rechargeable lithium ion batteries (LIBs) are widely used due to their high operating voltage, high energy density, long-term cycling life, and no side effects,

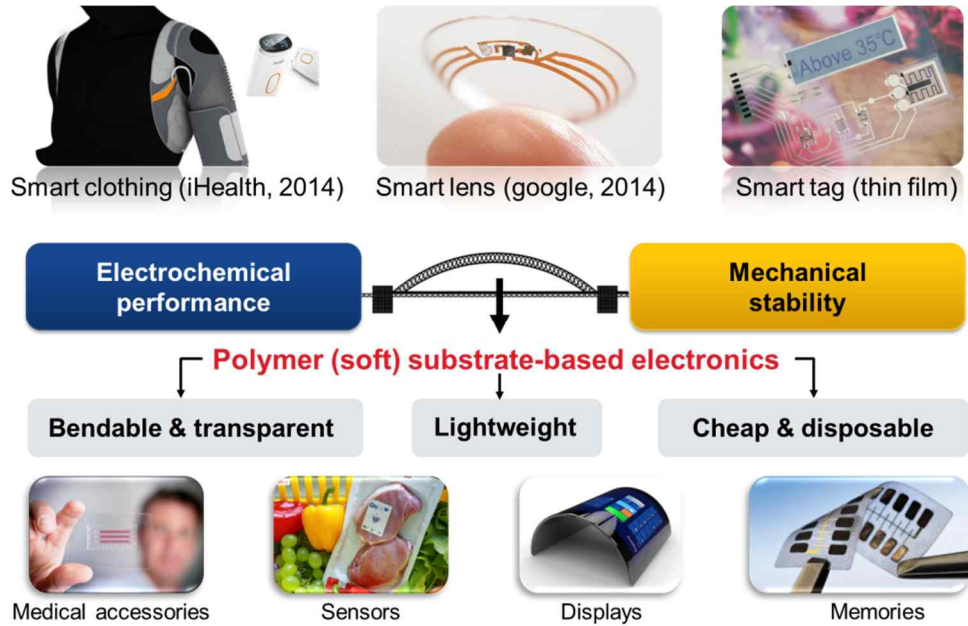


Figure 1.1. Wearable and bendable electronic devices based on soft substrates.

To run these devices, electrochemical and mechanical stabilities are required.

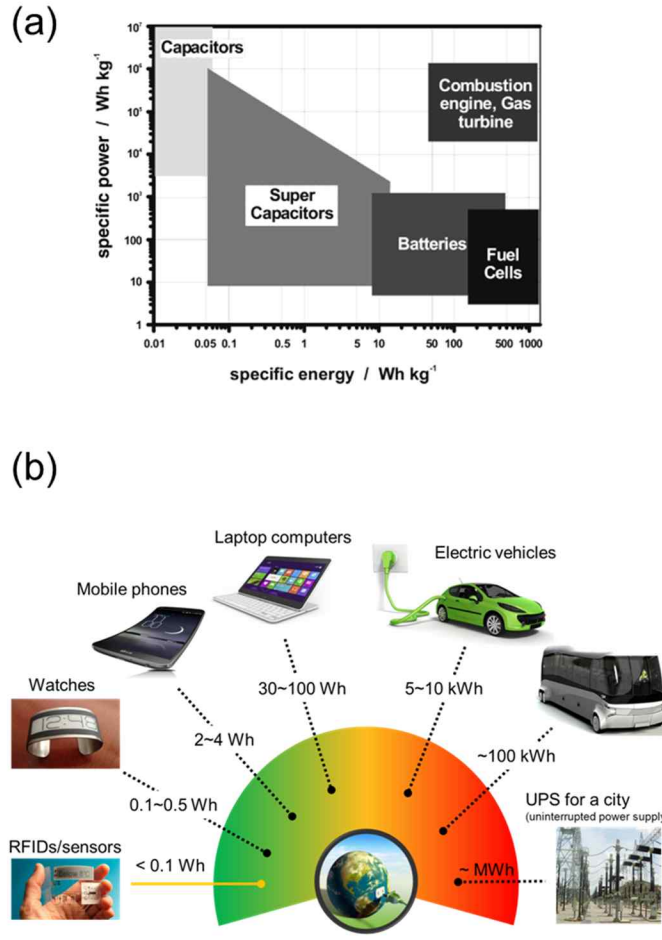


Figure 1.2. (a) A simplified Ragone plot for various energy storage domains ^{8,9}
 (b) large range of stored energies in batteries⁷

such as memory effect, and large discharge rate. Thus, LIBs are very appropriate for the next-generation bendable electronics.^{7,10} Recently, carbon based nanotubes,^{11,12} metal oxide-based nanowires,¹³ slurry-typed composites,¹⁴ and graphene¹⁵ have been extensively associated with flexible LIBs.

1.2. Reliability issues in bendable batteries

Miniaturization and high integration of electronic components to form modern all-in-one devices have called for embedded systems and Li-ion batteries embedded in a polymer substrate may expand the horizons of bendable devices. However, due to a limited space for the batteries, high-capacity electrode materials are essentially needed (Figure 1.4). Among several active materials for anode electrode, the alloying types (Si, Sn, Ge, As, Al, etc) are widely popular due to their higher gravimetric and volumetric capacities than those of other electrodes types, viz. insertion and conversion types (Figure 1.3). These alloying types of anode materials have a large volume expansion coefficient and therefore, induces a huge internal stress, which causes mechanical degradation of the electrodes and drastic capacity fading

When LIBs are subjected to any mechanical deformation, such as bending, twisting, and stretching, externally induced stress is generated, which causes damage to the batteries. It is not only the active materials but also the current collector layer become prone to cracks and delaminations, resulting in a change of electrical resistance. Therefore, reducing both intrinsic and extrinsic stress is very important to improve the performance of LIBs for bendable electronics. In the current work, Si anode material has been selected due to its largest volume expansion and brittle nature. If the drawbacks of Si can be overcome, it can be used for any electrode.

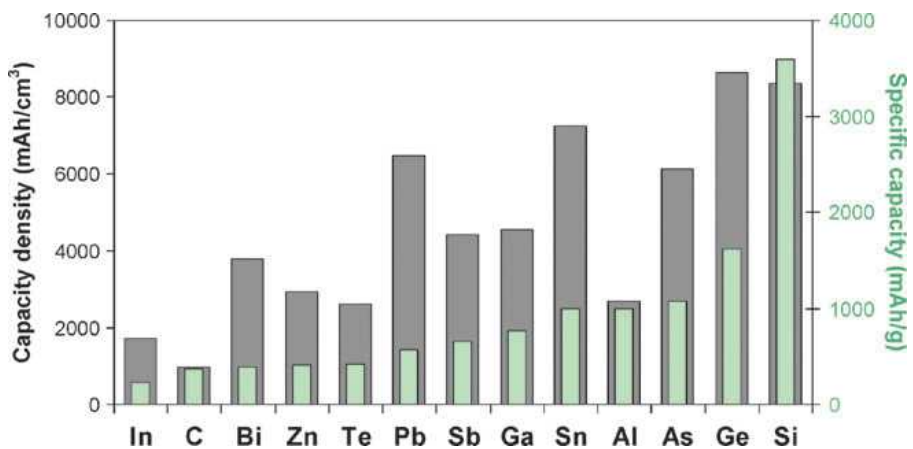


Figure 1.3. Gravimetric and volumetric capacities of various active anode materials⁷

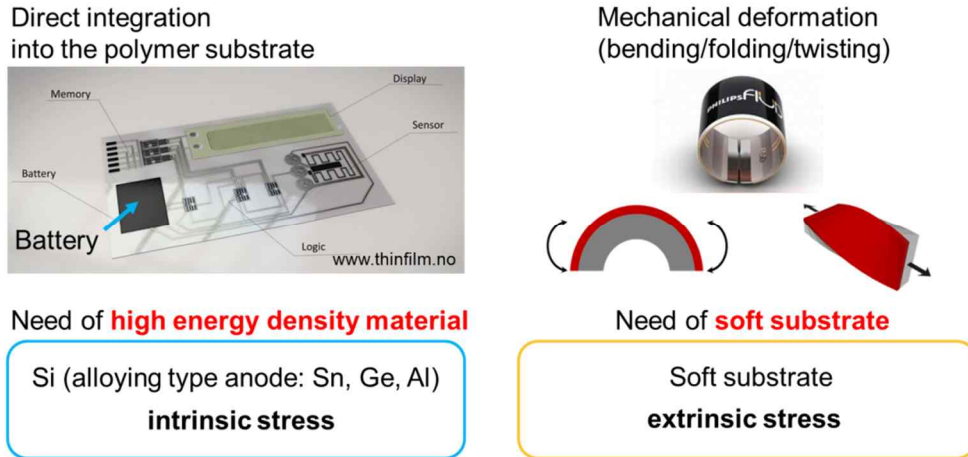


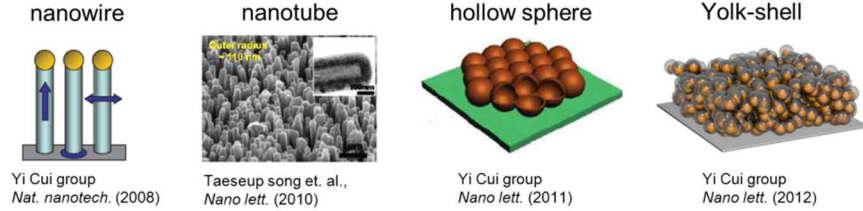
Figure 1.4. (a) Stress evolution by volume-change induced-intrinsic stress and mechanical-deformation induced-extrinsic stress

1.2.1. Intrinsic stress due to volume expansion

As mentioned earlier, high capacity materials exhibit large volume expansions in contrast to the commercially used carbon-based electrodes.^{16–18} Especially, Si anodes experience catastrophic failures during charge/discharge cycles. Si exhibits severe mechanical degradation (e.g. cracks, delamination) due to the accumulated stress caused by large volume expansion, which can be as high as 300 % upon full lithiation,^{19,20} thereby resulting in a fatal capacity decay and a short cycle life.^{21,22} Serious reliability issues, such as the acute delamination of the Si thin-film anodes on polymer substrates, can be even more severe, when compared to Si thin films on metal (e.g. Cu) current collector. In an attempt to overcome the mechanical instability of Si, various Si nanostructures, such as simple nanowires (NWs), core/shell NWs, coated NWs, embedded NWs and nanotube NWs^{23–28} have recently been explored. Such nanostructures, through their critical size effects, have been proved efficient in releasing any strain that develop from free expansion, and also impart fracture resistance through critical size effects in (Figure 1.5).^{29–32} However, designing of these nanostructured Si anodes on PI substrates is extremely challenging due to difficulties in their direct integration onto polymer substrates. One such difficulties is to use polymer based substrates at high temperature (say, between 300 to 1000 °C), which is the typical temperature range for the syntheses of the Si NWs via standard methods, viz. vapor-liquid-solid (VLS), supercritical fluid-liquid-solid (SFLS) or solution-liquid-solid (SLS) growth,^{33–35} as summarized in Table 1.1. In the current work, a nano-hairy Si electrode was directly fabricated onto the PI substrate. To demonstrate the lithiation mechanism of the unique nano-hairy structure an *in-situ* lithiation test was conducted, which facilitated not only the kinetic lithiation process but also the strain accommodation

process. Furthermore, using a button-cell battery test and a bendable pouch cell battery test, we demonstrated that our new electrode design significantly improved the cycling and rate performance of the battery, as well as successfully overcame the aforementioned fatal issues of the Si anode integrated onto a polymer substrate.

▪ Nano-structure for strain accommodation by free space



▪ Below the critical failure size

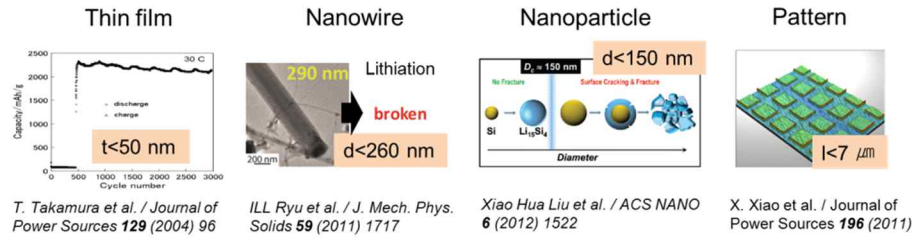


Figure 1.5. List of conducted studies to minimize the mechanical degradations through desinging of nano-structure Si anodes and fabrication of Si anodes below the critical failure size

Table 1.1. Various methods for the synthesis of Si nanowires

Method	Temperature	Sub.	Crystallinity	Reference
VLS (CVD)	300~1000 °C	Metal	Crystalline	V. Schmidt et al., <i>Chem. Rev.</i> (2010)
Supercritical fluid-liquid-solid (SFLS)	363 °C for Au	Metal	Crystalline	Korgel et al., <i>Science</i> (2000)
Solution-liquid-solid (SLS)	~ 450 °C	Metal	Crystalline	Korgel et al., <i>J. Am. Chem. Soc.</i> (2008)
Metal-assisted wet chemical etching (MaCE)	RT	Si sub.	Crystalline	K.-Q. et al., <i>Adv. Mater.</i> (2002)
Electrodeposition	RT	Metal	Amorphous	Mallet et al. <i>Nano lett.</i> (2008)
Deep reactive ion etching (DRIE)	RT	Si sub.	Crystalline	Y. Cui et al., <i>Appl. Phys. Lett.</i> (2008)
Spray coating	Annealing (363 °C)	Carbon textiles	Crystalline	Bin Liu et al., <i>Scientific Reports</i> (2013)

1.2.2. Extrinsic stress due to bending deformation

As shown in Fig. 1.4, LIBs can be deformed via bending, twisting, and stretching by external force. A large amount of stress starts to accumulate from the very beginning of the deformation,¹⁰ and this extrinsic stress can damage the current collector layer on soft substrate through cyclic deformations, resulting in an increase in the resistance. Even, electrochemical performance can also be deteriorated. Si has been actually used for bendable devices but not for bendable batteries. Bulk Si may not be an ideal material for bendable devices due to its brittleness under bending conditions and easily becomes fractured. In contrast to bulk Si, ultra-thin Si film has extensively been used for bendable devices, for e.g. solar cells and TFTs use either thin Si films or Si ribbons on elastomeric substrates.³⁶⁻⁴¹ The thickness of the Si thin film and ribbons are between a few nanometers and tens of micrometers, Therefore, Si can be used for mechanically bendable devices. Moreover, the void space between the Si nano-hairs would further enhance the mechanical tolerance upon bending and volume expansion during the charge-discharge cycles. However, application of ultra-thin Si in bendable batteries is still under question because Si anodes should accommodate the large volume expansion during the charge/discharge cycles. We believe that our direct integration scheme using a nano-hairy structure, is applicable not only to Si but also to general electrode materials for polymer substrate-based bendable Li-ion batteries, and this strategy can facilitate the designing of full bendable and foldable devices.

1.3. Objective of the thesis

By conceptualizing and preparing a novel nano-hairy structure, this manuscript presents the inaugural trial for a new integration scheme of Li-ion battery electrodes directly onto a polymer substrate. We employed our new design concept by fabricating a high capacity nano-hairy Si anode directly onto the polyimide (PI) substrate. Utilizing both *in-situ* SEM observations and electrochemical tests, we demonstrated a significant improvement in the performance of this hybrid nanostructured Si anode, when compared with a conventional thin-film type Si electrode on a PI substrate. Moreover, we successfully demonstrated the feasibility of the pouch-cell type bendable Li-ion battery with the nano-hairy Si electrode. If we can successfully develop a new design approach for the integration of Si anodes on PI substrates without sacrificing any battery performance, the scheme can be used for any electrodes because Si is highly disfavored for its mechanical instability during charge cycles due to its extreme volume expansion. We believe that our direct integration scheme using a nano-hairy structure is applicable not only to Si but also to general electrode materials for polymer substrate-based bendable Li-ion batteries, and this strategy can facilitate a new application of bendable and foldable devices.

The key findings of our work are summarized as follows:

- For proof of concept, we designed and fabricated a unique nano-hairy Si anode using a PI substrate.
- Through *in-situ* SEM observations, we clarified the lithiation mechanism of the nanostructured Si anode, including the lithiation kinetics and the huge strain accommodation of the individual nano-hairy Si anode that improves the lithiation

kinetics and brittle nature of Si.

- Based on the electrochemical cyclic battery tests, we demonstrated that the nano-hairy Si anode achieved outstanding battery performance compared with thin-film Si on pristine PI. This unique nano-hairy structure also improved the mechanical stability, resulting in the anti-delamination of Si.
- The nano-hairy Si anode has a smaller charge transfer resistance and an easier Li⁺ ion diffusion process than that of a Si thin film on pristine PI, resulting in a higher capacity and an excellent rate capability.
- We assembled a full bendable battery to exhibit the feasibility of direct integration of the battery for practical applications for bendable electronics. Our bendable battery demonstrated very stable voltage retention under the bending fatigue endurance (3000 bending cycles at 16.0 mm of R_c with 1 Hz).
- Electrochemical performance and mechanical resistance to cyclic bending cycles were further improved via increasing the surface area and density of nano-hairy structure by using different gas etching mechanisms. Conductive polymer that uses graphene oxide (GO) was also verified for battery applications.

In broader terms, our work will also be of interest to general scientific approaches in several ways:

- This work represents a multidisciplinary study between materials science, polymer science, mechanics and battery physics, as it incorporates an advanced design and fabrication of the nanostructured hybrid materials for battery applications and utilizes state of the art *in-situ* characterization.
- Practically, in the future of mobile and wearable electronics, there will be an increased demand for bendable, lightweight and cost-effective polymer substrate-based

electronics. Following the current trend toward miniaturization and high integration of disposable and lightweight full bendable electronic devices, such as RFID tags, smart chip cards, e-paper, biomedical circuits, and smart watches, integrated rechargeable batteries for embedded systems are inevitably necessary. This meaningful work will open the door to new possibilities of imbedded energy storage for PI-based next-generation electronic devices. For the specifications, the area of the battery is below the 25 cm^2 , capacity is bounded from $4 \text{ } \mu\text{Ah/cm}^2$ to 0.2 mAh/cm^2 . Bending radius is at least below 30 mm with an over 2,000 bending cycles.

1.4. Organization of the thesis

This thesis consists of seven chapters. In chapter 2, fundamental electrochemical reactions of Si during charge and discharge processes have been explained. In addition to this, the basic fracture theory, such as crack initiation, propagation, and buckle-driven delamination events from Griffith fracture criterion have also been dealt in detail. Chapter 3 introduces experimental procedures, including sample preparation and characterizations. Failure of Si thin film and their related electrochemical performance during lithiation and delithiation steps have been shown in Chapter 4. The interface toughness of lithiated Si has also been discussed, using fracture theory in this chapter. In chapter 5, the newly designed polymer-substrate based nanostructured template was introduced, along with various results to confirm the superior performance of our new battery. Furthermore, a failure mechanism was also discussed w.r.t. fracture theory. In chapter 6, we narrated modification in the design of nano-hairy structure and the related electrical properties. Such modifications gave an insight into the improvements in Si anodes. Some useful and important results are also included in the appendices of this thesis.

CHAPTER 2

Theoretical background

2.1. Electrochemical and mechanical properties of silicon during charge/discharge

The electrochemical alloying process of Li with various Si anodes at room temperature (RT) has been investigated using Si powders⁴²⁻⁴⁴ or Si thin films.⁴⁵ From the Li-Si phase diagram,⁴⁶ 5 different intermetallic compounds were shown, LiSi, Li₁₂Si₇, Li₇Si₃, Li₁₃Si₄ and Li₂₂Si₅ (see Figure 2.1). However, at room temperature, Si does not generate any of these Li-Si silicides upon electrochemical alloying except for the formation of LiSi. Moreover, upon RT electrochemical lithiation of Si, the crystalline Si becomes amorphous.⁴⁷ Due to this Li insertion and extraction, Si experiences a large volume change upto 320%,^{19,20} resulting in a large stress development in the order of GPa within the Si anodes. As a result, mechanical degradation, such as fracture and delamination occurs inevitably, which is directly related to the cycle life and capacity decay of the Si anodes. Therefore, efficient designing of Si anode is very crucial based on the knowledge of these fundamental electrochemical and mechanical characteristics.

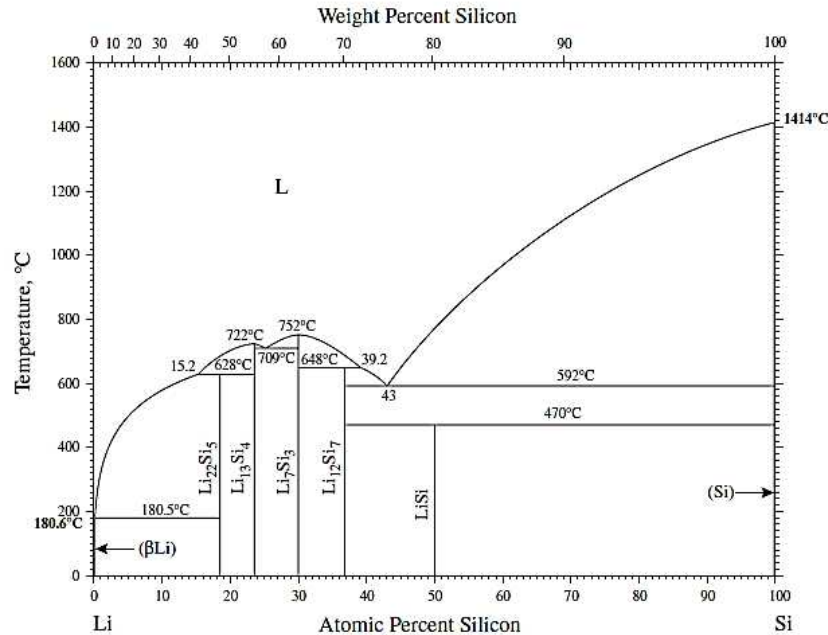


Figure 2.1 A phase diagram of Li with Si. Five distinct silicide phases LiSi, $\text{Li}_{12}\text{Si}_7$, Li_7Si_3 , $\text{Li}_{13}\text{Si}_4$ and $\text{Li}_{22}\text{Si}_5$ have been observed.⁴⁶

2.1.1. Lithiation of silicon

Upon the first lithiation of crystalline Si (c-Si), the alloying process and the discharge profile can be observed in the galvanostatic (constant current) lithiation curve of Si nanowires (SiNWs) as shown in Figure 2.2. The sloping plateau indicates a two-phase equilibrium between c-Si and amorphous a-Li_xSi.⁴⁸ From the literature^{44,49}, x=3.4~3.5 seems to be an appropriate value for a-Li_xSi. Near 60 mV (vs. Li/Li⁺), c-Si seems to be completely disappeared, and the corresponding capacity is 3350 mAh/g. If the voltage goes further down below 60 mV, a-Li_{3.5}Si turns to crystalline phase of Li₁₅Si₄, which has the highest Li content in Si at RT, and the capacity is 3570 mAh/g. This Li₁₅Si₄ exhibits a non-stoichiometrical composition, which was designated as $Li_{15\pm\delta}Si_4$ by Li and Dahn.⁴⁴ Consequently, the maximum theoretical capacity of Si at RT is ~3800 mAh/g.

In the atomic scale, a-Li_{3.5}Si and c-Si interface is controlled by breaking the Si-Si bonds during lithiation at (111) plane.⁵⁰ This breaking of the Si-Si bonds at the a-Li_{3.5}Si and c-Si interface is facilitated by high Li concentration. A high Li concentration increases the electron density and thus increases the antibonding states, resulting in a local softening effect in the Si covalent network.^{51,52} This softening effect can cause a change in modulus of a-Si, as reported by P.R. Guduru group that, biaxial modulus of Si decreases from 70 GPa to 35 GPa.⁵³

The P.R. Guduru group studied the mechanical properties of Si anode during the lithiation and delithiation process via *in-situ* multi-beam optical sensor (MOS) technique.⁵³⁻⁵⁶ They obtained compressed and tensile stress to be about 1.7 GPa and 1.75 GPa, respectively, from a 250 nm-thick Si film at a voltage range of 1.2 and 0.01 V vs. Li/Li⁺, as shown in Figure 2.3. During the Li insertion, Si thin film expands,

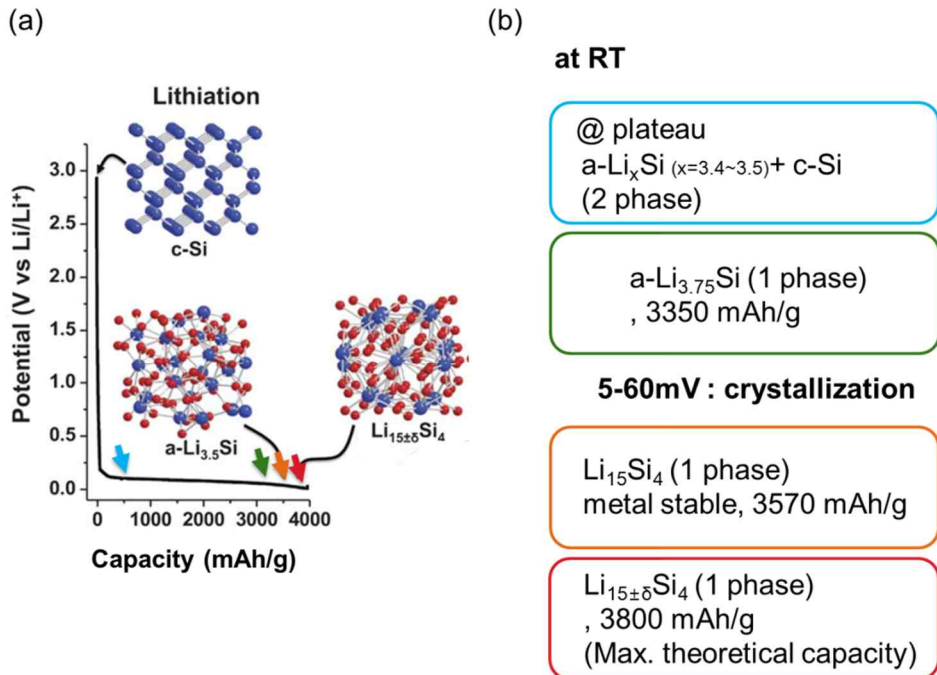


Figure 2.2 (a) The first galvanostatic lithiation curve of SiNW⁴⁸ (b) Phase transformation of crystalline Si during lithiation.

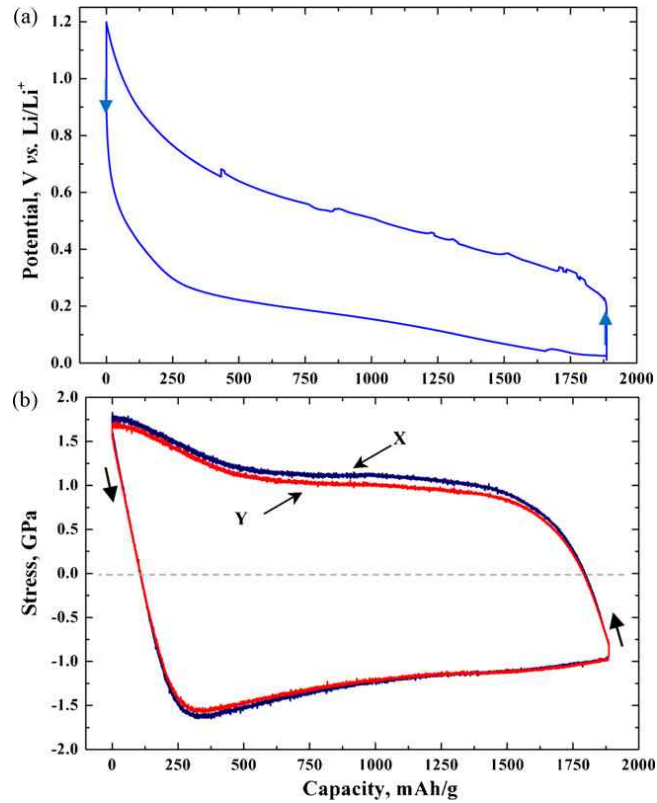


Figure 2.3 (a) Charge and discharge curve between 1.2 and 0.01 V vs. Li/Li⁺ at C/4 (b) Stress in the Si thin film (250 nm) calculated from the substrate curvature by Stoney equation via MOS technique.⁵⁴

but Cu substrate constrains its volume expansion by imparting a compressive stress. This compression is actually responsible for buckles and delaminations, which are discussed in more detail in the following chapters. Generally, delaminations cause loss of active material from the Si anode, leading to an abrupt capacity drop, as shown in Figure 2.4.

At the end of the lithiation process, the Li-Si phase undergoes a rapid crystallization to form $\text{Li}_{15}\text{Si}_4$ phase, which is not in the phase diagram.^{30,57} The structural change from amorphous Si to crystalline $\text{Li}_{15}\text{Si}_4$ affects the mechanical properties due to the formation of a phase boundary and creating micro cracks and defects. Therefore, to avoid such phase transformation, a charging limit above 50 mV seems to be a reasonable solution and maintain the performance of Si anodes.

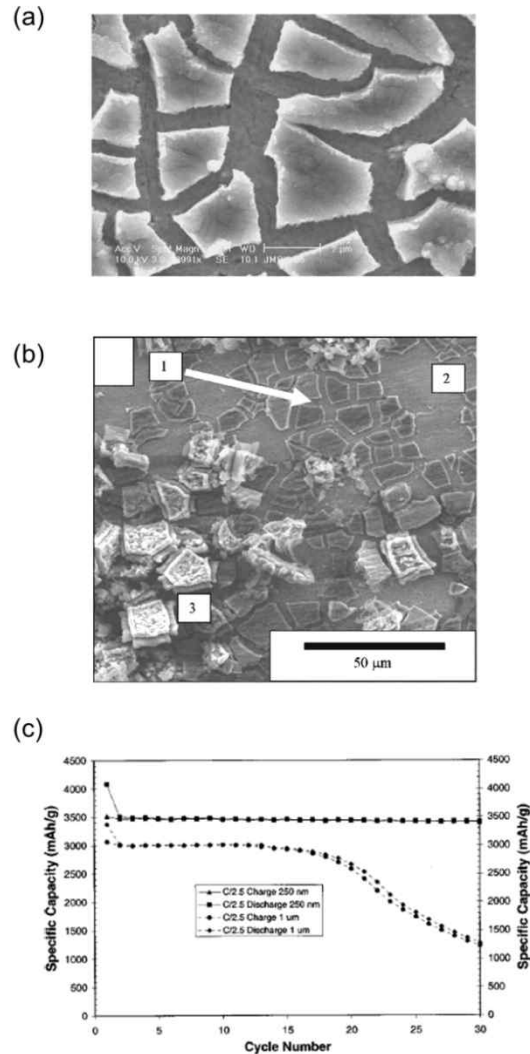


Figure 2.4 Surface morphologies after 30 cycles. (a) 250 nm-thick Si film (b) 1 μm -thick Si thin film (c) Cracking does not directly cause any capacity decay from a 250 nm-thick Si film. However, rapid capacity decay was seen for a 1 μm Si thin film due to delamination of the film²²

2.1.2. Delithiation of silicon

Upon delithiation, the $Li_{15\pm\delta}Si_4$ phase gradually disappears. Around 430 mV, $Li_{15\pm\delta}Si_4$ and a-Li_ySi ($y \sim 2$) exist on the plateau (Figure 2.5).⁴⁴ When $Li_{15\pm\delta}Si_4$ has completely disappeared, further Li extraction occurs from a-Li₂Si, resulting in a single amorphous phase a-Li_tSi ($0 < t < 2$).⁴⁴ After complete removal of Li, Si exist in the amorphous state. However, if the product of the lithiation process was amorphous a-Li_{3.75}Si, two amorphous phases (a-Li_{3.75}Si, a-Li₂Si) were obtained during the delithiation step.

After complete extraction of Li from Si, the residual plastic deformation generates a tensile stress in the Si film. As mentioned above, the overall Si-Si bond strength in the Si network becomes very low due to bond breakage. This leads to formation of through-the-thickness cracks, whose orientation of propagation is random without any preferred direction, as can be seen in fig. 2.4. The formation of these cracks is primarily based on Griffith's fracture theory and will be explained in section 2.2.3. According to the theory, a crack initiates when the release rate of elastic strain energy is at least greater than the cracking resistance force (surface energy) and the thickness below which advancement of an existing channel crack is energetically unfavorable is called the critical thickness h_{cr} . The critical thickness for Si is between 100 to 200 nm,^{30,58,59} as deduced from different cycling rates, pre-existing inhomogeneities and defects in both of film and substrate.⁶⁰

According to Juchuan Li,⁵⁹ primary cracks are unlikely to change with further cycling because the tensile stress in the thin film is not large enough during cycling to create any further new cracks. This might also be related to the minimum crack spacing theory as discussed in section 2.2.3.1

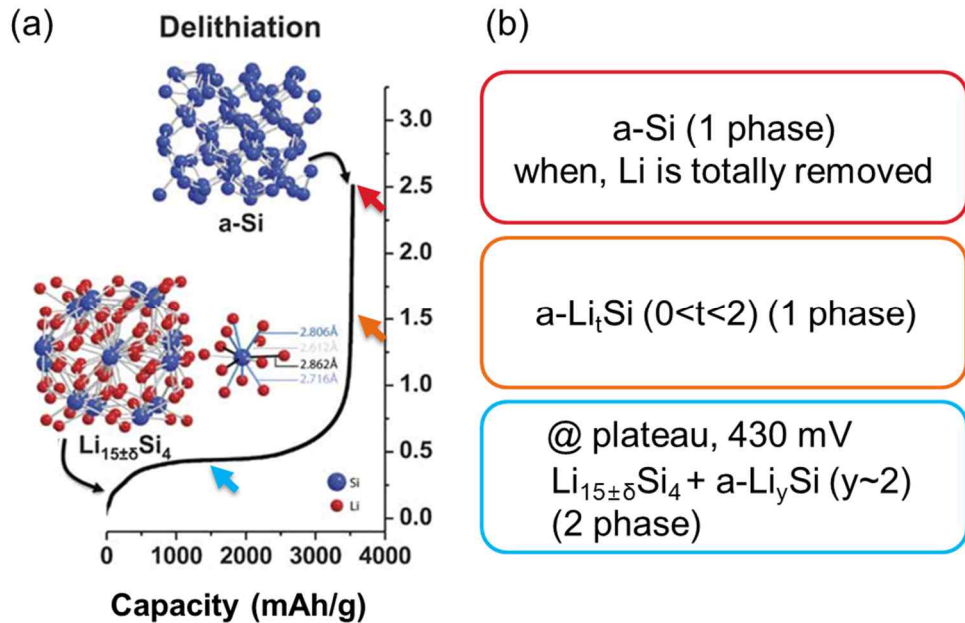


Figure 2.5 (a) The first galvanostatic delithiation curve of SiNW⁴⁸ (b) Phase transformation from crystalline Si to amorphous phase during lithiation.

2.2. Mechanical fracture in thin film

The separation or fragmentation of a solid into two or more parts due to intrinsic or extrinsic stress is called *fracture*. The process of fracture has been categorized into several parts— damage accumulation, nucleation of cracks or voids, and growth of cracks or voids. Damage accumulation is related to the properties of a material, such as its atomic structure, crystal lattice, and grain boundaries.⁶¹ Therefore, these characteristics are different for different materials, such as metals, ceramics, polymers, and composites. When a stress is generated from certain internal defects or from some geometrical variations, it leads to a fracture in the film or an interfacial delamination between the film and the substrate. The stress concentration is based on equilibrium stress analysis, and its advancement due to the interface delamination and crack growth generates a fracture. Griffith in 1920 pioneered this energy balance approach and quantitative factors, such as energy release rate and interface toughness can be estimated from his theory.⁶²

2.2.1. Energy release rate and Griffith criterion

According to the Griffith fracture criterion, if potential energy decreases due to initial crack propagation, the corresponding work is equal to the energy consumed for the new surface creation by the crack extension. In other words, a crack cannot propagate if decrease in the associated potential energy is less than the material fracture energy i.e. the surface-energy. In 1956, Irwin proposed an energy approach for fracture based on the Griffith model. Irwin defined an *energy release rate*, G , which is the change in elastic strain energy in the cracked area. G is derived from the derivative of a potential

energy with respect to the crack length $2a$ and an infinite plate of thickness t under plane stress, as shown in Figure 2.6.⁶³ As the stress is applied, the crack opens up and the stored elastic strain energy is reduced. The elastic energy per unit volume in a solid under stress is given by $\frac{\sigma^2}{2E}$. By considering the volume of the material, the total strain energy released is⁶¹

$$\left(\frac{\sigma^2}{2E}\right)(2\pi a^2 t) = \frac{\pi a^2 t \sigma^2}{E} \quad (2.1)$$

or, in terms of the per-unit thickness of the plate under plane stress, the energy released is given by⁶¹

$$U_e = \frac{\pi \sigma^2 a^2}{E} \quad (2.2)$$

The decrease in strain energy, U_e , when a crack propagation is balanced by an increase in the surface energy, U_s , obtained by the creation of two new crack surfaces. The increase in surface energy is:⁶¹

$$U_s = (2at)(2\gamma_s) \quad (2.3)$$

where, γ_s is the specific surface energy (energy per unit area). In terms of per unit thickness of the plate, the increase in surface energy is $4a\gamma_s$. Now, the change in potential energy of the plate,⁶¹

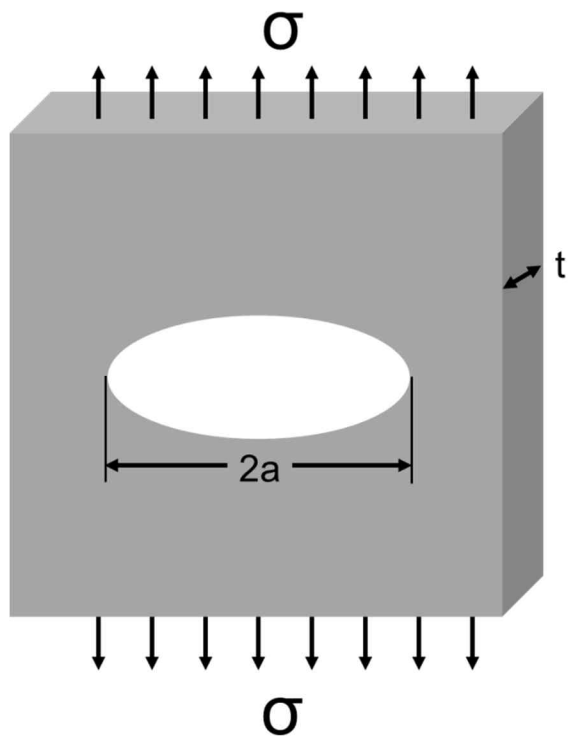


Figure 2.6 A through-the-thickness crack in an infinitely wide plate subjected to a remote tensile stress

$$\Delta U = U_s - U_e = 4a\gamma_s - \frac{\pi a^2 \sigma^2}{E} \quad (2.4)$$

where, ΔU is the change in the potential energy per unit thickness of the plate in presence of the crack, σ is the applied stress, a is the half the crack length, E is the modulus of elasticity of the plate, and γ_s is the surface energy per unit area.

As the crack advances, strain energy is released and new surfaces are created. From the energy equilibrium condition, by equating the first derivative of the potential energy ΔU with respect to the crack length we get,⁶¹

$$\frac{\Delta U}{\partial a} = 4a\gamma_s - \frac{2\pi a^2 \sigma^2}{E} = 0 \quad (2.5)$$

The critical stress required for the crack to advance in the plane stress condition is given by,⁶¹

$$\sigma_c = \sqrt{\frac{2E\gamma_s}{\pi a}} \quad (2.6)$$

For the plain strain condition, we need to consider the factor $(1-\nu^2)$ in the denominator because of the confinement in the direction of thickness. The expression for the critical stress for crack propagation is expressed in terms of the Poisson ratio ν ,

⁶¹

$$\sigma_c = \sqrt{\frac{2E\gamma_s}{\pi a(1-\nu^2)}} \quad (2.7)$$

The change in the rate of elastic energy with respect to the crack length (2.5) and energy release rate can be expressed by the relationship,⁶¹

$$G = \frac{1}{2} \frac{\partial U}{\partial a} \quad (2.8)$$

(2.6) and (2.7), under the plane stress and plane strain condition respectively, can therefore be modified to⁶¹

$$G = \frac{\pi a \sigma^2}{E} \quad (2.9)$$

$$G = \frac{(1-\nu^2)\pi a \sigma^2}{E} \quad (2.10)$$

The surface energy per unit area can be regarded as the property of the material, and independent of the geometry and the applied loading. Just to mention that, the terms fracture energy and *interface toughness*, Γ , will be used interchangeably in this thesis. The Griffith condition $G \geq \Gamma$ is a necessary condition for the onset of a crack growth. Values of Γ can vary widely, from about 1 J/m^2 for separation of atomic planes in brittle materials, where the strength of the chemical bonds dominates the resistance to fracture, to 10^4 Jm^{-2} or more in ductile materials.⁶²

2.2.2. Nucleation and growth of buckles in thin films

Thin film materials are widely used in many applications. When thin films are exposed to compression and the strain energy of this compression exceeds the interface toughness, then the surface thin films can have two different primary failure modes—edge delamination and buckle delamination. The elastic energy per unit area, which is stored in the film and is available for these delaminations, is given by equation 2.17. From the Figure 2.7, the flaw size that induces an edge and a buckle delamination is 1~2 h and 20 h, respectively. This implies that, the edge delaminations are more likely to be observed than the buckle delaminations. However, in many systems buckle delaminations have been found to occur more often because, edge delamination is a mode II cracking having the highest interface toughness, whereas buckle delamination is a mixed mode type but approaches mode II as the delamination spreads and becomes arrested.⁶⁴ In this thesis, we shall mainly focus on buckle-driven delamination. As mentioned above, compressed films are susceptible to buckling to release their strain energy through various relief patterns such as circular buckles, straight-sided buckles, and telephone cord buckles (Figure 2.8).^{65,66} These buckles are initiated either near the interface defects or at the free edge.⁶⁷ Buckling loads at the edge of the interface crack between the film and the substrate and start to grow. The failure phenomenon involves both buckling and interfacial crack propagation. As illustrated in Figure 2.9, buckles lead the interface delamination between the thin film and the substrate. After buckling, the stress in the film is no longer spatially uniform adjacent to the buckles.⁶² Furthermore, the transition in stress state from the unrelaxed condition in the still-bonded region to the relaxed condition within the buckled region occurs

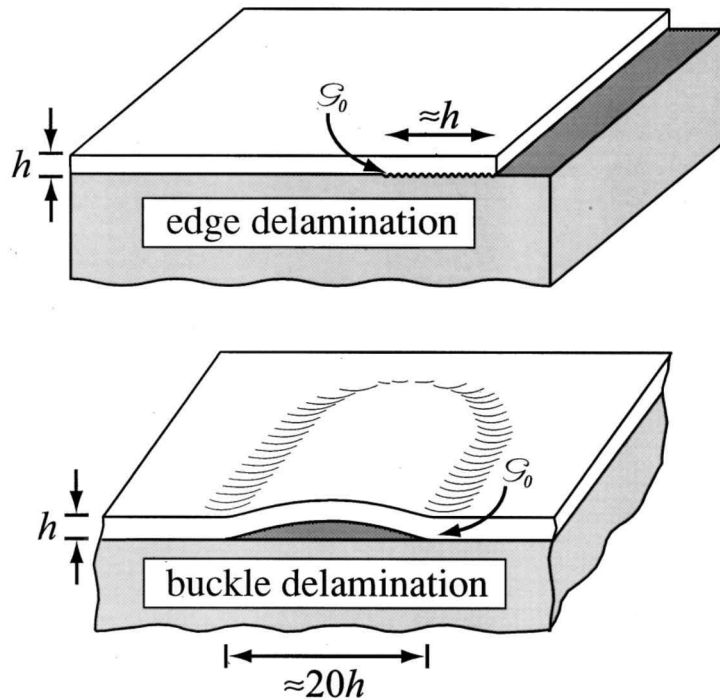


Figure 2.7 (a) Edge delamination and (b) Buckle delamination with the minimum flaw sizes necessary to debond the film from the substrate⁶⁴

quite rapidly across the boundary of the buckled area of the interface. This induces a stress concentration at the interface along the edge of the buckled region. Such stress concentrations can affect the subsequent growth of a buckled region in size, or bring a change in its shape due to proceeding delamination.⁶²

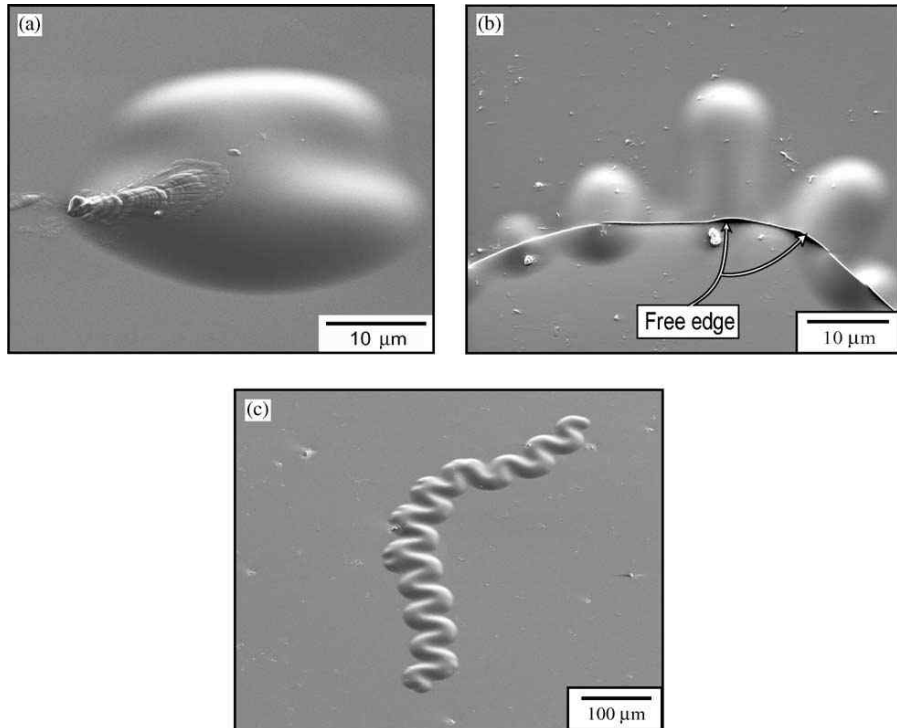


Figure 2.8 Various buckle configurations (a) Circular (b) Straight-sided, and (c) Telephone-cord buckle ⁶⁶

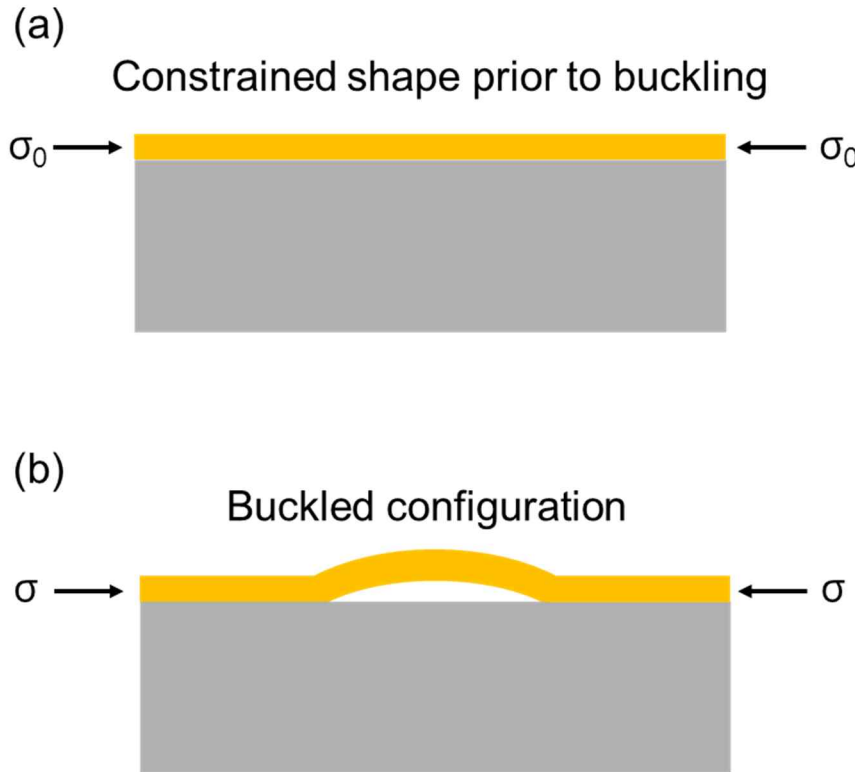


Figure 2.9 A schematic of thin film shape (a) under the pre-stress, σ_0 , and (b) under the resultant stress, σ . Buckle configurations lead the delamination between the film and the substrate.

2.2.2.1. Circular buckle

When a film is under the equi-biaxial compressive stress (σ_0), the film is relaxed over a circular region of radius (R) and thickness (h). If the size of the buckled region increases by propagation of the delamination front, the shape of the region remains circular.⁶² The classical buckling stress of a clamped circular region is⁶⁸

$$\sigma_c = 1.2235 \frac{E}{1-\nu^2} \left(\frac{h}{R} \right)^2 \quad (2.11)$$

The asymptotic result for the energy release rate is⁶⁸

$$G = G_0^* [1 + 0.9021(1 - \nu)]^{-1} \left[1 - \left(\frac{\sigma_c}{\sigma} \right)^2 \right] \quad (2.12)$$

where, G_0^* is the strain energy per unit area stored in the unbuckled film,⁶⁸

$$G_0^* = \frac{(1 - \nu) h \sigma_0^2}{E} \quad (2.13)$$

2.2.2.2. Linear/nonlinear buckle

A straight buckle usually propagates with a curved front. (its various parameters are illustrated in Figure 2.10.) The conditions at the stationary side and the circular front have been considered in terms of mode mixity and the energy release rate.⁶⁸⁻⁷⁰ The critical compressive biaxial stress at the onset of buckling, σ_c , is⁶⁸

$$\sigma_c = \frac{\pi^2}{12} \frac{E}{1-\nu^2} \left(\frac{h}{b} \right)^2 \quad (2.14)$$

The average rate of energy release is the difference between energy per unit area of the plate, U_0 , in front of the propagating end in the unbuckled state and the average energy per unit area well behind the end in the buckled state, \bar{U} , i.e. $\bar{G} = U_0 - \bar{U}$. The energy per unit area in the unbuckled state for an equi-biaxial compression is same as in equation 2.13. The average energy per unit area in the buckled state is given by—

$$\bar{U} = U_0 \left[1 - \left(\frac{1+\nu}{2} \right) \left(1 - \frac{\sigma_c}{\sigma_0} \right)^2 \right] \quad (2.15)$$

$$U_0 = \frac{(1-\nu)h\sigma_0^2}{E} \quad (2.16)$$

The energy release rate averaged over the curved front for the straight buckle is ⁶⁸

$$\bar{G} = G_0 \left(1 - \frac{\sigma_c}{\sigma_0} \right)^2 \quad (2.17)$$

where, G_0 is the available energy per unit area stored in the unbuckled film that is subjected to reduce under plane strain conditions,

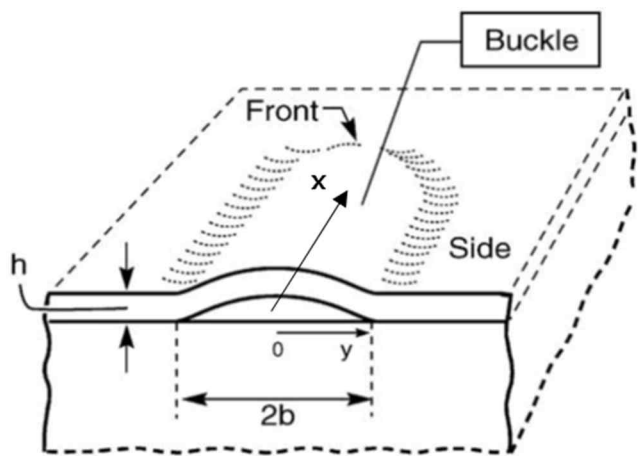


Figure 2.10 The geometry parameters in straight buckle⁶⁶

$$G_0 = \frac{1+\nu}{2} U_0 = \frac{(1-\nu^2)h\sigma_0^2}{2E} \quad (2.18)$$

The straight buckle relieves the compression along the y-direction but not in the x-direction. However, when the compressive stress increases in the film, only one-dimensional relaxation is not sufficient to release the elastic energy. Therefore, additional undulations along the x-direction can effectively reduce the compression, resulting in a telephone-cord buckle. This transformation from the straight buckle to telephone-cord buckle takes place dependently with a Poisson's ratio and σ_c/σ_0 , as shown in Figure 2.11

The normalized average energy release rate, \bar{G}/U_0 of straight buckle and telephone cord buckle has been plotted in Figure 2.12. Between both these buckles, the straight buckle is more favored when $\sigma_c/\sigma_0 < 6.5$ and any non-linear buckles are unlikely to form. However, telephone cord buckle becomes dominant when, $\sigma_c/\sigma_0 > 6.5$ because telephone cord buckles are more effective in lowering the energy.⁷¹ Actually, it is reported that a telephone cord buckle is more easily observed than a straight buckle in highly compressed thin films.⁶⁶

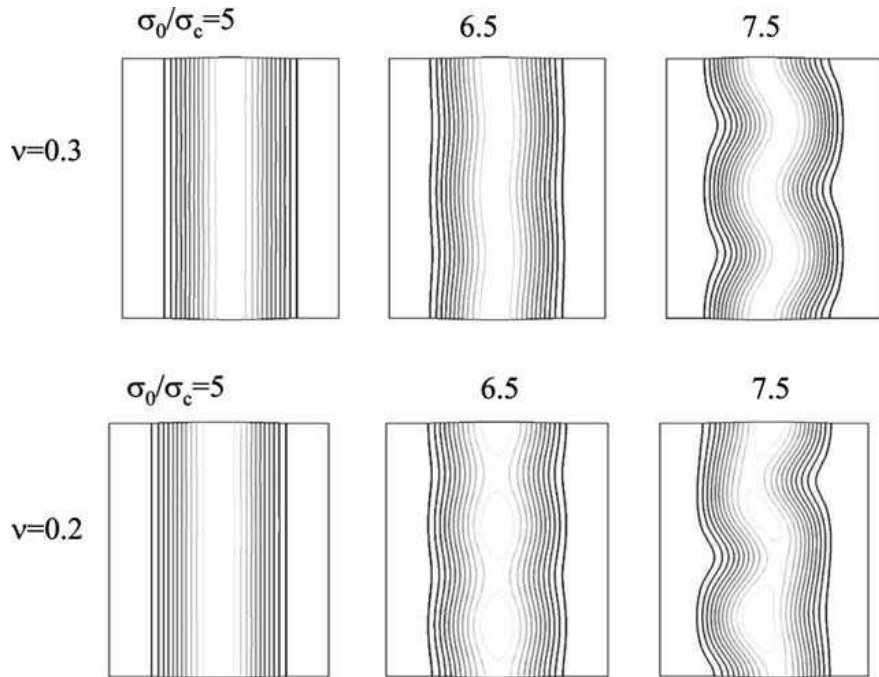


Figure 2.11 Buckle configurations from straight (left), varicose (middle), and telephone-cord (right). Bifurcation is determined from the Poisson's ratio and σ_c/σ_0 using the finite element code, ABAQUS.⁷¹

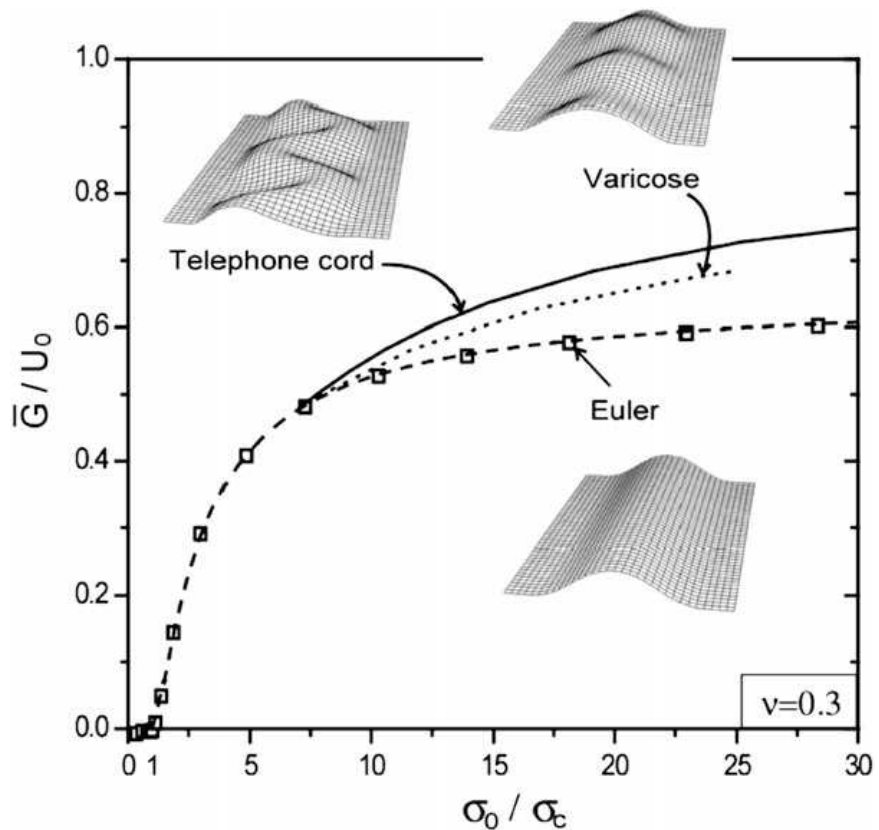


Figure 2.12 Buckle configurations from straight (left), varicose (middle), and telephone-cord (right). Bifurcation is determined with a Poisson's ratio and σ_c / σ_0 using the finite element code, ABAQUS.⁷²

2.2.3. Nucleation and growth of cracks in thin films

When thin films of metals, ceramics and polymers, are subjected to residual stress, cracking of the films are induced to relieve the elastic energy with various patterns as shown in Table 2.1.⁶⁸ These cracks are normally nucleated at a flaw in the material or at a surface damage site and advance as long as the elastic energy released from the system equals or exceeds the interface toughness of the system.⁶² In this regard, a dimensionless number Z is defined as the energy release rate for a crack and is given by⁶⁸

$$G = \frac{Z\sigma^2 h}{E_f} \quad (2.19)$$

Z acts as a driving force depending on the pattern of the crack.

For a given material system, a specific pattern is effective when the film is above the *critical thickness*, given by⁶⁸

$$h_c = \frac{\overline{E_f}\Gamma}{Z\sigma^2} \quad (2.20)$$

where, Γ is the relevant interface toughness of the system.

The result of the competition between crack patterns, such as crack penetration into the substrate vs. crack deflection into an interface is determined by the fracture resistance ratio $\Gamma(\psi)/\Gamma_s$ where $\Gamma(\psi)$ is the fracture resistance of the interface at a phase angle and Γ_s is the fracture resistance of the substrate material to mode 1 crack

Table 2.1 Commonly observed crack patterns with a dimensionless driving force Z^{68}

Cracking Patterns	$G = Z\sigma^2 h / \overline{E_f}$
	Surface crack $Z=3.951$
	Channeling $Z=1.976$
	Substrate Damage $Z=3.951$
	Substrate Damage $Z=0.343$
	Debond $Z=1.028$ (initiation) $Z=0.5$ (steady state)

growth. The material and geometrical parameters are arranged into non-dimensional groups, $\frac{\sigma_m^2 h_f}{E_f \Gamma_f}$ versus Γ / Γ_s can be divided into regions of film cracking and interface delamination. The ratio Γ / Γ_s prevents any further crack penetration into the substrate. The relation among the three non-dimensional groups has been illustrated in Figure 2.13⁶²

2.2.3.1. Minimum crack spacing

If a thin film is attached to a substrate, and if that film is subjected to a residual tensile stress, the stress can be partially released by formation of surface cracks and channeling the cracks in the film. According to X. Xiao's work³⁰, they tried to figure out what determines the crack spacing in Si film on Cu substrate. They assumed that, if a very small crack spacing is present, known as minimum crack spacing, then no additional crack could be inserted via plastic strain localization between the already existing cracks in Si. From the force equilibrium, they set the minimum crack spacing as

$$L_{cr} = \frac{2\sigma_Y^{Si}}{\tau_{cr}^{\text{int}}} \quad (2.21)$$

where, τ_{cr}^{int} is the interfacial shear strength between lithiated Si and Cu, which is the minimum values between the shear flow stress of Cu or the interfacial friction strength. σ_Y^{Si} is the yield strength of silicon. The acceptable values for τ_{cr}^{int} and σ_Y^{Si} are 40 MPa and 1-1.75GPa, respectively. Therefore, L_{cr} varies with the

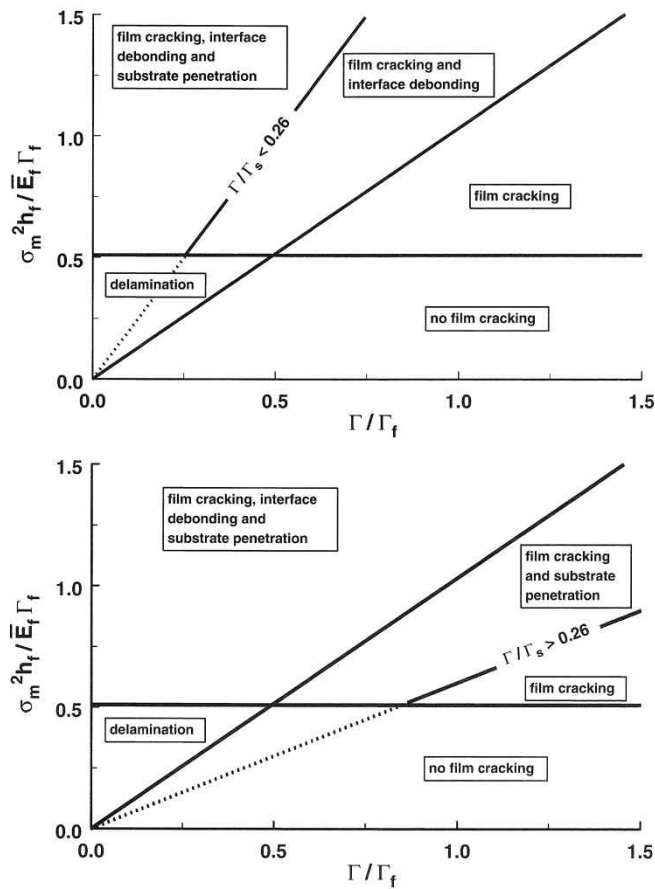


Figure 2.13 Dimensionless groups of system parameters, $\frac{\sigma_m^2 h_f}{\bar{E}_f \Gamma_f}$ is plotted as a function of Γ / Γ_f with Γ / Γ_s (<0.26: upper, >0.26: lower) For $D_1=0$ (Dundurs parameter, $D_1 = \frac{\bar{E}_f - \bar{E}_s}{\bar{E}_f + \bar{E}_s}$), the Γ / Γ_s ratio is approximately 0.26)⁶²

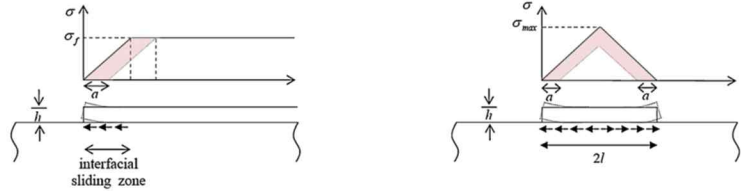
thickness of Si film. If the length of the Si film (L_{Si}) is well above the L_{cr} , the thin film is relatively susceptible to plastic strain localization, leading to a large amount of dislocations in the Cu substrate during the lithiation and delithiation cycles. Such dislocations would then result in interfacial delamination of the lithiated Si film from the Cu substrate. However, if L_{Si} is below the L_{cr} , no plastic strain localization in the Si film can occur because the film stress would be beneath the plastic flow stress of the lithiated Si, preventing any dislocation in Cu and thus, will also stop interfacial delamination.

2.2.3.2. Critical delamination length

Mechanical degradations, such as fracture and delamination of Si is most commonly observed mainly during the lithiation and the delithiation cyclic processes.^{22,30} From the mechanical perspective, cycling-induced microcracks continue to grow through the film thickness as long as the Si film is adhered to the current collector. However, since delamination of Si film directly leads to a rapid decay in the capacity, such events are much more important to prevent in order to maintain the capacity of Si anode.⁷³ The film delamination is presumed to occur via the propagation of a delamination front, or an interfacial delamination crack from the elastic energy stored (residual stress) region in the film in order to release the stress level, when $G \geq \Gamma$.⁶² To protect the delamination of Si thin film, several approaches were conducted by reducing the thickness of the Si film,^{29,59} and enhancing the adhesion between the Si film and the substrate.⁷⁴ Especially, Hamed haftbaradaran reported a concept of deducing the critical length for thin films to avoid the delamination under plane strain condition,⁷³

where they introduced a large scale interfacial sliding near the edge of the film. If the length of the Si film is larger than the spacing

(a) length of the film \gg sliding zone size (b) length of the film \sim sliding zone size



- | | |
|---|--|
| <ul style="list-style-type: none"> - Crack growth ($a > h$) - G is independent of the crack size - No size effect | <ul style="list-style-type: none"> - Strong size effect (away from film thickness) - Deduce the critical size for delamination - Strong size effect |
|---|--|

Figure 2.14 A comparison between no interfacial sliding model and interfacial sliding model.⁷³

of the sliding zone, a delamination edge crack grows more steadily than the case, where the crack size is longer than the film thickness [see Figure 2.14 (a)]. Under such conditions, the energy release rate is independent of the crack size, and no size effect is expected. In fig 2.14 (b), if the interfacial sliding from the island edges are long enough so they can extend over the entire island, a delamination size effect also comes into play and dependence on the size of the sliding zones can be observed, in addition to that on the film thickness. The interfacial sliding theory explains that the internal stress reduces as the two edge cracks increases in size, resulting in a decrease in $\sigma_{\max} (< \sigma_{fracture})$. Interfacial sliding zones decide the length scale which the maximum stress value in the film (σ_{\max}). When this σ_{\max} does not reach to the $\sigma_{fracture}$, film does show a fracture therefore we can expect the critical size for delamination.. Thus, a critical size for delamination has been proposed.

Considering a Si patch of length $2l$ and thickness h with an edge delamination crack a near the edge of the film and x is distance from the center of Si patch, the axial stress distribution of the half island is

$$\sigma_{xx} = \frac{\tau_0}{h} \begin{cases} l - a - x & l - a > x > 0 \\ 0 & l > x > l - a \end{cases} \quad (2.22)$$

The total elastic energy stored in the film in half of the patch is derived under the plane strain condition

$$U_{el} = \int_0^l \frac{1-\nu^2}{2E} \sigma_{xx}^2 dx = \frac{(1-\nu^2)\tau_0^2}{2hE} \frac{1}{3} (l-a)^3 \quad (2.23)$$

The energy release rate G is

$$G = -\frac{dU_{el}}{da} = \frac{(1-\nu_f^2)\tau_0^2}{2hE}(l-a)^2 \quad (2.24)$$

From the Griffith fracture criterion $G \geq \Gamma$, in an interfacial crack free state, i.e. $a=0$, the critical length (l_{cr}) is

$$l_{cr,nuc} = \sqrt{\frac{2hE\Gamma}{(1-\nu_f^2)\tau_0^2}} \quad (2.25)$$

The assumption of this approach is based on the energy equilibrium concept, that the total released elastic energy is completely consumed to create new surfaces. During this continuous interfacial crack propagation, the Si film is totally peeled off from the substrate, when $a=l$. The changes in the elastic energy and the surface energy are shown in Figure 2.15. From this relation, we can obtain the critical length for full delamination can be derived as follows—

$$l \geq l_{cr,del} = \sqrt{3}l_{cr,nuc} = \sqrt{\frac{6hE\Gamma}{(1-\nu_f^2)\tau_0^2}} \quad (2.26)$$

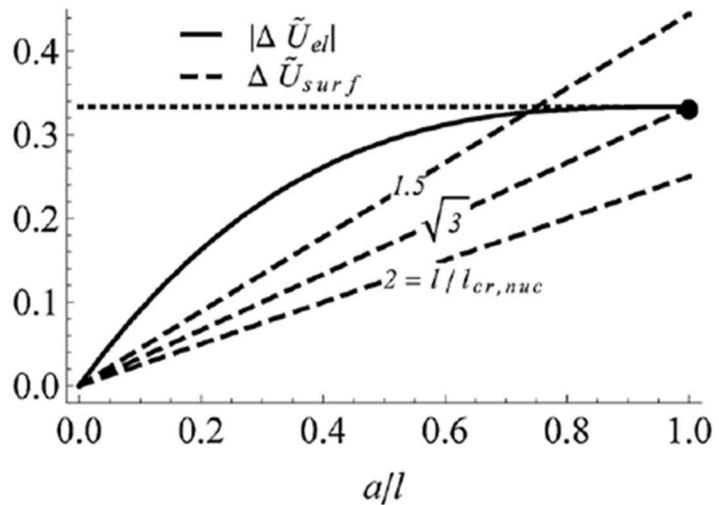


Figure 2.15 Changes in elastic energy in the Si film and surface energy as a function of the crack a with respect to l

2.2.3.3. Mechanical failure: Failure due to fatigue

A fatigue refers to a failure under the cyclic load having two different physical mechanisms: a) low-cycle fatigue involving large cycles with plastic deformation and short life, and b) high-cycle fatigue experiencing the low load and cycles within the elastic region. Fatigue failure can be rationalized in three steps: fatigue crack initiation, crack growth and fracture. Fatigue crack is initiated mainly by dislocation activities. Wood (1958) postulated that a cyclic load leads the material to different levels of net slip on different glide planes, resulting in rough valleys (or hills). These valleys become the stress concentration sites inducing crack nucleation.⁷⁵ Fatigue failure is initiated from a crack along the bands, where the slip is remarkably large. These slip lines are named *persistent slip bands* (PSBs) in which extrusion or intrusion occurs.

The propagation of fatigue crack can be plotted against the derivative of crack length (a) with respect to the number of cycles (n) i.e. da / dn . In this plot, three different regimes of crack growth rate can be seen. Region A is the fatigue region where crack propagation is undetectably low. Region B is known as Paris regime, where a linear relationship between $\log da / dn$ and $\log \Delta K$ (stress intensity factor) can be identified. In region C, the crack growth rate rapidly increases and leads to a catastrophic failure.

If this fatigue crack initiation and propagation occurs sequentially in a thin film metal electrode, it severely hinders the migration of the electrons and resistivity increases. In the current work, the electrical characteristics have been analyzed via the cyclic bending fatigue test using the resistivity change from the fatigue cracks.

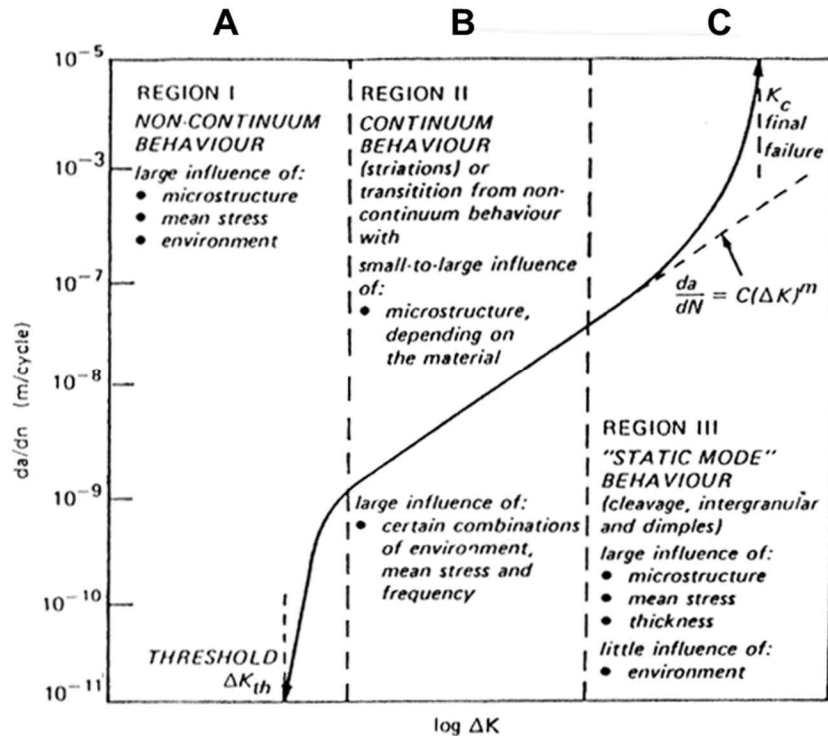


Figure 2.16 Illustration of crack initiation and propagation regimes with three different region by plotting da/dn versus $\log \Delta K$

CHAPTER 3

Electrochemical and mechanical behavior of Silicon thin film anode on soft substrate

3.1. Introduction

Si is known to have the highest theoretical specific capacity (about 4,200 mAh/g), which is nearly ten times higher than that of commercial graphite based anode, and low working potential (~0.5 V vs. Li/LI⁺).⁷⁷ However, a large volume change (300%) causes a dramatic decay in the capacity and induce failures. In general, thin films of Si are deposited on Cu foil, used as the substrate. It was C. Yu *et al.*, effectively released the stress of Si thin film on elastomeric substrate (i.e. poly-dimethylsiloxane, PDMS) and was able to release effectively any strain developed by generating out-of-plane deformation.⁷⁸ However, the cycling performance of Si thin film on polyimide (PI) substrate has not yet been investigated. In this chapter, the electrochemical performance of Si thin film on PI substrate has been investigated and surface morphologies have been studied. By introducing the fracture mechanics, the interface toughness of lithiated Si was also calculated.

3.2. Experimental procedure

The samples were fabricated at high temperature by vacuum deposition process. Since polymer substrates are susceptible to deformation when heated, the target substrate should be heat resistant with a high mechanical strength to find application as bendable batteries. We searched the most widely used soft substrates and their detail specifications, which are listed in table 3.1. Among these polymer substrates, we selected polyimide (PI), which has been widely used for polymer-based devices in aerospace and military, telecommunications, medical and general electronics applications due to their excellent thermal stability, stable mechanical properties and good chemical and ultraviolet resistances compared to other polymer substrates.⁷⁶

From the equation (3.1), the window of film and substrate is simply sectioned in Figure.

3.1. The fracture strain (ε) of Si is known to be 1%,

$$\varepsilon = \frac{(h_{sub} + h_{film})}{2r} \quad (3.1)$$

To satisfy the aim of this thesis, substrate and Si film should be below the 600 μm and 1 μm for bending radius (r) 30 mm at least (grayed region is out of our experimental region in Figure 3.1 (b)). The fabrication scheme of the battery anode system, has been shown in Figure 3.1. (1 μm of Si thin film is due to the delamination events shown in Figure 2.4 (b)). Pristine PI (125 μm , DuPont) served as the substrate and was used as received. On top of the PI, thin films of Cu (200 nm thickness) and Si (300 nm thickness) were deposited sequentially using a metal mask to serve as the current collector and

active material, respectively. The surface morphology has also been shown in Figure 3.2 (bottom).

For the *ex-situ* coin-cell test, coin-type half cells (2032R type) were assembled in a glove box (KK-011-AS, Koreakiyon) in an Ar atmosphere with less than 1 ppm moisture and oxygen content. A detailed description of the coin-cell assembly is provided in the Figure. 3.3. A 1M LiPF₆ electrolyte in a mixture of ethylene carbonate (EC) and diethyl carbonate (DEC) (1:1 by volume) was employed. Lithium metal foil was used as a counter electrode. A cycler system (WONATECH, WBCS3000) was introduced for the electrochemical measurement. The cells were galvanostatically discharged to 0.001 V (versus Li/Li⁺) at a constant current of 50 μ A .

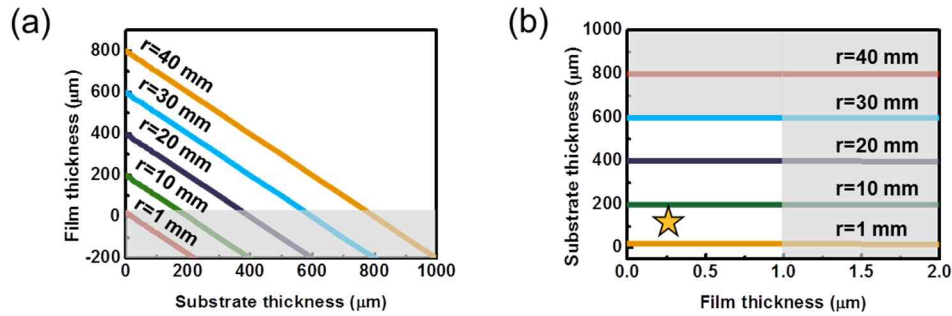


Figure 3.1. The relation from equation (3.1) between (a) substrate and film thickness with bending radius (b) ideal range for the aim of this research. Star means our experimental condition.

Chapter 3: Electrochemical and mechanical behavior of Silicon thin film anode on soft substrate

Table 3.1. Various kinds of soft substrates and their detail specifications.

Soft Substrate		Merits	Limits	Company
PET	Polyethylene Terephthalate	1. Resistant to UV 2. Resistant to chemicals	1. Double refraction 2. Color change by heat 3. High CTE 4. Low fabrication temperature (130°C)	General Atomics, Mitsubishi Chemical
PEN	Polyethylene Naphthalate	1. Resistant to chemicals 2. Low moisture absorption 3. Low CTE	1. Double refraction 2. Low fabrication temperature (150°C) 3. Weak optical transmittance	Teijin DuPont
PC	Polycarbonate	1. Commercialized 2. Excellent optical transmittance	1. Weak to chemicals 2. High CTE 3. Low fabrication temperature (180°C) 4. Weak to UV	Teijin, GE, Mitsubishi Engineering
PES	Polyether Sulfone	1. High fabrication temperature (230°C) 2. Resistant to UV 3. Commercialized	1. High moisture absorption 2. High CTE 3. Weak to chemicals	i-Components, Sumitomo Bakelite
PI	Polyimide	1. High fabrication temperature (360°C) 2. High mechanical strength 3. Resistant to chemicals 4. Low CTE 5. Resistant to H ₂ O permeation 6. Excellent optical transmittance	1. Double refraction	DuPont, Mitsubishi Engineering, Kolon, SAIT

출처: 강정원, 대신증권 산업분석 (2012)

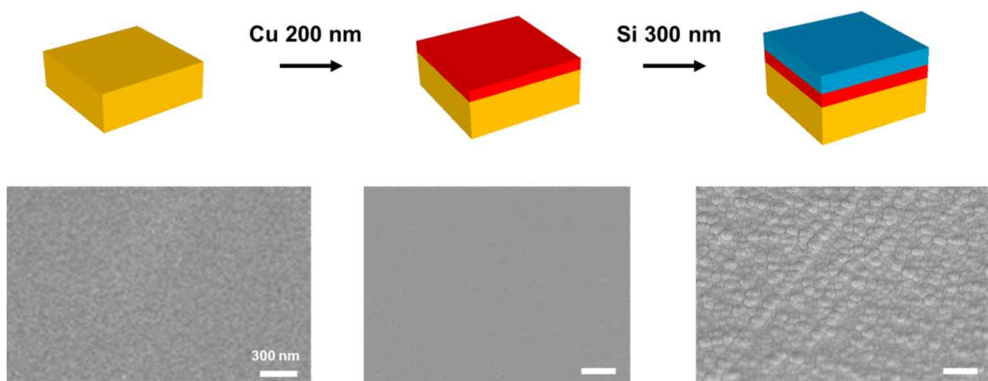


Figure 3.2. Deposition sequence of Cu and Si for the battery anode system .

Surface morphology is below the schematics captured by FE-SEM

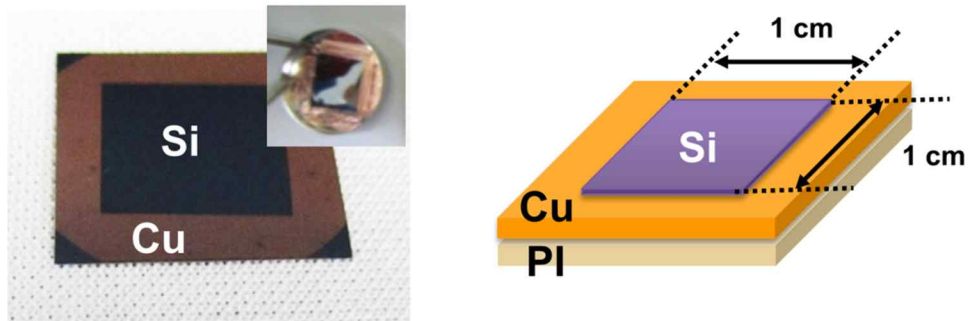


Figure 3.3. Coin-cell assembling. Cu (200 nm) was deposited onto the PI substrate, and Si (300 nm) was subsequently deposited using a metal mask with an area of 1 cm². Cu tape was used to attach the sample and electrically connect the same with the coin cell.

3.3. Results

We investigated the crystallinity of Si thin film through X-ray analysis and performed a lithiation process. After the first lithiation, catastrophic failures (circular buckles, telephones cord buckles) of Si thin film were observed. Based on fracture mechanics, we estimated the interface toughness of lithiated Si on soft substrate.

3.3.1. Material characteristics of Si

Figure 3.4 presents the XRD pattern of the Si thin film on Cu-coated PI. XRD analysis was performed both on the Si and Cu thin films using the grazing incident angle diffraction mode. Except for two strong diffraction peaks corresponding to the Cu film, none of the Si peaks were detected within the measured range. This result indicates that the deposited Si thin film was amorphous. An important step was to verify the presence of the native oxide of Si and its thickness on the surface because this oxide critically affects the dimensional expansion and the electrochemical cycling life of the Si anodes.⁷⁹ It has been reported that an oxide layer on the Si contributes to an irreversible capacity loss and lowers Coulombic efficiency upon further cycling. An oxide layer can also cause hydrostatic compressive stress, which limits the extent of lithiation. Therefore, investigating this oxide layer was necessary to understand the volume changes of the nanostructured Si anodes and determine a good life cycle. Past research had shown that, the cycling behavior is largely influenced by the thickness of the oxide layer. A lower capacity was observed when the oxide thickness was above 7 nm, whereas not much difference was observed for thicknesses below 3 nm. In the current work, the existence of Si oxide layer was verified by XPS. Figure 3.4 (b) shows the surface and

inner chemical states of the deposited Si. Although there are various chemical structures of Si oxide (Si, Si₂O, SiO, Si₂O₃ and SiO₂) following Siⁿ⁺ (n=0, 1, 2, 3, or 4), Si⁰ and Si⁴⁺ are the dominant components based on our results, suggesting the formation of a Si and SiO₂ matrix on the surface.⁸⁰ This formation of SiO₂ is probably due to the exposure of the Si-deposited samples to air while preparing the coin-cell assembly. However, no Si⁴⁺ signal was detected in the inner region of the Si film after sputtering. This lack of Si⁴⁺ signal indicated that the Si oxide layer was merely formed on the surface, and the thickness of the oxide layer was approximately 2.5 nm from the surface when the sputtering depth of XPS was considered. Therefore, oxide layer does not critically affects the cycling behavior in our case.

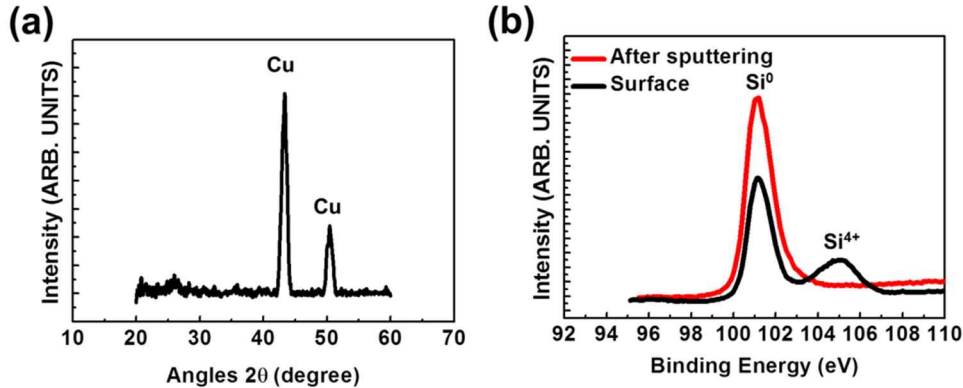


Figure 3.4. (a) XRD pattern of the deposited thin film on PI substrate, (b) XPS studies of the thin film before (black) and after (red) sputtering.

3.3.2. Failures of Silicon thin film after first lithiation

The insertion of Li into Si thin film induces a volume expansion of the film upto 300%, but at the same time, Cu/PI constrain the volume change, resulting in a compression. On the other hand, the extraction of Li from lithiated Si causes a tension in the Si film. On the surface, various types of Si fractures induced from these stress evolutions have been identified.³⁰ In this regard, buckling, delaminations and cracks occur to release the stress out. Among these, the bucklings and the delaminations are normally observed under compressive stress and cracking is seen under tensile stress. On lithiation of the Si film on PI at a C/6 rate [Fig. 3.5 (b)] a huge compressive stress generated, similar to that observed and investigated by Guduru's group through an *in-situ* stress measurement

method.^{53,54} They studied the stress that generated during electrochemical lithiation and delithiation by using the multi-beam optical sensor (MOS) technique. In the corresponding work, the Si thin film electrode showed a plastic deformation at a compressive stress up to -1.75 GPa on lithiation from the plastic strain, as displayed in Fig. 3.5 (c). Upon delithiation, the electrode experienced an elastic strain in an opposite direction, resulting in a tensile stress up to 1 GPa and it showed a plastic deformation during the rest of the delithiation process.⁵⁴ After the end of the lithiation step inducing compressive stress, catastrophic failures can be observed [Figure 3.5 (a)]. Circular and telephone cord buckles were identified dominantly and delamination events could be easily observed. It was an anomaly to detect the cracks which were expected to be generated under tensile conditions. Especially, the circular and the telephone cord buckles have not been reported for Si thin film anode during lithiation to the best of our knowledge. These failures of Si thin film directly affect the cycling performance. The micro-cracks partially decrease the capacity due to SEI layer formation on the newly-created fresh surfaces. From a mechanical perspective, these cracks rather alleviate the stress, preventing further delaminations from the current collector. Therefore, delaminations are fatal to the battery performance due to the direct active material loss. In this research, we focused on compressive stress-induced failures, which need more attention to achieve an increased battery performance. The interesting fact is that the onset stress and the interface toughness (adhesion energy) can be easily calculated from the circular buckles and telephone cord buckles, as shown in chapter 2.⁶⁸

Circular and telephone cord buckles are normally formed in biaxially compressed thin films and are initiated near interface defects or free edges⁶⁷ as mentioned in chapter 2. These non-linear buckles, observed in many thin films, generally develop from thermal expansion coefficient mismatch or intrinsic stress originated from deposition process, or

lattice parameter mismatch.⁷¹ The above-mentioned sources of the fractures contain meaningful information, such as onset stress and interface toughness can be obtained by measuring some parameters.⁶⁸ In Figure 3.6 (a) and (b), we can identify the PI substrate, the Cu layer (200 nm) and the Si (approximately 250 nm) film. Just underneath and onto the Si thin film, Pt is supposed to be re-deposited during FIB sectioning. The interface toughness can be calculated by measuring the thickness and the width of the buckles.

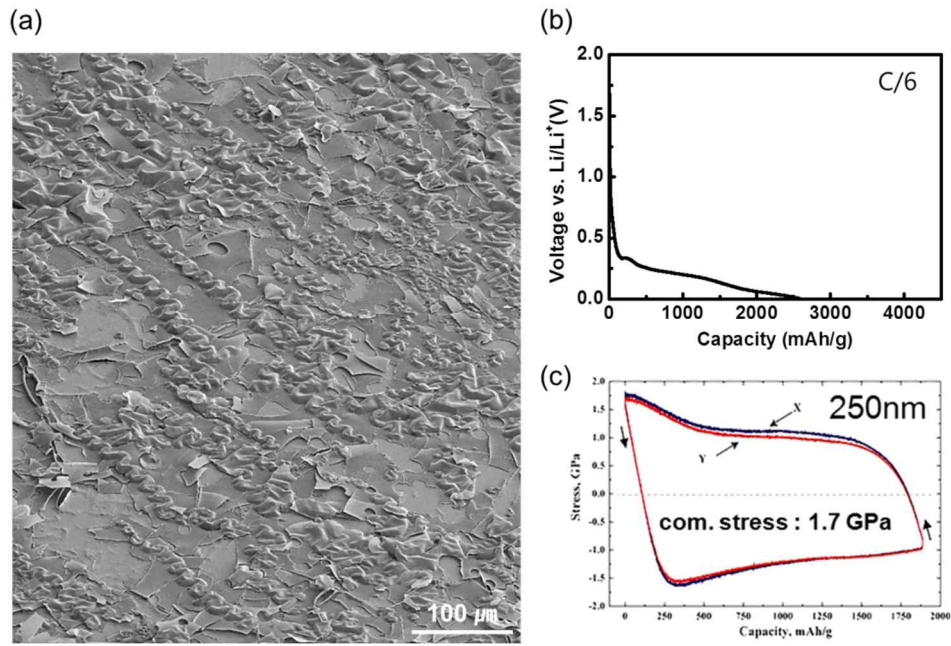


Figure 3.5. (a) Failure morphologies of lithiated Si after lithiation. Telephone cord and circular buckle are observed. (b) Discharge profile of Si thin film down to 0.001 V (c) quantitative stress study of Si thin film during cycling.⁵⁴

3.3.3. Interface toughness of lithiated Silicon

To understand the mechanical properties, we measured the geometric parameters, such as thickness of the thin film, radius of a circular buckle, and width of the telephone cord buckle by using the equations discussed in chapter 2. The onset stress of a circular buckle is measured by

$$\sigma_c = 1.2235 \frac{E}{1-\nu^2} \left(\frac{h}{R} \right)^2 \quad (2.11)$$

The equation for the energy release rate is⁶⁸

$$G = G_0^* [1 + 0.9021(1 - \nu)]^{-1} \left[1 - \left(\frac{\sigma_c}{\sigma} \right)^2 \right] \quad (2.12)$$

where, G_0^* is the strain energy per unit area stored in the unbuckled film,⁶⁸

$$G_0^* = \frac{(1-\nu)h\sigma_0^2}{E} \quad (2.13)$$

From these equation, the buckling stress of a circular buckle was calculated. The thickness and radius were measured as $h=240$ nm and $2R=8.57 \mu m$ (see Figure 3.7 (a) and (b)). For lithiated Si, the Young's modulus (E) and the Poisson's ratio are 50 GPa and 0.22, respectively.^{54,81} Therefore, σ_c obtained was 201 MPa. From these values, the energy release rate (G) can also be calculated from equation (2.12). If σ is

assumed to be 1.7 GPa, then the value of G is 6.26 J/m².⁵³ The reason to select E=50 GPa and $\sigma_0 = 1.7$ GPa is because circular and telephone cord buckles are likely to be formed when the stress exceeds the critical point (onset stress). According to the literature, the stress in a film has the highest value, when $x=0.33$ (in Li_xSi). At this state, the modulus is 50 GPa and the stress reaches to 1.7 GPa. According to the Griffith's fracture criterion, energy of creation of a new surface (adhesion energy) should be larger than the energy release rate. Therefore, the adhesion energy (interface toughness, Γ) of the lithiated Si was estimated to be 6.26 J/m². The practical interface toughness of lithiated Si has been approximated through statistical approaches by measuring the thickness and radius of other circular buckles. As a result, the onset stress and the interface toughness were calculated to be 183 ± 116 MPa and 6.52 ± 0.14 J/m², respectively as indicated in Table 4.1.

Characteristics of telephone cord buckles are also be calculated from the following equations,

$$\sigma_c = \frac{\pi^2}{12} \frac{E}{1-\nu^2} \left(\frac{h}{b} \right)^2 \quad (2.14)$$

and energy release rate is,

$$\bar{G} = G_0 \left(1 - \frac{\sigma_c}{\sigma_0} \right)^2 \quad (2.17)$$

$$G_0 = \frac{1+\nu}{2} U_0 = \frac{(1-\nu^2) h \sigma_0^2}{2E} \quad (2.18)$$

where, G_0 is the available energy per area stored in the unbuckled film subjected to reduction under plane strain conditions.

The width and the thickness of a telephone cord buckle is $2b=9.34 \mu m$ and 288 nm, respectively [see Fig. 3.7 (c) and (d)]. Therefore, the onset stress and the interface toughness are calculated as 70.6 ± 55.9 MPa and 5.59 ± 0.27 J/m², respectively as indicated in Table 3.2.

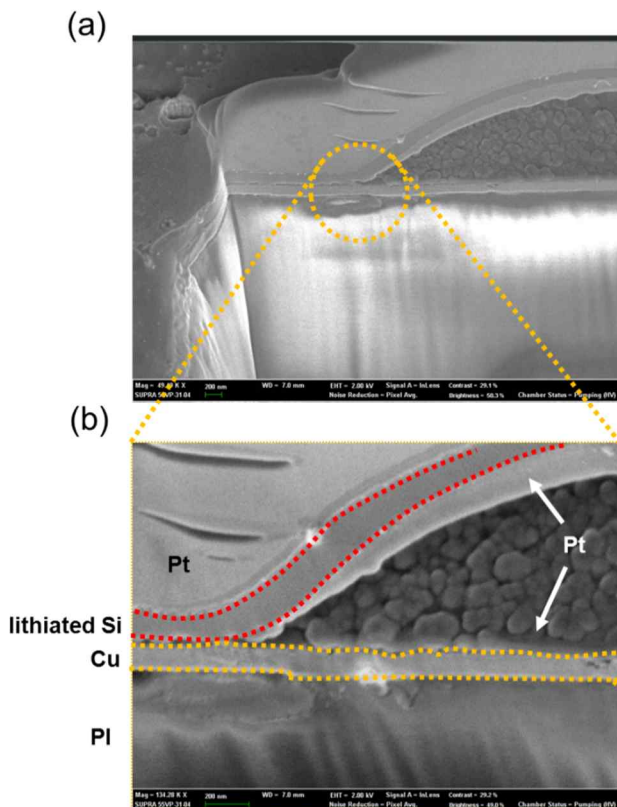


Figure 3.6. Cross-sectional view of a telephone cord buckle sectioned by FIB technique. (a) the interface between lithiated Si and Cu layer (b) enlarged image of (a). The Pt (protecting layer) was re-doped during FIB sectioning. The Cu and lithiated Si is clearly separated by compressive stress.

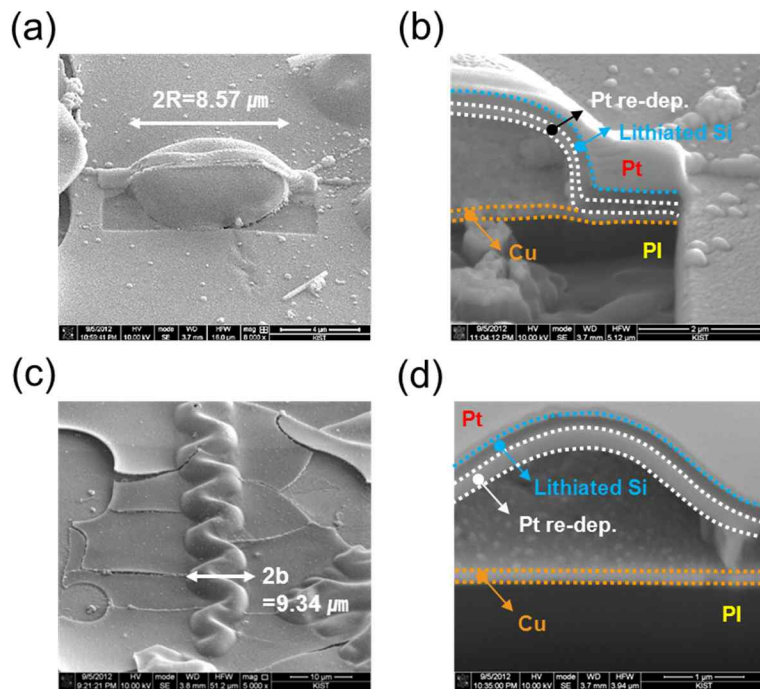


Figure 3.7. Measurements of different parameters—(a) radius of circular buckle and (b) thickness. (c) width of telephone cord buckle and (d) thickness

Table 3.2. Onset stress and interface toughness of circular and telephone cord buckles.

	Onset stress (MPa), σ_c	Toughness (J/m²), Γ
Circular buckle	183 ± 116	6.52 ± 0.14
Telephone cord buckle	70.6 ± 55.9	5.59 ± 0.27

Table 3.3 lists the interface toughness between Si and Cu. Cu current collector is essentially used for anode electrode system. Therefore, the interface characteristics with other active materials are very important. However, the interface between Cu and Si have been hardly studied. One report for the interface toughness between amorphous Si and Cu is shown in table 3.3 via the tensile test but interface toughness between lithiated Si and Cu is exclusive in this study.

From the EDS mapping analysis, we can accurately distinguish each layer on a severely failure surface (Figure 3.8). The Cu layer was stably attached to the PI substrate, whereas Si was partially peeled off by the circular buckle and was largely delaminated. These results show that the delaminated interface was between the Si and the Cu layer, but not between the PI substrate and the Cu layer. In the literature, the adhesion energy between PI and Cu was reported to be larger than 25 J/m^2 ⁸³ which is larger than that of Si/Cu interface. Therefore, the delamination interface is inevitably determined between Si and Cu. In conclusion, the cycling performance can be improved by increasing the interface toughness between the Si and the Cu layers. For this, an adhesion layer or surface treatment can be introduced to increase the roughness.

Table 3.3. Values of interface toughness between Si and Cu

Γ_c (J/m ²)	Remark	Reference
7.7±1.9	- Amorphous Si/Cu foil - Debond zone from tensile test	J.P. maranchi et al, J. Electrochem. Soc. 153 (2006)
Cir.: 6.52 ± 0.14 Tele.: 5.59 ± 0.27	- Calculation from buckles - Lithiated Si	Our reserach

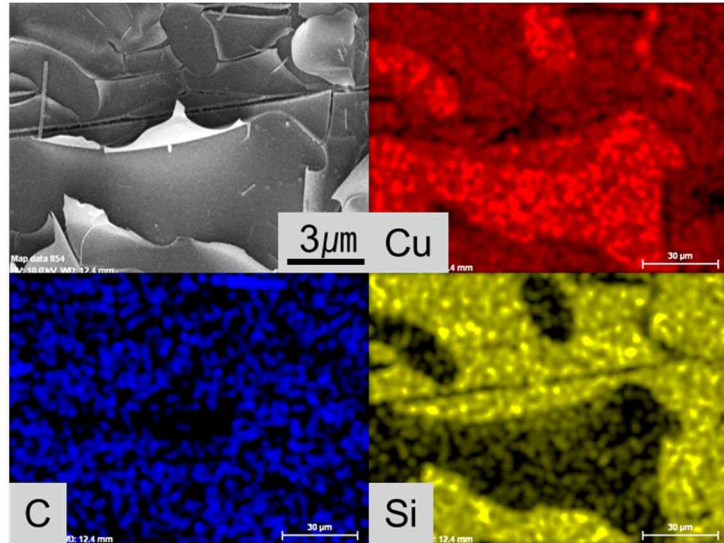


Figure 3.8. Delamination of Si thin film after lithiation. EDS analysis of Cu, C, and Si. Si is mainly peeled off from Cu layer. However, Cu is well attached onto the PI substrate.

3.4. Summary

In this chapter, mechanical degradation of Si thin film anode after lithiation process have been investigated. Due to the huge compressive stress, catastrophic failures, such as circular buckles, telephone cord buckles, cracks and delaminations were observed on the surface. The Guduru group studied on the mechanical properties of Si anode during lithiation and delithiation process via *in-situ* multi-beam optical sensor (MOS) technique.⁵³⁻⁵⁶ They obtained compressive and tensile stress of about 1.7 GPa from a 250 nm-thick Si film in the range 1.2–0.01 V vs. Li/Li⁺, which was similar to our results. We assumed that an analogous level of stress was built up in our Si thin film and further released through the formation of various fracture morphologies. We focused on not only these fractures of Si thin film but also on the mechanical properties of lithiated Si, e.g. onset stress and interface toughness, and measured them as well.⁶⁸ We analyzed the cross-sections of both the circular buckles and telephone cord buckles to measure the thickness. Using equations (2.11) and (2.14), we calculated the onset stress to be 201 MPa and 124 MPa for the circular and the telephone cord buckles, respectively. From the onset stress, we can finally obtain the interface toughness using equations (2.12) and (2.17). Instead of a single trial, we conducted several sequences to estimate the representative value. Through a statistical approach, we set the interface toughness as 6.52 ± 0.14 from the circular buckles and 5.89 ± 0.27 from the telephone cord buckles. This interface toughness values matched closely with Matt Pharr's *et al.* study ($5.4 \pm 2.2 \sim 6.9 \pm 1.9$).⁸² Therefore, our post-buckle analysis looked promising and have potential to contribute to practical anode design and fracture modeling of lithiated Si.

CHAPTER 4

Electrochemical and mechanical behavior of nano-hairy Silicon anode on soft substrate

4.1. Introduction

We observed in the previous chapter that, Si thin film has fatal issues on the mechanical properties in spite of its promising electrochemical performance. To address these drawbacks, various Si nanostructures, such as simple nanowires (NWs), core/shell NWs, coated NWs, embedded NWs and nanotube NWs,²³⁻²⁸ have recently been explored. These Si nanosturctures, due to their critical size effects, are efficient in releasing any strain that develops from free expansion and fracture resistance.²⁹⁻³² However, all of these trials had been done on metal foils but not on any polymer substrate. This is primarily because, syntheses of SiNWs require a very high temperature (hundreds of degree Celsius) at which most polymers melt and are unstable. Moreover, polymer substrates have very poor conductivity and the vacuum deposition process is also a challenge. In this chapter, we report the fabrication of a battery system, with Si anode from nanostructured polymer substrate by PECVD method and overcoming all the above-mentioned issues.

The relaxation of intrinsic stress was investigated through electrochemical measurement and the observed improvement in performance has been discussed from a mechanical perspective using the fracture theory. Additionally, a mechanical bending test was conducted to study the stability in terms of relaxation of extrinsic stress.

4.2. Fabrication of nano-hairy Silicon

Conventional SiNWs have several drawbacks and show poor electrochemical performance. Mainly, during the charging and discharging processes, unequal volume expansion and contraction causes a mis-match between the NWs and the substrate, inducing a complete delamination of the SiNWs from the substrate (see Figure 4.1 (a)). Moreover, cracks initiated from the outer surface of the SiNWs propagate into the core of the NW, resulting in a partial breakage of the NWs (Fig. 4.1 (b)). The traveling distance of electrons generated from an electrochemical reaction is very long, resulting in poor C-rate dependence, as shown in Fig. 4.1 (c). To overcome these limitations of SiNWs, using a polymer substrate (PI) based template has been suggested in the current work (Fig. 4.1 (d)). The PI substrate is heat resistant and has a high mechanical strength, which are the essential pre-requisites for the high temperature fabrication process and flexible application of the battery. As indicated in Fig. 4.1 (d), no shear stress occurs during the charge/discharge process because the PINWs are the same body, unlike conventional SiNWs. In addition, the polymer core blocks any crack propagation and prevents any separating and breaking issues associated with brittle SiNWs. The travelling distance and current clouding of electrons are also dramatically reduced, through formation of a current collector layer around the nanostructures. Dense nanostructure can maximize the surface area, providing sufficient reaction sites to the Li ions. These functions can effectively increase the C-rate dependence. The free spaces between PINWs are expected to accommodate any strain easily that would develop due to expansion of Si. As illustrated in this proposed model in Figure 4.1 e and f, when the deposited Si expands, the pliable PINWs allow bending motion without fracture. The PI

template can also release the strain from an extrinsic stress, such as bending and folding deformation through its pliable bending motions.

Plasma-based surface treatments have been normally adapted to create nano-structures on organic and inorganic materials, including Si and polymer substrates using various gases.^{84–86} These reports state that any non-etchable residues of the surface treatment reactions can act as etching mask and thereby, promote selective etching, as illustrated in Figure. 4.2. Fluorine containing gases (i.e. CF₄ or C₄F₈) have been introduced for nano-structuring by anisotropic etching process in Si industry and inorganic substrates.^{84,87–92} In these processes, ionized gas radicals (CF₃⁺) are accelerated and directed toward the negatively charged cathode plate or the chamber wall^{84–86}, where strong bombardment takes place. This event is similar to the sputtering process. Sputtered metals (M) are deposited on the soft substrates and are bonded with the fluorine radicals (F) in the gas to form MF. MF then acts as unetchable masks, thereby preventing the material below it from being etched. By contrast, soft substrates consisting of oxygen and carbon chain chemically react with gases to form volatile products, leaving back a dense layer of nano-structures. The interesting fact is that, the nano-structures can be controlled by the gas species, cathodic materials, gas pressure, etching time, and the accelerating voltage.

Using the PECVD method, we successfully fabricated various nanostructures on different substrates, as shown in Figure 4.3. We could freely modify the structure of Si using polystyrene (PS) bid with an etching pressure, time, and acceleration voltage on pure Si wafer, resulting in a well-aligned SiNWs and dual structure of SiNWs, in Figure 4.3 (a). PS could also be effectively etched with the different size of PS and etching conditions in Figure 4.3 (b). A high aspect ratio of the NWs was eventually obtained

using the PI substrate in Figure 4.3 (c). The notable result is that very fine (diameter: 30 nm) and

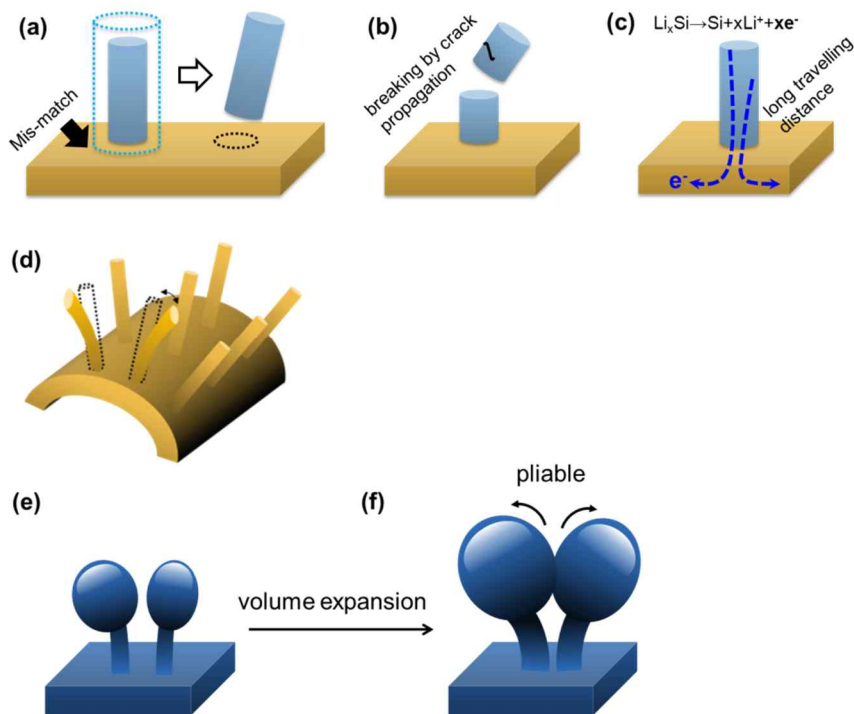
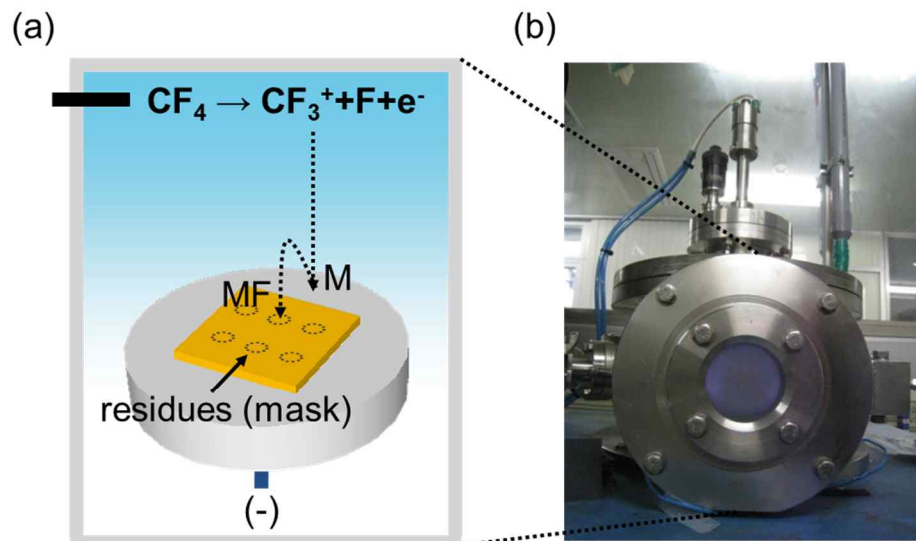


Figure 4.1. (a) Schematic design of the dense and pliable nano-hairy structures on a polyimide substrate. Cartoon schematics of the Si-coated polyimide nanowires (PINWs) (b) before lithiation and (c) after lithiation. (d) The delamination of SiNWs due to mismatch between SiNWs and the current collector during charging/discharging. (e) The partial breaking of SiNWs by crack initiation and propagation. (f) The long travelling distance of an electron from the Si NWs to the current collector.

long (height: $1.8 \mu\text{m}$) NWs was obtained by changing the inlet gas. A detail mechanism will be dealt in following chapter.

Nano-hairy structures integrated onto a polyimide (PI) substrate (Dupont, Kapton) were prepared (Figure 4.4 a) with a thickness of $125 \mu\text{m}$ using the RF glow discharge of CF_4 via plasma-enhanced chemical vapor deposition (PECVD) (Fig. 4.4 (b)). During the etching process, the gas pressure and the bias voltage were maintained at 30 mTorr and -500 V, respectively, and the operating time was 60 min. Because PI is a non-conductive substance, an artificial current collector layer was necessary. For the current collector layer, a 200-nm thick Cu layer was deposited on the nano-hairy PI substrate using the thermal evaporation method, as shown in Fig. 4.4 (c). The cross-section of the nano-hairy Si anode was visualized using a focused ion beam (FIB) sectioning (Fig 4.4 (e)). Cu was deposited at the bottom of the PI nano-hairy structure and along the nano-hairs to form a stable current collector. Si (300 nm) was then deposited on top of the Cu layer, as in Fig. 4.4 (d), which aggregated more at the tip and lesser at the side and bottom of the nano-hairy structure to form a mushroom shape. Enough space was left between the nano-hairs so that any strain that would develop from the volume expansion and bending deformation of Si, could be accommodated (Fig. 4.4 (f)). For comparison purposes, Cu (200 nm) and Si (300 nm) were deposited onto pristine PI using the same deposition conditions as shown in Figure 3.1.



1. Deposition of F atom-Metal residue (MF, unetchable) from the chamber wall or cathode electrode
2. Soft substrate (C-O chain) + $\text{CF}_x \rightarrow$ volatile gas ↑

Figure 4.2. Schematic of plasma-enhanced CVD (PECVD) mechanism (a) Formation of residues. (b) a real equipment during etching process

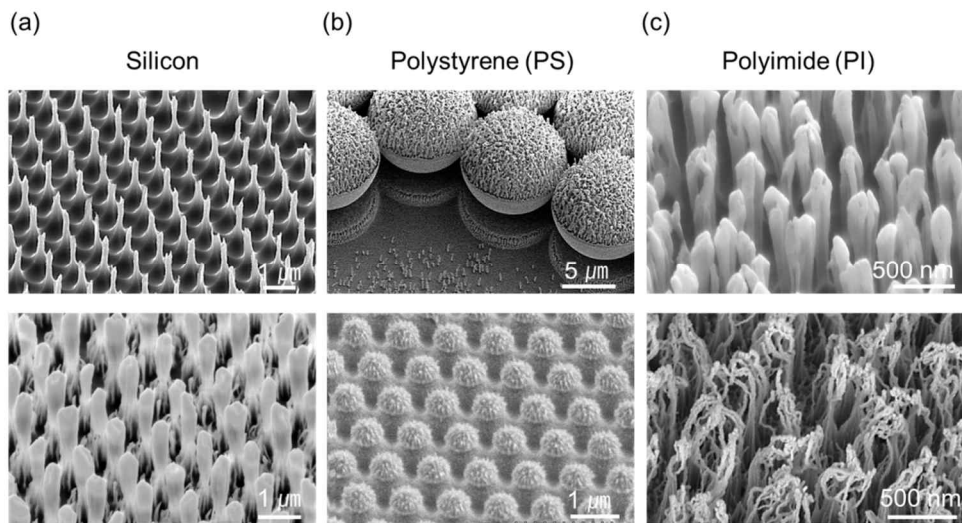


Figure 4.3. Various nanostructures from (a) Si wafer (b) polystyrene bid (c) polyimide substrate

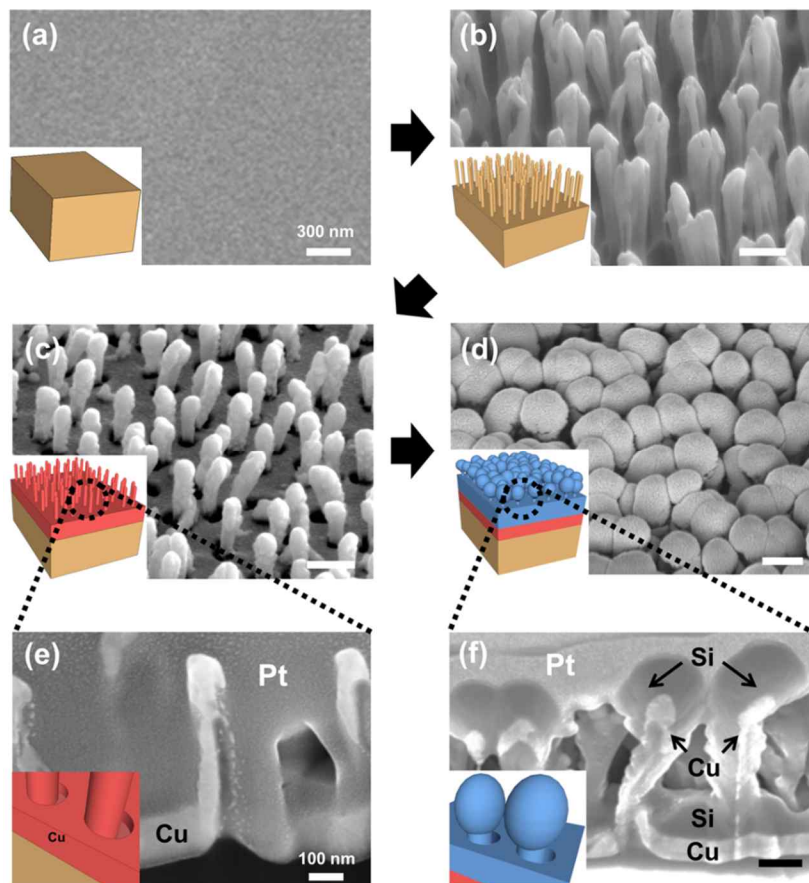


Figure 4.4. Direct integration of nano-hairy Si anode on a nanorod array polymer substrate: (a) Pristine PI substrate before CF_4 etching, (b) Well-arrayed PI nano-hairy structures after CF_4 PECVD etching on pristine PI, (c) Cu (200 nm) as the current collector deposited by thermal evaporation, (d) Si deposited (300 nm) as the active material by thermal evaporation on the sample (c), (e) A cross-sectional image of sample (c), and (f) A cross-sectional image of sample (d), both prepared by FIB cutting after Pt coating

4.3. Experimental procedure

In-situ Si lithiation experiments were performed using a nano-manipulator (MM3A, Kleindeck) installed in a FIB (focused-ion beam) system (Quanta 3D, FEI) (see Figure 4.5 (a)). Core/shell PI/Cu and Si samples were sectioned in the FIB chamber to study the cross sections. Bulk Li was cut into pieces using a micro-blade inside the FIB chamber to expose fresh surfaces without letting any oxidation. Li metal, located on a movable tungsten probe and directly controlled by the nano-manipulator, was placed in direct contact with a bundle of the polymer/Si core/shell nanostructure Si (Fig. 4.5 (b)). During the *in-situ* test, no potential was applied, and the sample was grounded with a carbon tape.

The cells were galvanostatically charged and discharged within the voltage range 0.001 V to 2.00 V (versus Li/Li⁺) at a constant current with a C/6. Furthermore, the high reversible capacities of the various charge/discharge rates were also demonstrated. The currents were calculated using the theoretical capacity (4,200 mAh/g). The cell was first cycled at C/20 and subsequently cycled at C/10, C/5, C/2.5, 1 C, 2.5 C, 5 C, 10 C in a step-wise manner; then, the cycle was returned to C/20. The morphology and composition of the synthesized and electrochemically tested samples were observed using field emission scanning electron microscopy (FESEM) and an energy dispersive spectrometer (EDS) (Carl Zeiss, SUPRA 55VP), respectively. The final products were washed with dimethyl carbonate (DMC) prior to the subsequent morphology observation.

The change in electrical resistance as a function of cycle numbers was measured by two different bending tests. The first bending test was conducted with a metal thin film on PI under a cyclic sliding motion to demonstrate for repeated flexible

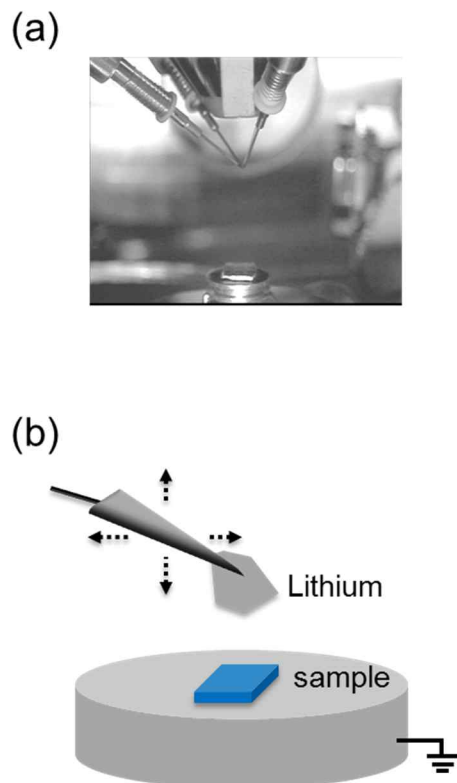
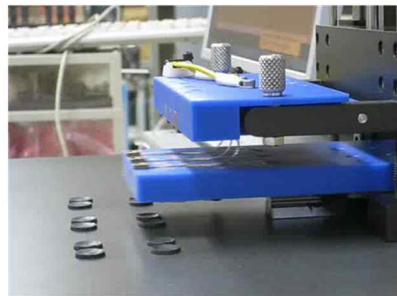


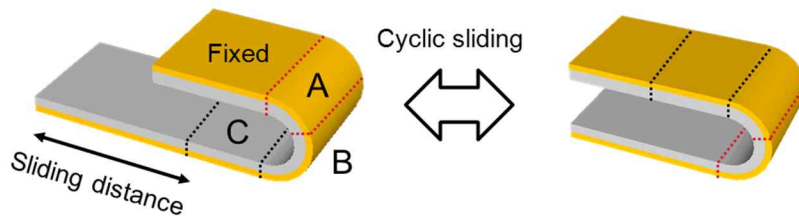
Figure 4.5. (a) *In-situ* manipulator in the chamber providing SEM and FIB function. (b) Freely moving probe by a controller to all of the directions.

Applications, (Figure 4.6). As shown in fig. 4.6 (a), the edge of the metal thin film was fixed at the upper and lower plate on the PI sample with metal grips. The lower plate moved repeatedly back and forth in the horizontal direction at a constant rate (5 Hz) and distance (10 mm) up to 500,000 cycles, whereas the upper plate was fixed, as illustrated in fig. 4.6 (b). Through this cyclic sliding motion, cyclic load (1.1% bending strain) was applied in both A and C regions, keeping the loading order mutually opposite (fig. 4.6 (c)). In region B, a uniform strain was applied during the whole test. Therefore, fatigue-induced cracks were generated in both the A and C regions but not in the B region. From the bending direction, we can determine whether it is a tensile or a compress stress. We only evaluated for the tensile condition. Electrical resistance was recorded simultaneously using a multi-meter (Agilent 34410A), a switch box (Keithley 7007) and monitored with Labview software.

(a)



(b)



(c)

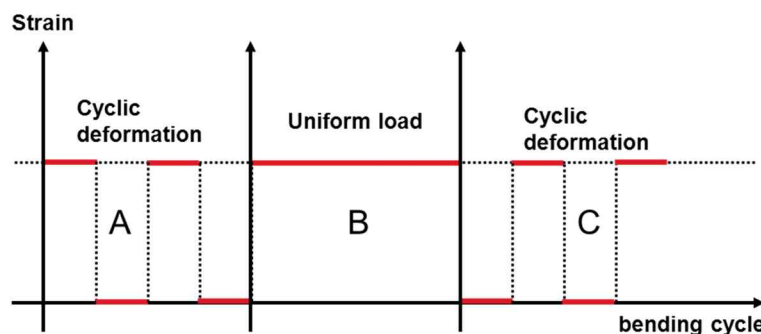


Figure 4.6. (a) Image of bending fatigue equipment (b) Free diagram: sliding motion of the metal thin film on PI (c) Applied strain and sequence by the sliding motion in the regions A,B, and C

The pouch cell battery, used in this work was assembled at ROCKET ELECTRONIC Inc. (Republic of Korea) and showed performance reliability even after 1000 bending cycles. LiNiCoAlO₂ (NCA) was used as the cathode material and the original carbon based anode material was replaced with the nano-hairy Si anode and thin film Si, as illustrated in Figure 4.7. The capacities of the anode (Si) and cathode (NCA) were approximately 0.98 mAh and 8.5 mAh, respectively; therefore, there was enough resource for the cathode materials to test the anode performance. LiPF₆ based electrolytes were used as the electrolyte solution. For the impedance analysis of the flexible battery, electrochemical impedance spectroscopy (EIS) was conducted (WONATECH, ZIVE MP2A and BioLogic, VSP-300).

The second bending test was cyclic bending, conducted with a full battery assembled as described in the last paragraph. *In-situ* voltage change was measured via bending of the full battery against a steel bar (R=12.7 mm) manually up to 3000 cycles as can be seen in Figure 4.8. The bending rate was 1 Hz (1 bending per second) and the voltage was measured using a digital multimeter (Agilent, 34410A) and Labview software.

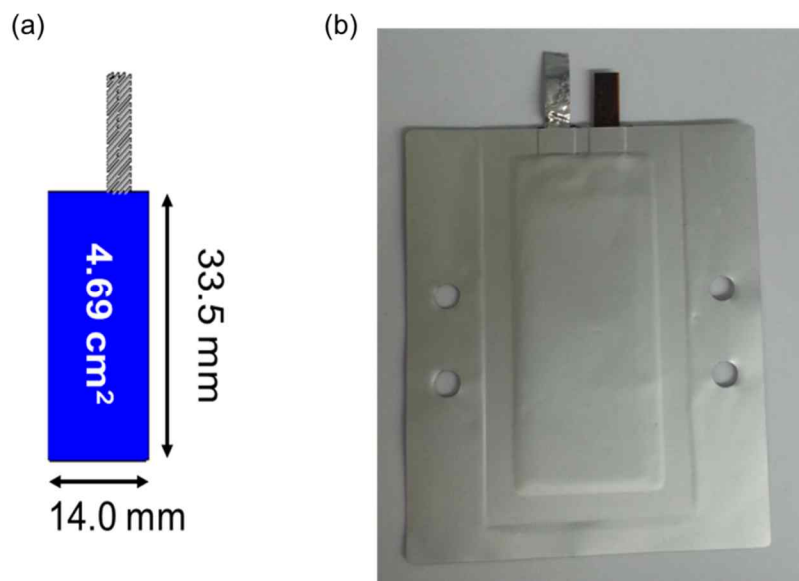
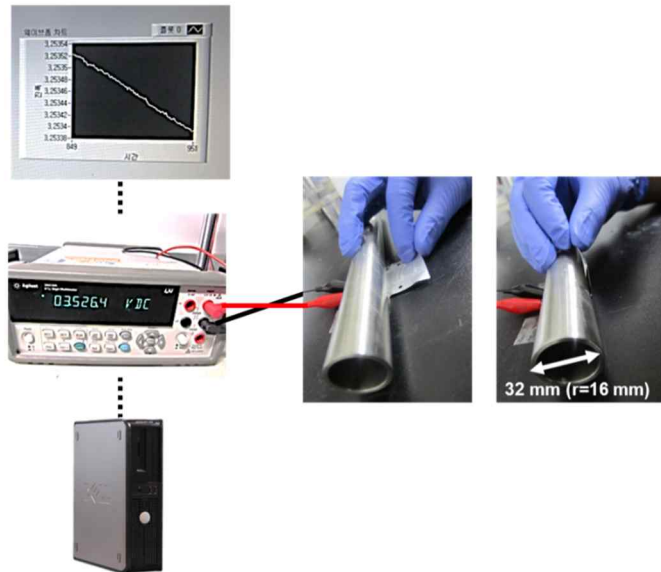


Figure 4.7. Full-cell assembling. (a) Dimension of cathode and anode electrode
(b) Full packaging battery with Si anode and NCA cathode, assembling process
is co-operated with ROCKET ELECTRONIC Inc.

(a)



(b)

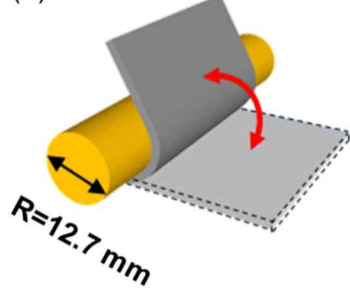


Figure 4.8. (a) Bending fatigue test using a supporting steel bar. Non-bending state (left) and bending state (right). (b) Schematic image of bending and non-bending state of a full battery

4.4. Results

Silicon-based electrodes for lithium-ion batteries face myriad of challenges: large volume changes and associated stress-induced fracture, semiconducting nature of Si itself and anisotropic nature of volume expansion, depending on the facets of c-Si. The current manuscript attempts to address all of the above-mentioned challenges by designing core-shell Cu/a-Si nano hairs directly on a polymer substrate. One aspect that stands out is the ability to use bendable polymer substrate to integrate any active electrode. Additionally, a plethora of information acquired using various characterization tools and techniques have also been presented.

4.4.1. *In-situ* lithiation of nano-hairy silicon

To elucidate the diffusion process and the strain accommodation mechanisms of this nano-hairy Si anode, an *in-situ* lithiation test was first performed. Inside the SEM chamber, Li was placed on the Si anode, as illustrated in Figure 4.9 (a) and the full lithiation process of the nano-hairy Si anode could be observed. The snapshots of the movie, presented in Fig. 4.9 (b)-(f) illustrate how the individual nano-hair anodes were lithiated, indicated by arrows and dashed lines. When the top part of a nano-hair anode (arrow #1) came in contact with the Li metal, the nanostructured Si anode began to expand gradually (see Fig. 4.9 (b) and (c)), followed by an abrupt expansion that occurred within just tens of seconds (Fig. 4.9 (c) and (d)). Simultaneously, the Si hairs that are located next to #1 (marked by arrows #2, #3 and #4) showed successive expansion due to homogeneous volume expansion. These volume expansions of Si were accommodated into the free space among the nanostructured Si. Furthermore, a bundle

of Si anodes (arrows #1-#4) became laterally bent because of the push experienced from the adjacent Si anode during the volume expansion. These pliable characteristics of the polymer NWs indicate that they can endure strain by bending themselves rather than breaking, delaminating or partially fracturing. From the results of the *in-situ* analysis, we have thus, demonstrated that the individual Si nano-hair can function well as an anode electrode system and can effectively accommodate the volume expansion during the lithiation process.

The nano-hairy Si anode expanded in all directions, which represents a typical isotropic volume expansion of amorphous Si during lithiation, as schematically shown in Fig. 4.10 (a) and (b).^{19,93} The real time *in-situ* test revealed fast lithiation from the surface to the core. We also measured the increased diameter of Si on the PINWs to compare this value with the theoretical change, as indicated in Fig. 4.10 (c) and (d). The theoretical volume expansion of the Si anode is approximately 300% after the full lithiation process, and the corresponding change in length is approximately 144%. The increased diameter was experimentally measured to be $128.48 \pm 4.76\%$, which was close to the theoretical value (144%).

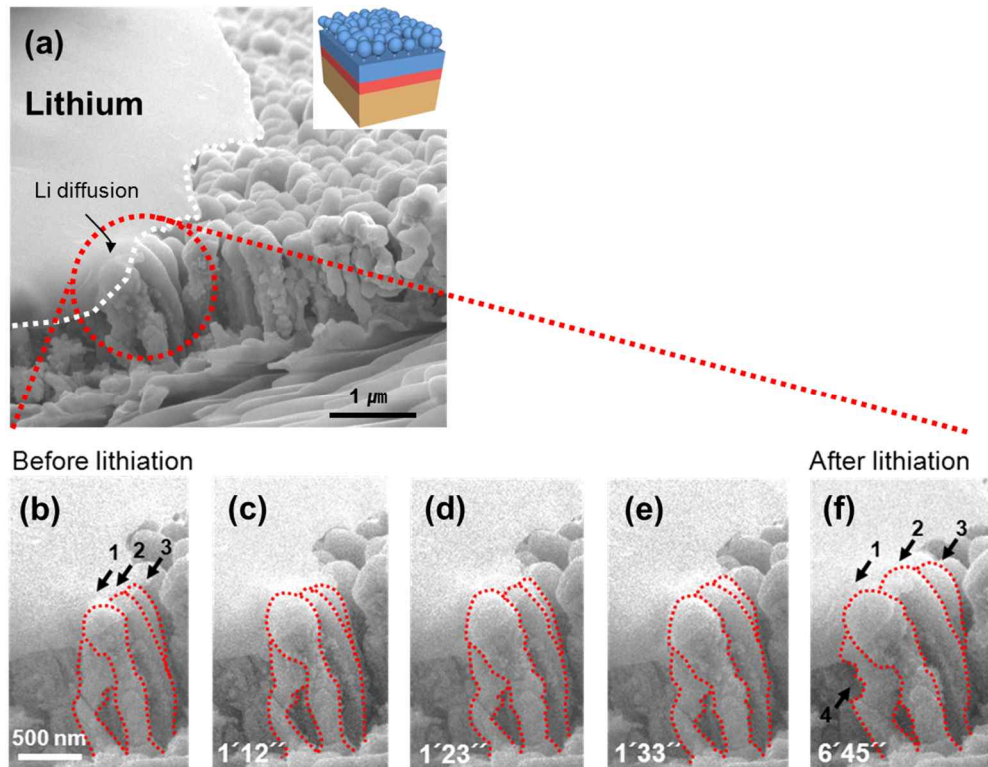


Figure 4.9. *In-situ* investigation of the lithiation process of *In-situ* Si lithiation test on nano-hairy PI through contact with bulk Li, (a) before Si lithiation and during the process of lithiation (b)-(f).

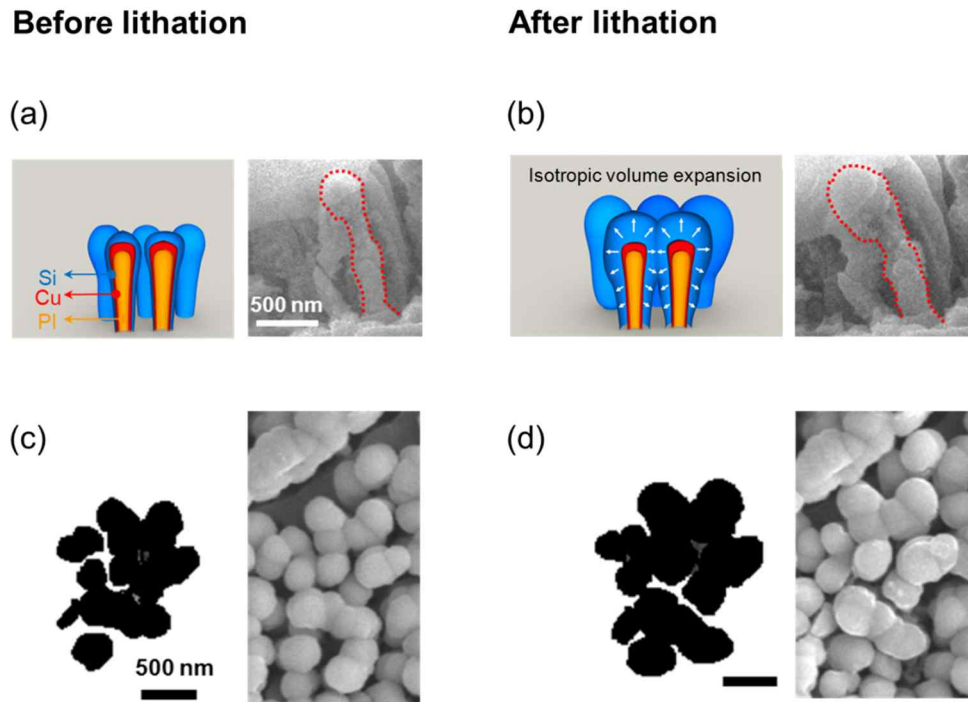


Figure 4.10. Schematic images and pictures of (a) before lithiation (b) after lithiation. Dimensional change in length during the lithiation process by the contact-lithiation method. We observed increased Si on the tip of the nanorod from the top view (represented by black dots) (c) before and (d) after the lithiation test and edited these images using an image analyzer. For selected round and independent Si heads, the change in diameter was measured.

We can also calculate the diffusivity of Li in amorphous Si from the expansion behavior as a function of time. The expansions was observed in order from 1 to 3, as shown in Figure 4.11 (a)and was quite similar to the solid-state diffusion of Li into Si. The diffusion time was approximately 19s and the diffusion length was 500-600 nm long. The Li diffusivity can be obtained from the well-known diffusion equation,

$$D = \frac{l^2}{4t} \quad (5.1)$$

where, l is the diffusion length and t is the diffusion time. The calculated diffusivity is $3.29 \times 10^{-11} \sim 5.55 \times 10^{-11} \text{ cm}^2/\text{s}$ as shown in Fig. 4.11 (b). Since our result is akin to other reports, the current experimental methods seem suitable and correct to estimate the diffusivity of amorphous Si. The current experimental methodology also enables one to know the diffusivity without an SEI layer because the current technique was applied to a solid-state system and not in any liquid electrolyte system, which is commonly found in the past reports (Fig. 4.11 (b)). Li diffusivity can be hindered by the SEI layer on the Si surface. In the current work, the possibility of SEI formation was excluded and tried to obtaining a practical value for amorphous Si was attempted for the first time without any applied potential.

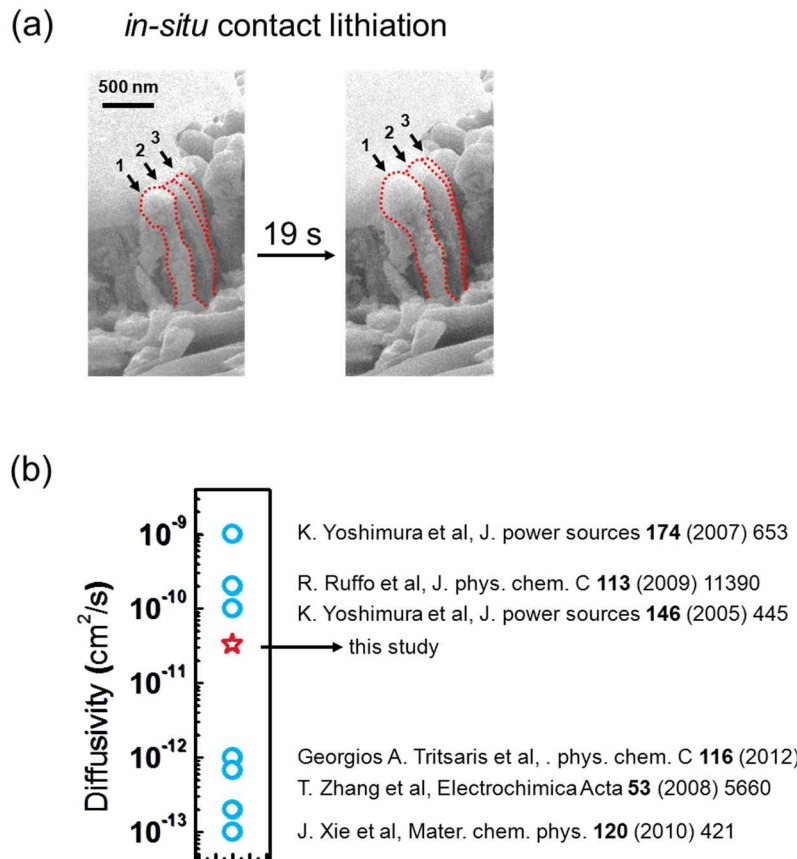


Figure 4.11. (a) In-situ lithiation test of nano-hairy Si. Si is expanded one by one from #1 to #3 for 19 seconds. (b) Literature values of diffusivity of Li^+ in amorphous Si. The current result is comparable with the reported values.

4.4.2. Improvement of electrochemical performance

We then tested our nano-hairy Si anode using a coin-type cell to investigate its electrochemical stability and performance during a cycling test. As demonstrated in Figure 4.12 (a), a significant difference was observed in the cycling performance between the Si anode on the nano-hairy PI and a conventional Si thin-film anode on pristine PI. From the initial point to the end of the cyclic test, the Si anode on nano-hairy PI always showed a much higher capacity than the conventional Si thin-film anode on pristine PI at a rate of C/6. The capacity of the nano-hairy Si anode was stabilized at approximately 60 cycles (Figure 4.13), after which the capacity value was approximately 1573 mAh/g at the 100th cycle, which is comparable to the capacity decay previously observed for Si thin film on a metal (Cu) substrate.^{21,22,94,95} By contrast, the cycling capacity of the conventional Si thin film on pristine PI decreased rapidly after the 1st cycle and was 131 mAh/g at the end of the test (at cycle 100). Hence, the nano-hairy structure significantly improved the battery performance of the Si thin film on the PI substrate. To understand the different cycling behaviors for both the samples from their early stages, the cycling test was stopped immediately after the first lithiation process and the surfaces were characterized using SEM and energy dispersive spectrometer (EDS), whose results are presented in Fig. 4.12 (b) and (c). For the conventional thin film Si anode on the pristine PI substrate, a significant amount of compressive stress developed because the large volume expansion of Si during lithiation was constrained by the Cu current collection layer and the pristine PI substrate. To relieve the compressive strain energy, mechanical failures such as buckling, the formation of cracks and film delamination were inevitable, and have been observed in many film-substrate systems that were subjected to excessive stress.^{22,30,71,73,96} For

instance, we observed the formation of buckling at locations (i) and (ii) in Figure 3b, which corresponded with a telephone cord-like buckle (i) and a circular buckle (ii), respectively. We also observed a large area of Si delamination, as shown in Fig. 4.12 3b-iii, which was confirmed by EDS analysis. The EDS results indicated that the Cu layer was stably attached to the pristine PI substrate; however, the Si film had largely peeled off through the circular buckle (ii) and severe delamination (iii). This delamination caused a rapid decay in the capacity, right from the initial cycle. By contrast, no buckling or delamination were observed on the active anode structure for the nano-hairy Si electrode on the nano-hairy PI, as illustrated in Fig. 4.12 (c). After the first lithiation test, cracks formed on the surface of the solid-electrolyte interphase (SEI) layer but no delamination of the active material (Si) was observed. The EDS analysis revealed that the Si and Cu films were not delaminated from the nano-hairy PI structure. As observed in the *in-situ* test, the individual Si on the nano-hairs appeared to be stably lithiated and well adhered to the substrate, such that the capacity of Si on the nano-hairy electrode did not decrease rapidly compared to that of the Si thin film on the pristine PI. This result indicates that preventing the active material (Si) from mechanical fracture is the key to secure the abrupt capacity drop. Notably, the capacity decreased very gradually as the cycle number increased to 100 in Fig. 4.13. This decrease is possibly due to the growth of the SEI layer, which also reduced the diffusion of the Li ions into the anode.⁹⁷

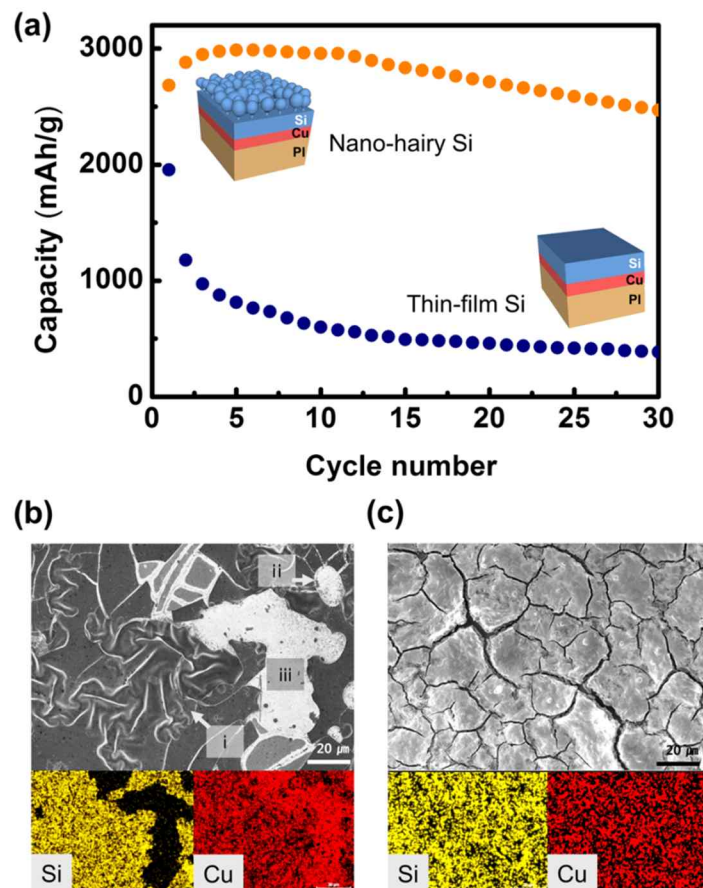


Figure 4.12. Coin-cell test: (a) Capacity on delithiation step of Si on pristine and nano-hairy PI tested using a half-cell, and surface morphologies after the first lithiation test and EDS mapping results (b) on pristine PI with buckles (i and ii) and Si delamination of the Si film (iii) and (c) on a nano-hairy PI

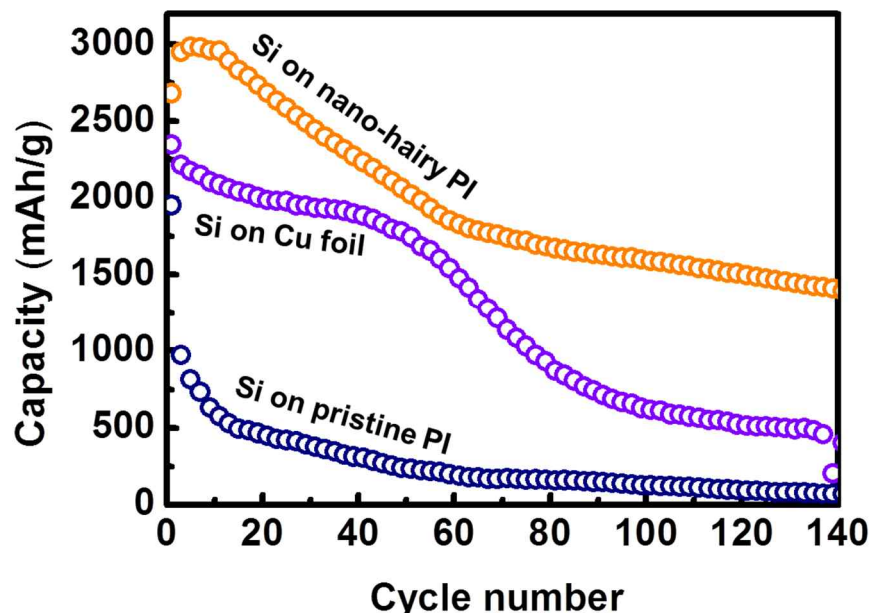


Figure 4.13. Discharge capacity of (a) Si on nano-hairy PI, (b) thin-film Si on Cu foil and (c) thin-film Si on pristine PI up to 140 cycles.

The rate capabilities at various charge and discharge rates were also investigated. In general, the nanostructured Si anode possessed a good rate capability due to its short diffusion length. The *in-situ* test clearly revealed a good transport behavior and mechanical stability of the individual nano-hairy Si anodes. Hence, a good rate capability was also expected, comparable to similarly designed nanostructured Si anodes fabricated on metal substrates.⁹⁸ The cell was first cycled at C/20, and the cycling continued using a stepwise increase to as high as 10C. As shown in Figure 4.14 (a), the polymer/Si core/shell structures exhibited outstanding rate capabilities. The initial capacity was 2790 mAh/g for the last cycle of the lowest C-rate, C/20 (20 μ A), and the capacity decreased to 48 mAh/g at the highest C-rate, 10C (4 mA). However, the capacity recovered to 2775 mAh/g at C/20 when the rate returned to the initial C-rate, demonstrating an excellent reversible performance. In spite of installing the battery system on the insulating polymer substrate, the obtained value of the capacity is relatively high for nano-structured Si anodes in comparison with the already reported literature values.^{25,99} Coulombic efficiency (CE) is another important factor for evaluating a battery performance. The CE of the first cycle was very low possibly because of the formation of a SEI layer, which may be due to the consumption of some of the lithium ions.²⁷ The recorded CE was as high as 98-99 % at a rate of C/20. Fig. 4.14 (b) plots the charge/discharge profiles of the last cycle for the same C-rate corresponding to Fig. 4.14 (a). These profiles have the typical potential profiles of silicon between 0 and 2 V¹⁰⁰ and indicate a consistent behavior of amorphous silicon,^{101,102} as presented in Figure 4.15. A dashed line (C/20') means a charge/discharge profile of a returned C-rate followed by 10C, and the capacity was recovered to almost the same value as the initial capacity at a rate of C/20 (99.46 % of capacity recovery), showing an

excellent reversible performance. The performance of our nano-hairy structure is even comparable to the Si anode on the metal substrate.^{21,22,25,94,95,19,93}

By contrast, very poor rate capabilities were obtained from the conventional thin film Si anode on pristine PI, as shown in Figure 4c. From C/20 to C/2.5, the capacity was considerably lower than that of the nano-hairy Si anode, and the CE was also unstable and low. The charge and discharge hardly occurred between 1 C and 10 C. C/20' (returned C-rate) was not recoverable (18.93 % of capacity recovery) when compared with the nano-hairy Si anode. After the rate capability test, we observed significant morphological differences between the nano-hairy and thin film Si anode structures, similar to the aforementioned cyclic performance test, as presented in Figure 4.16. Although the thin film Si anode on the pristine PI substrate was severely delaminated, no delamination was observed for the nano-hairy Si anode after the C-rate test. Thus, the capacity of our Si anode was reversibly recoverable without a capacity drop when the C-rate returned to its initial value, whereas the conventional thin film Si anode on the pristine PI severely peeled off, which induced poor rate capability and capacity recovery.

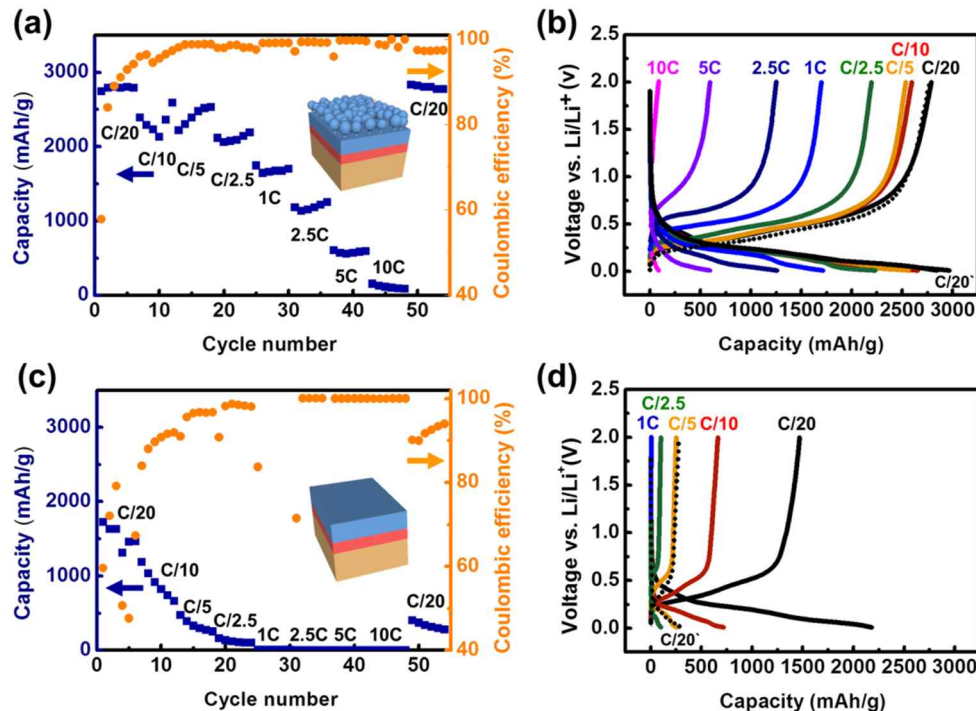


Figure 4.14. (a) A rate capability test and (b) charge/discharge profiles (of the last cycle at the same C-rate) at various C-rates for the Si on nano-hairy PI. (c) A rate capability test and (d) charge/discharge profiles (of the last cycle for the same C-rate) at various C-rates for the Si on pristine PI.

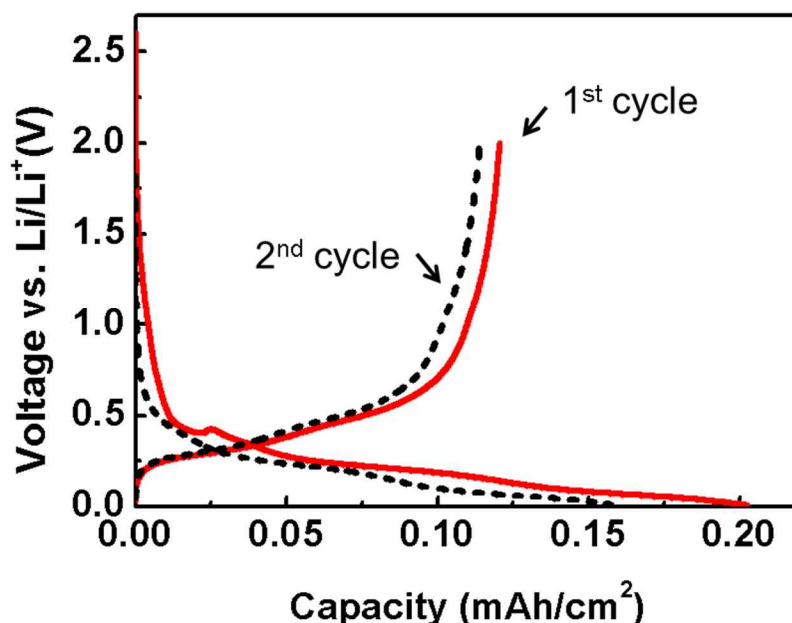


Figure 4.15. First and second charge-discharge profile of Si. The lithiation potential has a sloping profile between 0.1 and 0.01 V, reflecting the behavior of amorphous silicon. A plateau was also observed at approximately 0.4 V at the first discharge graph, corresponding to SEI layer formation.

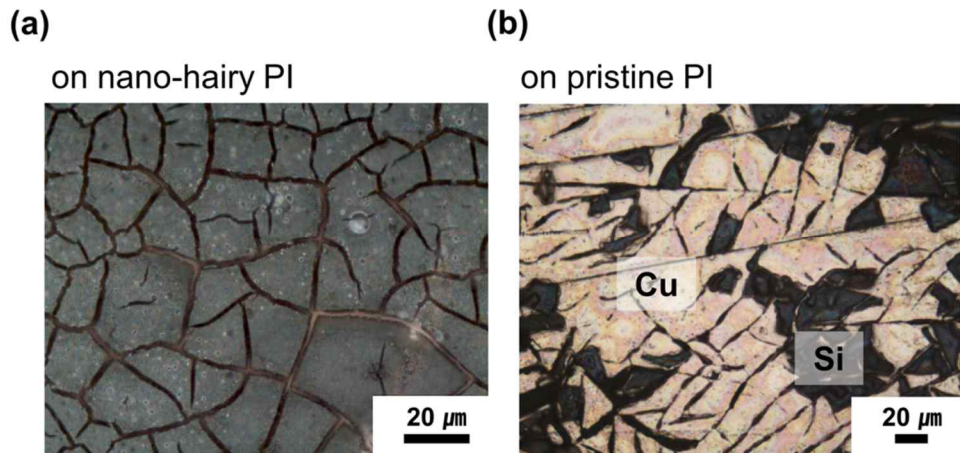


Figure 4.16. Morphology observation after the rate capability test. (a) A SEI layer (dark green) covers the polymer/Si core/shell structures without any delamination events on the nano-hairy PI substrate. (b) The Si film was severely peeled off, and the exposed Cu layer (yellow) was wider than the Si islands, thus indicating a loss of active material.

To investigate the cycling performance at a full battery level, we assembled a full pouch-cell battery made of Si anodes. Collaborating with Rocket Electronics Company, the pouch cell was designed and fabricated by commercial means, using a bendable Li-ion pouch cell battery with LiNiCoAlO_2 (NCA) cathode. Figure 4.17 shows the galvanostatic cyclic performance of the pouch cell batteries made of the nano-hairy Si anode, compared with that of the thin film Si (100 nm) at various C-rates. Similar to the results from the coin-cell tests, the capacity of the pouch cell with the nano-hairy Si anode was always higher than that of the thin film Si anode for the entire range of C-rate from 3C/3.3 to 6C and the corresponding voltage range 2.4-3.7 V. The main reason for the large capacity difference between Si on nano-hairy PI and thin film Si on pristine PI can also explained by the electrochemical impedance spectroscopy (EIS) results, shown in Figure 4.18. The EIS was measured using a full flexible battery after the C-rate test (charged state). The generally accepted interpretation is that the first semi-circle in the high frequency (HF) region accounts for the resistance of the SEI film, and the middle frequency (MF) semicircle is related to the impedance of the charge transfer reaction at the interface of the electrolyte and the active material.¹⁰³ The straight line corresponding to the Warburg impedance in the low frequency (LF) region stands for the diffusion of Li^+ into the electrode.¹⁰⁴ In our case, we observed two semi-circles, one in the HF (~20k Hz) and the other in the MF (~250 Hz) regions, as observed in Fig. 4.18 (b). The second semi-circle for Si on nano-hairy PI is much smaller than Si on pristine PI, indicating a smaller charge transfer resistance that resulted in a higher capacity performance. We postulate that the high surface area of the nanostructured Si constructs a high electrode/electrolyte interface, inducing the active charge transfer process. The slope of the Warburg impedance of Si on the nano-hairy PI is also greater than that of the thin film Si on pristine PI, implying that the Li^+ diffusion process is easier for the

nano-hairy Si.¹⁰⁴ These characteristics are attributed to the enhancement of the electrochemical performance of the nano-hairy Si anode.

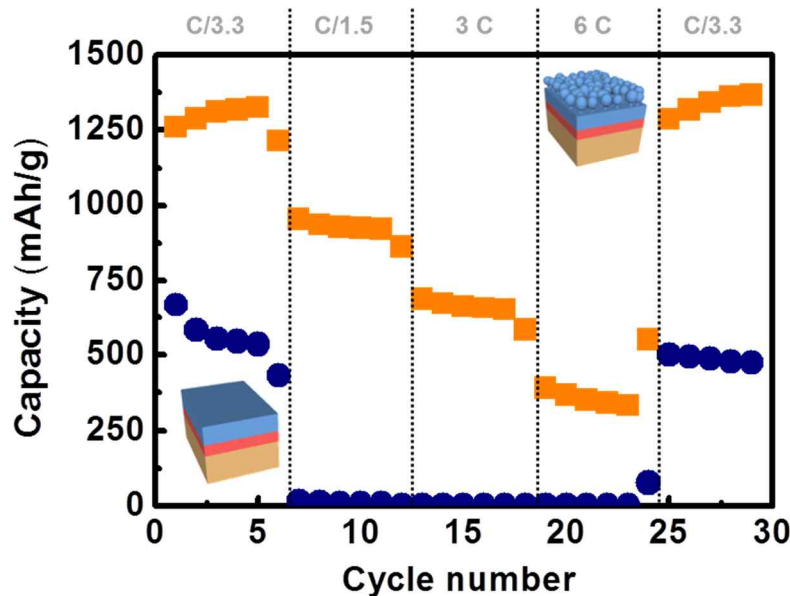


Figure 4.17. A rate capability comparison of electrochemical and mechanical responses with the pouch-cell batteries made of a nano-hairy Si anode (orange) and a thin film Si anode (navy) on PI substrates.

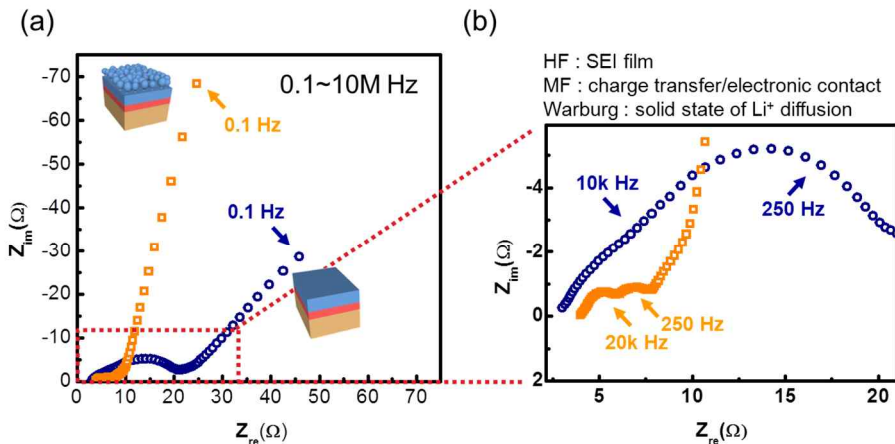


Figure 4.18. Electrochemical impedance spectroscopy (EIS) results for Si on nano-hairy PI (orange square) and Si on pristine PI (navy circle) (a) in a high frequency region and (b) low frequency region.

4.4.3. Improvement of electrical stability

For flexible or bendable electronics, both mechanical and electrical stability should be guaranteed for repeated bending conditions. Furthermore, for bendable batteries, the current collector layer should also be reliable and stable for repeated bending conditions. When the resistance of the current collector increases due to cracking or delaminations, battery performance is deteriorated w.r.t. impedance. Hence, a fatigue-free electrode is always desirable for flexible and bendable batteries. We investigated both the mechanical and electrical stabilities of the Cu current collector under the cyclic sliding condition to evaluate its possibility for flexible applications. The mechanical stability of a full battery under cyclic bending condition was also tested.

To evaluate the robustness of the current collector on the polymer substrate, we introduced a bending fatigue equipment. (see more information in Fig. 4.6) We cycled the Cu on pristine PI and nano-hairy PI upto 500,000 cycles. The initial resistance was 4.17 and 5.78 Ω , respectively. Resistance of Cu on nano-hairy PI was slightly higher than that of Cu on pristine PI. The electrical resistance change was plotted against cycle numbers as shown in Figure 4.19. The resistance of Cu on pristine increases dramatically with the cyclic bending deformations. The final resistance was 17.35 Ω , corresponding 300% change in electrical resistane w.r.t. the initial value. However, Cu on nano-hairy PI shows a stable behavior. After the 500,000 slidings, the electrical resistance increased only less than 10%, corresponding to 6.36 Ω . The resistance change of nano-structured Cu was saturated before 10,000 cycles. Formation of crackswas the main reason for the increase of resistance in both the samples. Several cracks on the pristine PI could be easily observed because the Cu thin film was very susceptible to crack formation and propagation under the cyclic bending fatigue

condition. By contrast, Cu on nano-hairy PI delayed the crack initiation and hindered the propagation through the nano-hole structures by crack blunting effects.¹¹¹

4.4.4. Improvement of mechanical stability

As mentioned earlier, two different mechanical stress evolutions have been focussed. Si based anodes (as well as high capacity materials, such as Sn, Bi, Ge, Al, and etc having large volume expansions in common),⁷ used in the current work, undergo huge volume changes inducing intrinsic stress borne out of the materials themselves. In the last chapter, it has been demonstrated from electrochemical tests that our novel design could successfully accommodate this intrinsic stress, showing no delamination events compared to the Si thin film anode. The second stress evolution comes from the mechanical deformations (i.e. flexible, bending, twisting and folding) observed. Since the battery deforms under these conditions, severe extrinsic stress was applied in the battery system.

We set the cut off voltage at 1 mV and disconnected the Li insertion test to understand the nature of lithiation of the Si anode at a very early stage. After the first lithiation step, the surface morphology and composition of the sample were investigated. Si coated nano-hairy PI were buried under the thickly grown SEI layers and micro-cracks were generated on the surface as shown in Fig. 4.20 (a) and (b). This thick SEI formation

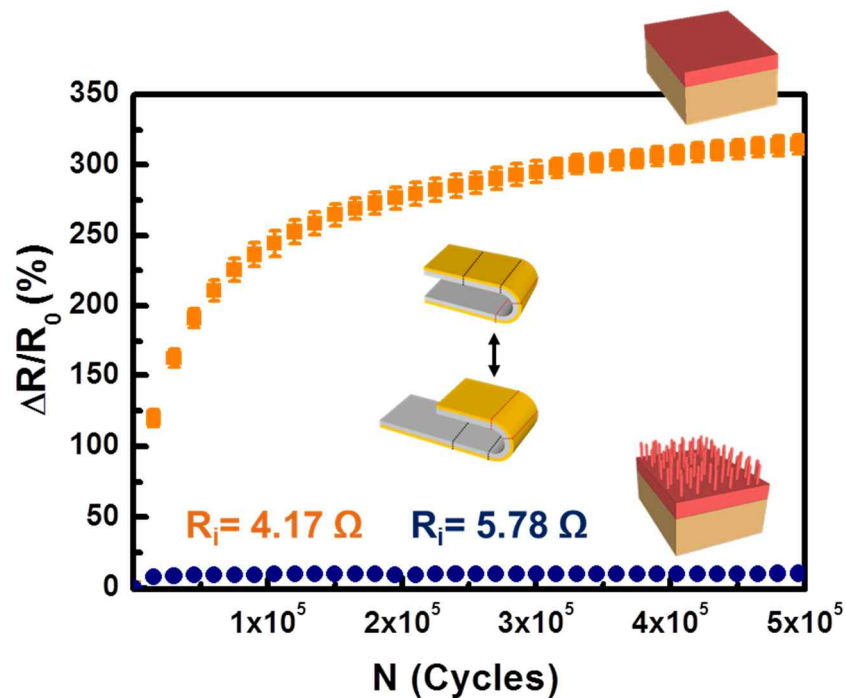


Figure 4.19. Change of electrical resistance versus number of cycles in a bending fatigue test of Cu on pristine PI and on nano-hairy PI.

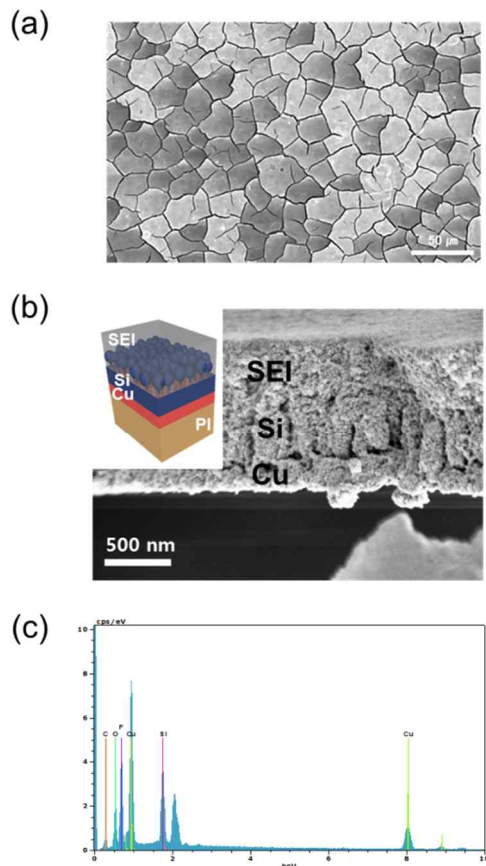


Figure 4.20. (a) Cracked surface of SEI/Si body and EDS mapping results of Cu and Si after the lithiation test. No delamination of Cu and Si was detected (b) SEI covered nanostructured Si (SEI/Si body) on the Cu layer by filling the free space above the Si nano-hairs and covering trend illustrated with a schematic image (inset) (c) compositional analysis of SEI/Si body

on Si nanostructures and surface cracking of SEI layer that have been observed in this research is similar to other various studies reported in the past.^{27,105} However, the primary difference between the current work and other studies is that, the cracks, in this research were formed very uniformly and surprisingly all have the similar crack length. Through the EDS analysis in Fig. 4.20 (c) it was known that, the SEI layer consisted of the main element of the electrolyte, such as carbon (18.11%), fluorine (7.15%), and phosphorus (1.15%) that comes from the decomposition products of 1M LiPF₆ in EC/DEC (1:1) electrolyte and oxygen (34.62%). The oxygen mainly comes due to exposure of the samples to the air during their handling.

While charging at 1 mV it has been observed that, much of the particle-like SEI covered the substrate and filled up the free space around the Si nano-hairs, resulting the whole thing to appear as a one continuous film, as illustrated in Fig. 4.20 (b). SEI covering is supposed to be the reason for the very conducting metallic current collector (Cu) on both of the substrate and PI nano-hairs, providing a preferential nucleation sites forming the one-continuum body with SEI products.¹⁰⁵ In the continuous SEI layer, the compressive stress developed due to volume expansion from lithiation of Si becomes equal throughout the system. This compressive stress was further released through formation of uniform cracks (see Fig. 4.20 (a)).

It is already known that, the formation of SEI causes deterioration of battery performance due to the following drawbacks: consumption of electrolyte and lithium ions, weakening the electrical contact between the current collector and active material due to the electrically insulating nature, long lithium diffusion distance through the SEI layer, electrode material degradation by mechanical stress. Furthermore, surface cracking of the SEI layer can even exacerbate the battery performance due to further SEI formation on the newly exposed surface of the active material in the electrolyte.¹⁰⁶⁻

¹¹⁰ Figure 4.20 (a) shows that, SEI covered Si nano-hairs were broken up into individual pieces by interconnected cracks having very similar crack length. The formation of micro-cracks in the Si thin film is associated with energy release rate.^{30,62,63} When the strain energy release rate exceeds the fracture resistance, crack propagation in the film or at the interface between the substrate and the film occurs. Since this energy release rate is a function of thickness of the Si thin film, thicker the film is, larger is the release rate of the strain energy, inducing a film fracture. Therefore, thickness information of the electrode system is important as it gives a picture of the crack formation trend. In this study, since the thin film electrode was not designed directly by us, the thickness of the Si layer was estimated by considering two factors. First, Si agglomeration at the tip of the nano-hairy PI was dense and continuous, which would behave as a thin-film-like one-layer. The corresponding thickness of the Si was approximately 300 nm. Now under these conditions, we can bridge between particular crack spacing and improved cycling performance with theoretical considerations.

Generally, a fracture tends to occur at the weakest point of a surface, such as defects or voids due to stress concentration. In the current study, evenly placed Si nano-hairs distribute the stress evenly, from where micro cracks can generate, instead from any preferential cracking sites or directions. However, the accurate point of the crack initiation was not clear, calling for further investigations by introducing the concept of minimum crack spacing, L_{cr} , a length smaller than which no additional cracks can form between the two already existing neighboring cracks. Below the L_{cr} , it is not possible to insert a new crack because the stress in Si is not enough to reach the plastic flow stress of the lithiated Si. On the other hand, new crack formation occurs when the length of already existed crack length is above the minimum crack spacing because the accumulated stress can exceed the plastic flow stress of the continuum body. In our case,

plastic flow stress of SEI is much smaller than that of the lithiated Si, therefore, we may only focus on the stress of lithiated Si.

For a crack with a crack length above the minimum crack spacing, two competitive options exist as the stress relaxation route. One of them is the formation of a new through-the-thickness crack insertion between the neighboring cracks and the other option is an interfacial delamination from the edge of the body to decrease the energy release rate. The elastic energy release rate related to crack growth decreases with the interfacial crack length, whereas surface energy increases at a constant rate as shown in Figure 2.15.^{60,73} When the elastic energy of a system is completely consumed to create new surfaces, the interfacial crack length is arrested because there is no more energy available for further crack growth.^{60,73} This correlation between elastic energy and surface energy determines whether half or full delamination will occur induced by the crack length. For more detail approaches using theoretical calculations, interested readers are directed to review the critical crack/delamination length model by Haftbaradaran *et al.*^{60,73} They tried to deduce the critical fracture size on patterned Si patch during the lithiation process at the onset of a delamination crack and after full delamination in the presence of a large amount of interfacial sliding under the plain strain condition. They demonstrated that the theoretical treatment and the experimental observations were in excellent agreement. In this work, the uniformly separated SEI/Si islands bounded by cracks can be assumed as patterned Si patches, described in Haftbaradaran's work. By introducing this model, we use the following equation to expect the critical delamination length,

$$l \geq l_{cr,del} = \sqrt{\frac{6hE\Gamma}{(1-\nu_f^2)\tau_0^2}} \quad (2.26)$$

The critical length of crack nucleation ($l_{cr,nuc}$), which is actually an interfacial edge crack between the film and that substrate, can be calculated from equations (2.25-2.26). Before applying the above model and the related formulae, the transformation of the stress energy in the film to the surface energy, in order to release the strain should be considered. The intrinsic stress developed from the volume expansion is totally consumed to create new surfaces and equation (2.26) is applicable as long as this condition is satisfied. In this state, the delamination interface should be identified. Figure 4.21 shows the delamination of the Cu layer from the nano-hairy PI substrate. Therefore, various parameters for Cu and PI are to be used. Thickness of the Cu is 200 nm here, Young's modulus and Poisson's ratio of Cu is 130 GPa and 0.36, respectively,¹¹¹ Interfacial shear stress, τ_0 is 40 MPa¹¹² and interface energy lithiated Si, Γ , is 25 J/m².⁸³ The crack length inducing full delamination were of island sizes and were calculated as $2l_{cr,del} = 105.8 \mu m$. This signifies that, delamination cannot occur if the crack length of a Si island is below $105.8 \mu m$. This is just in accord with Figure 4.22 (a). The most effective way to release the stress is creating surfaces as large as possible in the film. The terminal morphology of the film surface had many uniform cracks with similar length scale. We consider that this morphology is the shape, which can provide the largest surface. The main reason for not seeing too many fine cracks is that the crack spacing between the neighboring cracks was below the minimum crack spacing. As all of the crack lengths were equal to the critical delamination length in Fig. 4.22 (a), mostly no delaminations were observed. However, very rarely, delamination occurred as shown in Fig. 4.22 (b). The figure shows that a delamination crack is initiated from the edge of the body. The crack length was approximately $148 \mu m$, and was above the critical delamination length, leading to peeling off from the substrate. Once a crack length of

the Si/SEI islands exceeded the critical crack delamination length, partial or full delamination occurred, inducing a rapid capacity decay of the battery performance, i.e. when $2l > 2l_{cr,del}$. The experimental results of this research showed a good agreement with the critical fracture model, suggested by Haftbaradaran's work.^{30,73} As already mentioned before, a crack formation is rather helpful in terms of stress relaxation, whereas delamination of active material is absolutely a fatal failure for the electrode stability. In the current work, delamination events of Si anode could be successfully prevented through uniformly patterned cracks below the anti-crack delamination length, which rather improved the cyclability of the Si anode electrode. We presume that the reason for the formation of surprisingly uniform cracks is the wide and even distribution of the Si nano-hairs.

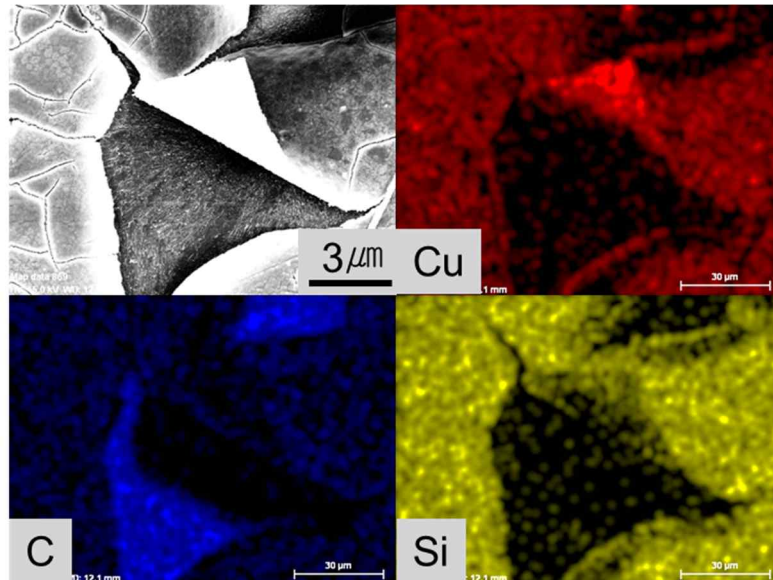


Figure 4.21. Delamination of nano-hairy Si after lithiation. EDS analysis of Cu, C, and Si. Cu is mainly peeled off from PI substrate. Si is well attached onto the PI substrate unlike the Si on pristine PI

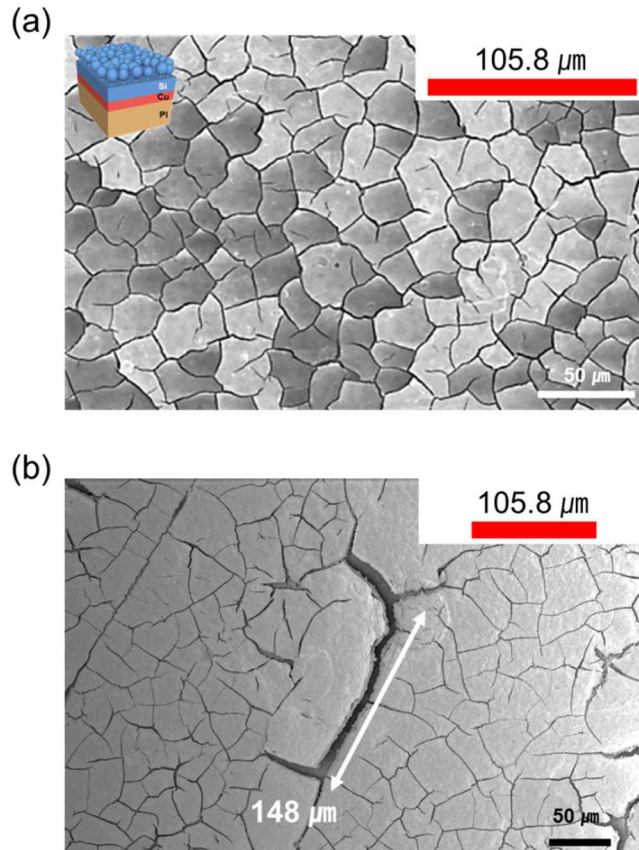


Figure 4.22. (a) Uniform crack initiation on Si on nano-hairy PI. Thick SEI layer covers the entire surface. No delamination had occurred because the average crack length was below the critical delamination length ($105.8 \mu\text{m}$). However, onset of delamination was observed when the crack length was above the critical delamination length.

From this preliminary study of current collector, it has been proved that the nano-hairy structure was very resistant to cyclic bending deformations and has also been applied to a full packing battery. We successfully turned on the back light unit (BLU) using our full pouch cell battery during repeated bending cycles (as well as LED lamp) (Figure 4.23 (a)). A constant voltage of 3.74 V was also maintained, as shown in Figure 4.23 (b). For quantitative analysis, we tested the mechanical stability of the nano-hairy Si and thin film Si anode against cyclic bending fatigue. The mechanical bending endurance was evaluated using voltage retention with respect to bending cycles (upto 3000 bending cycles) at a frequency of 1 Hz with a bending radius R_c of 12.7 mm, as shown in Figure 4.24 (see the testing method in the Figure 4.8). The initial and final voltages for the nano-hairy Si anode were 3.700 V and 3.702 V, respectively (100% retention), whereas the final voltage of the thin film Si anode decreased to 3.526 V. This voltage drop can be attributed to the bending fatigue effect compared to its non-bending state. We presumed that the inter-spacing between the nano-hairs could effectively accommodate the bending deformation. We also successfully demonstrated a high rate capability at various C-rate steps (Figure. 4.25 (a)) tested (Fig. 4.25 (b)). Even though, capacity of 2038 mAh/g at C/5 under bending state. In conclusion, the nano-hairy Si anode demonstrates outstanding mechanical stability against both charge-discharge induced-intrinsic stress and bending fatigue induced-extrinsic stress, which implies the feasibility of robust bendable Li-ion batteries directly embedded in PI-based full bendable electronics.

(a)



(b)

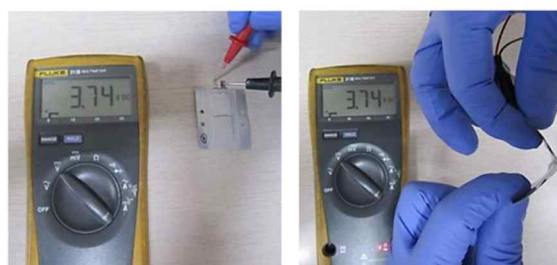
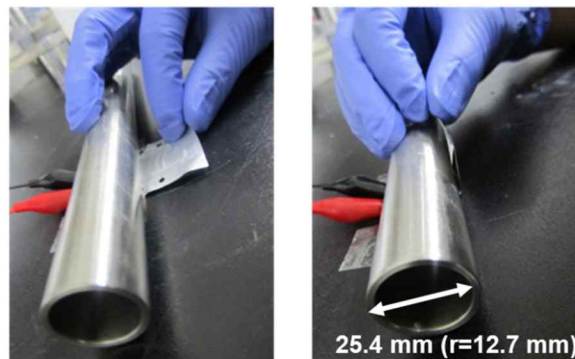


Figure 4.23. (a) A back light unit (BLU) was kept on during the bending cycles of the bendable pouch cell battery in which the nano-hairy Si anode was used as an anode and (b) the voltage of the pouch cell battery, which was maintained at 3.74 volts during non-bending (left) and bending (right) cycles.

(a)

Bending speed : 1 Hz



(b)

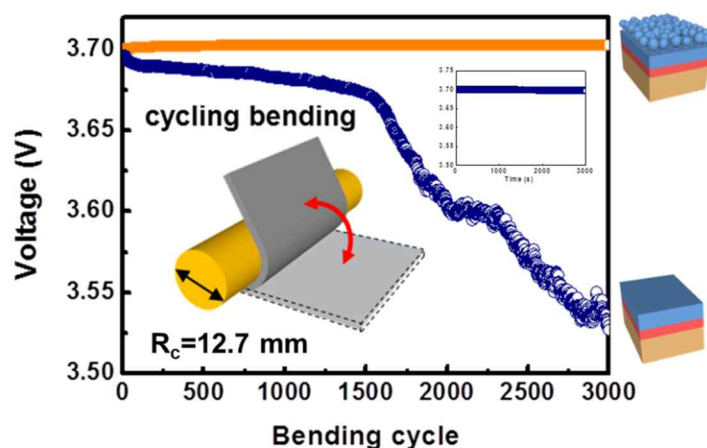


Figure 4.24. (a) Bending fatigue test using a supporting steel bar (b) voltage retention test during a cyclic bending fatigue test at 1 Hz. A full cell using a Si on pristine PI maintains the voltage at 3.7 without bending fatigue (inset)

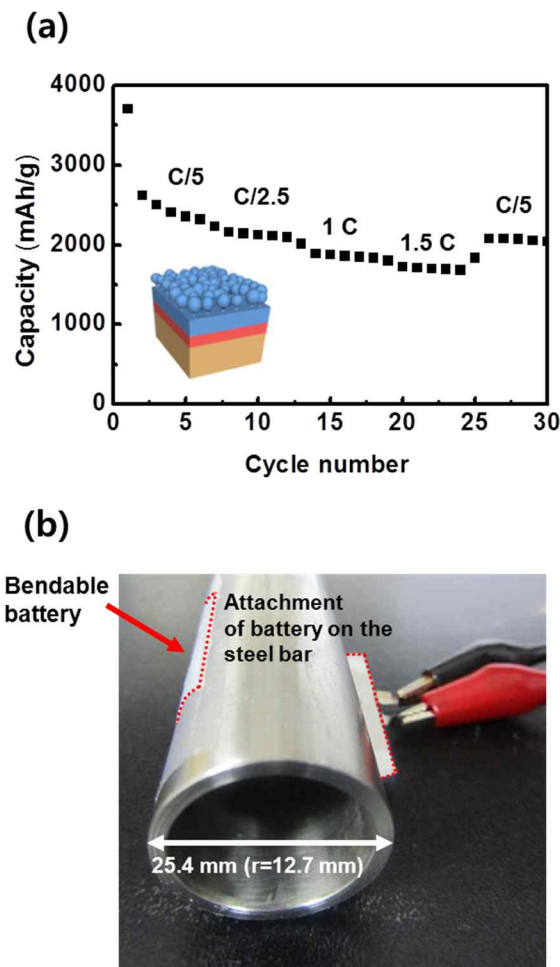


Figure 4.25. (a) Plot of discharge capacity per unit area (left y-axis) and per weight (right y-axis) versus cycle number of Si (300 nm) on the nano-hairy PI in a full pouch-cell at various C-rates. Charge and discharge was conducted from 3.0 to 3.9 V (b) under the bending status on a steel bar ($R_c=12.7$ mm)

4.5. Summary

In this chapter, we demonstrated the characteristics of nanostructured Si on polyimide substrate in comparison with Si thin film. From the *in-situ* technique we verified that, in the lithiaion process of nano-hairy amorphous Si strain accommodation could be achieved without any mechanical fracture. In the half cell test, nano-hairy Si showed a better cycling performance than the Si thin film. From the mechanical perspective, uniform cracks of SEI layer on nano-hairy Si alleviated the intrinsic stress. To this end, the interesting finding is that the length of generated micro-cracks are below the critical delamination length, preventing any peeling off. This also prevented the delamination events, inducing a longer cycle and a higher capacity. A partial edge delamination, peeled between Cu and PI interface was also observed, which meant that the delamination interface strength between Si and Cu in the Si thin film on pristine PI had been improved. The nano-hairy Si anode had a smaller charge transfer resistance and an easier Li⁺ ion diffusion process than that of a Si thin film on pristine PI, resulting in a higher capacity and an excellent rate capability for the former. In addition to this, mechanical resistance was also evaluated under cyclic deformation with a 2% strain from the current collector level to a full pouch battery. Cu on nano-hairy PI showed a stable electric behavior, only less than 10% resistance change compared to over 300% of Cu on pristine PI upto 500,000 cycles. Finally, it was possible to turn on the back light unit successfully and maintain 3.7 V under 3000 bending cycles with a 12.7 mm-bending radius. Excellent C-rate was observed also in the bent state.

CHAPTER 5

Engineering of soft substrate

5.1. Introduction

So far, we have discussed the electrical, electrochemical, and mechanical properties of nano-hairy Si anode grown on nano-hairy PI substrate, fabricated by CF₄ gas. From various tests, it was known that this nano-hairy structure of PI improved each of the above-mentioned performances than those on pristine PI. In this regard, quite a few questions arise, such as whether a control of the density of the nano-hairs and the geometric dimension would affect those properties or not? Therefore, a new gas was introduced to bring a change in the nano-hairy structure. One serious drawback of PI is that, it is an insulating substrate. Recently, graphene-based research has become one of the major interests among the researchers all around the globe. In the current work, graphene-oxide (GO) dispersed polyimide substrate have been employed, which is conductive, with a conductance just below 1 S/cm. Although this conductivity is relatively poor, it is expected that electrically unstable substances might be utilized and provide a guideline for energy storage within fabric or polymer based materials.

5.2. Geometric modification of nano-hairy structure

With a CF₄ PECVD etching process, we fabricated nano-hairy structures and already demonstrated the enhancement in electrochemical and mechanical performance. As stated earlier that, this nano-hairy structure can be modified with an inlet-gas, etching time and power. To modify the surface structure on purpose, the etching mechanism of soft substrate should be understood and detail information has been provided by Moon's group.¹¹³ Ionized gas radicals and sputtered metals (normally sputtered from the cathode or wall of chamber) can form un-etchable masks (set to express as MF) and be deposited on the surface of the soft substrate under CF₄ atmosphere. It is assumed that the diameter (or size) of the mask is determined by a group of several MFs and the etching rate. The MF thin film can actually be deposited like a conventional sputtering for a long time without any etching. However, this technique is not possible with soft substrates (consisting with carbon and oxygen chains), as they react with the inlet gas to form volatile products. If a mask is used on soft substrates, then the substrates do not come in direct contact with the inlet gas and the reaction between the two can be prevented. In this way, the nanostructures can also be preserved with any etching. When the inlet gas was changed from CF₄ to O₂, which is widely known to have a high etching rate,⁸⁶ ultra-thin and very long nano-hairy structures were obtained (Figure 5.1). This is because the size of the residue mask, MO (metal-oxygen), formed by the reaction of the cathode metal and the oxygen radical is physically smaller than MFs and can be easily distributed over the entire substrate more densely than MF. Likewise, there is not enough time to form a group of masks due to the high etching rate. The long hairy nanostructures had a diameter of 30 nm and length of 1.8 μm , with an aspect ratio (AR) of 60 (previous aspect ratio was 10 from CF₄ gas), which is a very high AR resulting in very large

surface area. Therefore, a higher cycling behavior and rate capability can be expected from this modified structure. From the bending fatigue test, it was known that, the nano-hole structure enhanced the mechanical stability of the Cu electrode. A same test was also conducted with the newly fabricated nano-hairy structure.

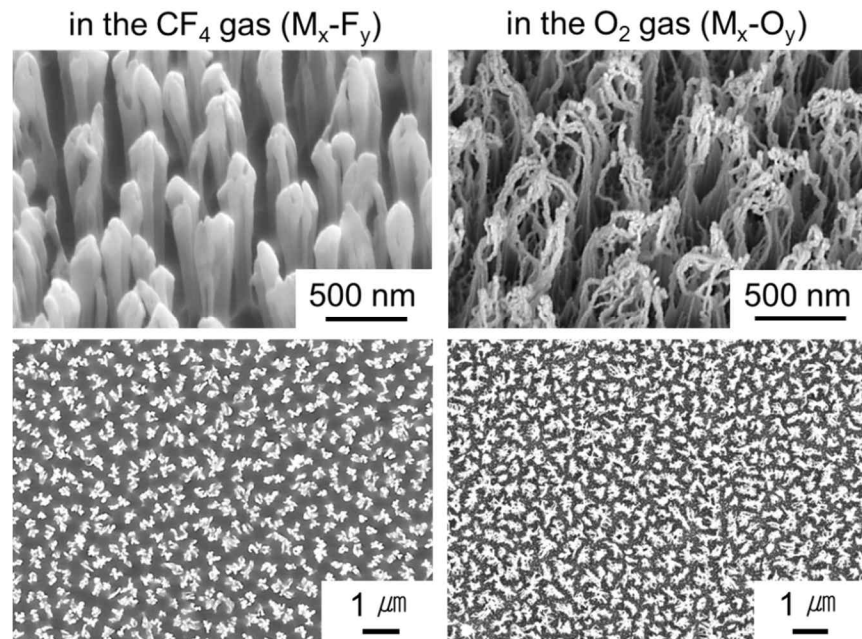


Figure 5.1. Tilted and top morphology of nano-hairy PI fabricated by CF_4 gas plasma etching process (left column) and by O_2 gas plasma etching process (right column)

5.2.1. Enhancement of electrical stability

A test, similar to that performed to characterize the Cu electrode under cyclic bending sliding motion with nano-hairy structure fabricated from CF₄ gas etching process, was conducted with ultra-thin and tall nano-hairy structure obtained from O₂ gas etching process. From now onwards, the nano-hairy structure from CF₄ etching will be denoted as CF₄-nano-hairy PI and that from O₂ etching as O₂-nano-hairy PI. To investigate the change in the electrical resistance, pristine PI, CF₄-nano-hairy PI and O₂-nano-hairy PI were prepared. A Cu layer (200 nm) was then deposited on the substrates by thermal evaporation method as shown in Figure 5.2. The initial resistance of Cu on pristine PI, CF₄-nano-hairy and O₂-nano-hairy were 2.75 Ω , 11.78 Ω , and 30 Ω , respectively. After the bending fatigue test under 4% strain condition, Cu on pristine PI showed an abrupt increase in the resistance nearly up to 7,000%, equivalent to 176 Ω (Figure 5.3. (a)). It was interesting to find that the resistance gradually increased without any saturation behavior along with the number of cycles up to 500,000. It can be assumed that the resistance may further increase, whereas for both the nano-hairy structures a saturation behavior could be seen. The final resistance of Cu on CF₄-nano-hairy PI was 16.9 Ω and that on O₂-nano-hairy PI was 34 Ω . Although the final resistance was higher for the O₂-nano-hairy PI than that for the CF₄-nano-hairy PI, the change in the resistance was lower (only less than 10%) for O₂-nano-hairy PI than that for the CF₄-nano-hairy PI as shown in Figure. 5.3. (b). To investigate the resistance change behavior, smaller samples were prepared by reducing the width (0.2 mm) and length (40 mm) and the bending fatigue test was performed under 4% strain condition (Figure 5.4). For the point of metallization on soft substrate, an increase in the density and the AR of PI is much more effective in small size electrodes because the cracks formed during cyclic

sliding on the Cu electrode largely affect the resistance change due to large scattering. The resistance in CF₄-nano-hairy PI slightly increases along with bending cycles as was observed in pristine PI with large pattern samples, whereas resistance change O₂-nano-hairy PI showed a nearly saturation behavior, signifying that no more cracks had been generated or propagated. Thus, it can be concluded that O₂-nano-hairy PI may be a more effective structure under more severely bended conditions with a nearly fatigue free behavior.

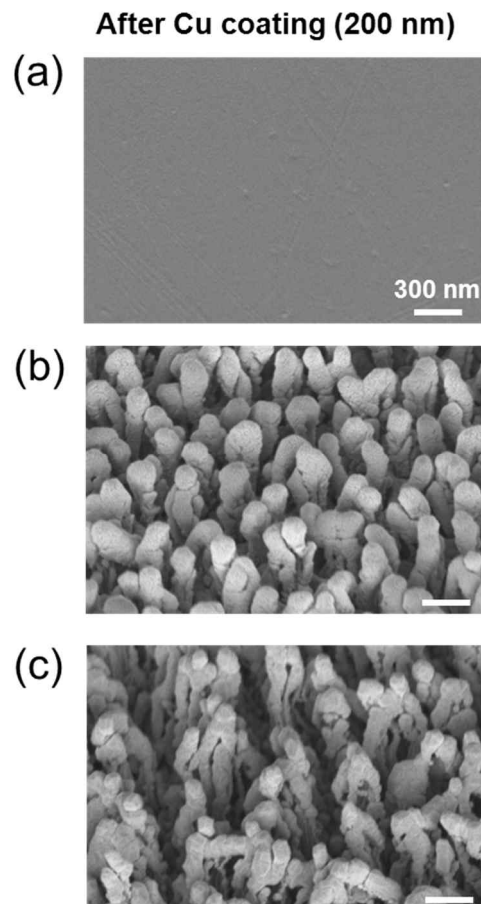


Figure 5.2. Cu deposition on (a) pristine PI (b) CF₄-nano hairy PI (c) O₂-nano hairy PI

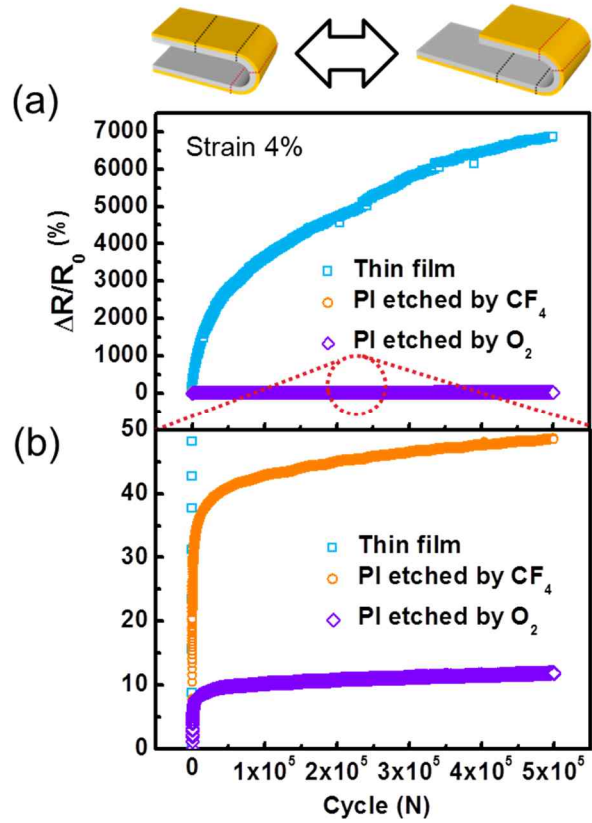


Figure 5.3. Results of bending fatigue test under 2% strain of (a) Cu on pristine PI, CF_4 -nano hairy PI and O_2 -nano hairy PI (b) enlarged graph of CF_4 -nano hairy PI and O_2 -nano hairy PI

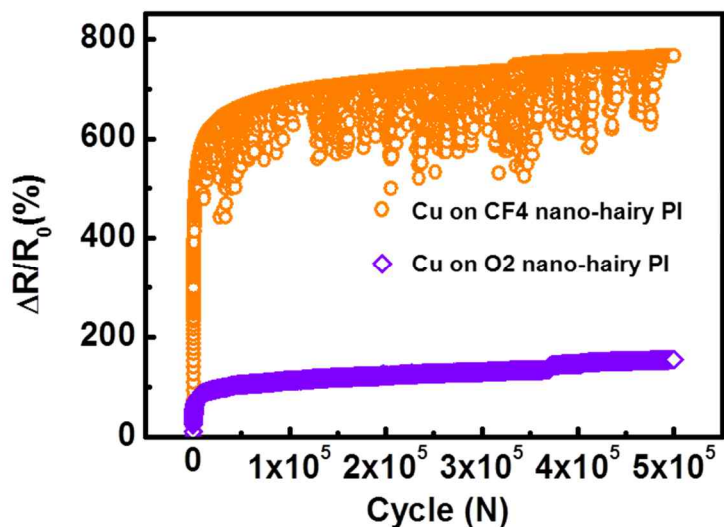


Figure 5.4. Results of bending fatigue test under 4% strain of Cu on CF₄-nano hairy PI and O₂-nano hairy PI

5.2.2. Enhancement of electrochemical performance

We already demonstrated that, the nano-hairy structures by O₂ plasma etching process showed an increased mechanical resistance to bending fatigue test. Through the introduction of O₂ plasma etching process, the resulting increase in surface area and porous space could benefit the volume changes during charge and discharge process as seen in Figure. 5.5. Fig. 5.5 shows that, the Si on O₂-nano-hairy PI, CF₄-nano-hairy PI, and pristine PI in order from top to bottom.

With a half-cell (Figure 5.6), the rate capability test was performed at various C-rates. As expected, Si on O₂-nano-hairy PI showed a better cycling behavior than those of Si on CF₄-nano-hairy PI and pristine PI. Higher capacities were obtained for O₂-nano-hairy PI at all of the C-rates. To compare the current results, a plot of capacity versus C-rates for various types of SiNWs, such as simple SiNWs, core/shell SiNWs, coated SiNWs, embedded SiNWs, and Si thin films from past references has been illustrated in Figure 5.7.^{23,25,99,101,114–126} The Si anodes with other geometrical shapes, such as Si particles, Si nanotubes, and Si powders have been excluded in Fig 5.7. The general trend is higher the C-rate, lower is the capacity. At higher C-rates, there are not many studies as compared to those at lower C-rates. For Si thin films, the capacity dramatically decreased with the increase in the C-rate. It is also to mention that, a very poor rate capability was shown by our thin film Si on pristine PI, marked as thin film (MS, standing for Min-suk). Nevertheless, we improved the rate capability dependent capacity very dramatically nearly to the highest position via introducing CF₄ etching process even with an insulating polymer substrate. A further increase in the capacity with increase in the rate capability was achieved through the O₂ etching process. The capacity obtained from Si on O₂-nano-hairy PI showed the highest value than the other

literature values. Moreover, the rate of capacity recovery, i.e. returning to the initial capacity value after the C-rate increase, was also excellent for Si on O₂-nano-hairy PI..

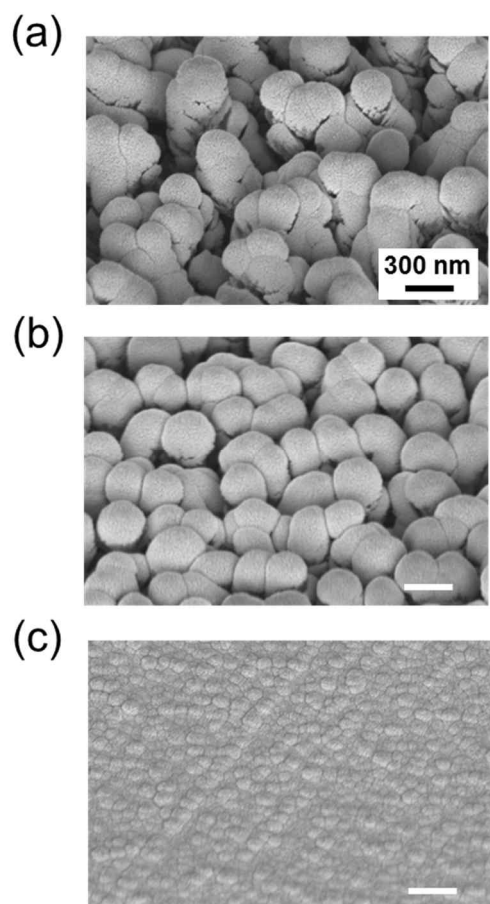


Figure 5.5. Images of Si on Cu coated (a) O₂-nano hairy PI (b) CF₄-nano hairy PI and (c) pristine PI

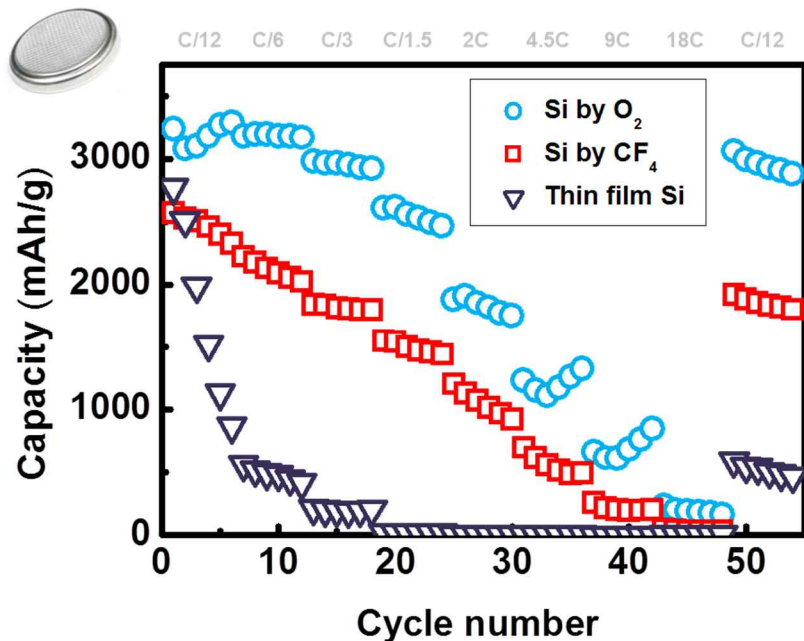


Figure 5.6. Rate capability test of Si on O₂-nano hairy PI, CF₄-nano hairy PI and pristine PI with a half-cell.

Subsequently, we also performed a C-rate test with full pouch batteries (see Figure 5.8) but the capacity results were not up to par with some of the recent advances and the theoretical capacity value. However, Si on O₂-nano-hairy PI showed a reproducible higher cycling performance (Figure 5.8). In the first place, we thought that this behavior was possibly due to the large surface area and higher density effects, as compared to Si on CF₄-nano-hairy PI. However, electrochemical impedance was also found to affect largely the cycling and rate capabilities as indicated in Figure 5.9. As shown earlier that, Si on pristine PI and CF₄-nano-hairy PI have clearly different impedance behavior. Unlike on CF₄-nano-hairy PI, at high C-rates, the Si on pristine PI could not participate in the charge and discharge process in both the half-cell and the full-cell. This is because the impedance was much higher for pristine PI than that for CF₄-nano-hairy PI. Thus, it can be concluded that, a lowering of the electrochemical impedance was very essential to improve the electrochemical charging and discharging process. Using nano-hairy structure was very helpful for those reactions. Si on O₂-nano-hairy PI, with much lower impedance than the other samples, showed a higher capacity.

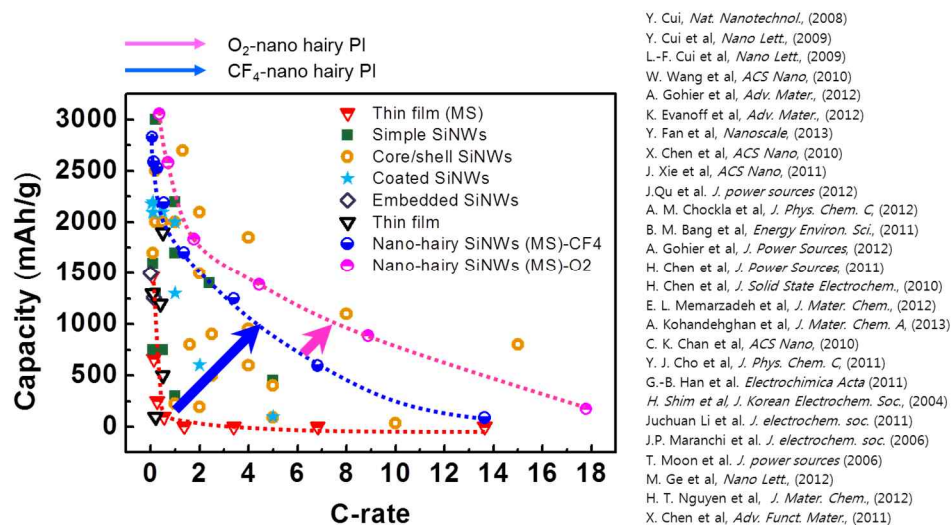


Figure 5.7. Plot of capacity vs C-rate for various types of SiNWs

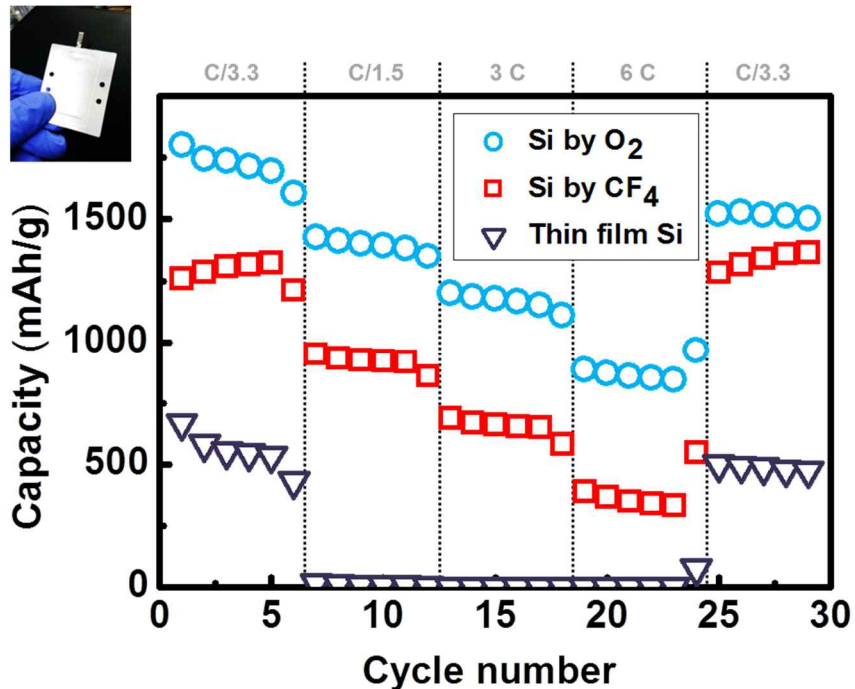


Figure 5.8. Rate capability test of Si on O₂-nano hairy PI, CF₄-nano hairy PI and pristine PI with a full-cell.

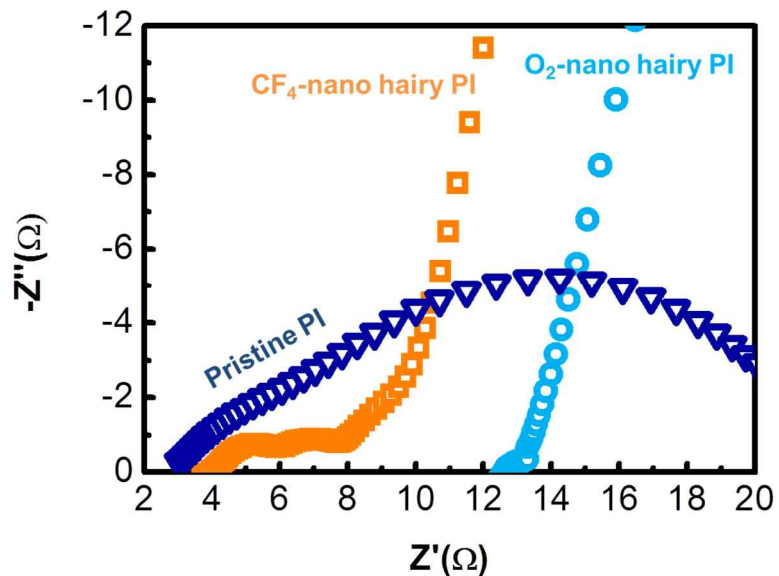


Figure 5.9. EIS results of Si on O_2 -nano hairy PI, CF_4 -nano hairy PI and pristine PI with a full-cell

5.3. Electrical modification of soft substrate

Recently, graphene-based electronics are intensively studied due to their excellent heat transports, conductivity, mechanical strength and even transparent properties.¹²⁷⁻¹³⁰ To fulfill the demands for electrically conductive polymer substrates, conductive reduced graphene oxide (R-GO) has triggered a wide range of application for flexible nanoelectronics, sensors, and super-capacitors.¹³¹ Pack *et al.* fabricated highly conductive reduced graphene oxide polymer composites by a well-organized thermochemical synthesis technique. The electrical conductivity of GO-based polymer composites can be further improved by heat treatment (~300 °C), as shown in Figure 5.10. Therefore, a polymer substrate, which is resistant to heat should be introduced. Among many polymer substances, as listed in Table 3.1, PI substrate is one of the most widely used and highly stable at high thermal conditions. Above all, PI substrate can acquire nano-hairy structures by plasma etching process. Therefore, conductive PI was used in the current research for battery application.

Conductive PI can have different conductivities depending upon the density of GO in the composite, provided by Korea Institute of Science and Technology (KIST) (Figure 5.11 (a)). Fig. 5.11 (b) shows a conductivity plot of GO-PI samples, Ag (known for very high conductivity among the metals), and (de) lithiated Si. Generally, the minimum barrier of conductivity for actual applications should be beyond 1 S/cm. The given samples are even below this limit and are not appropriate for conventional electronics. However, we tried to investigate and suggest the guidelines for fabric or polymer composite based electronics. Since, they have very poor conductivity so practically they are not useful for battery applications. Recently,

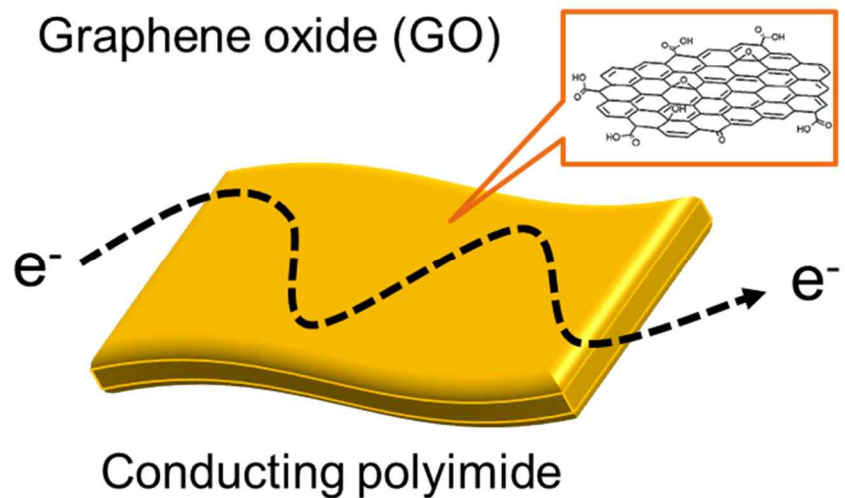


Figure 5.10. Graphene oxide (GO) dispersed in conductive polymer composites.

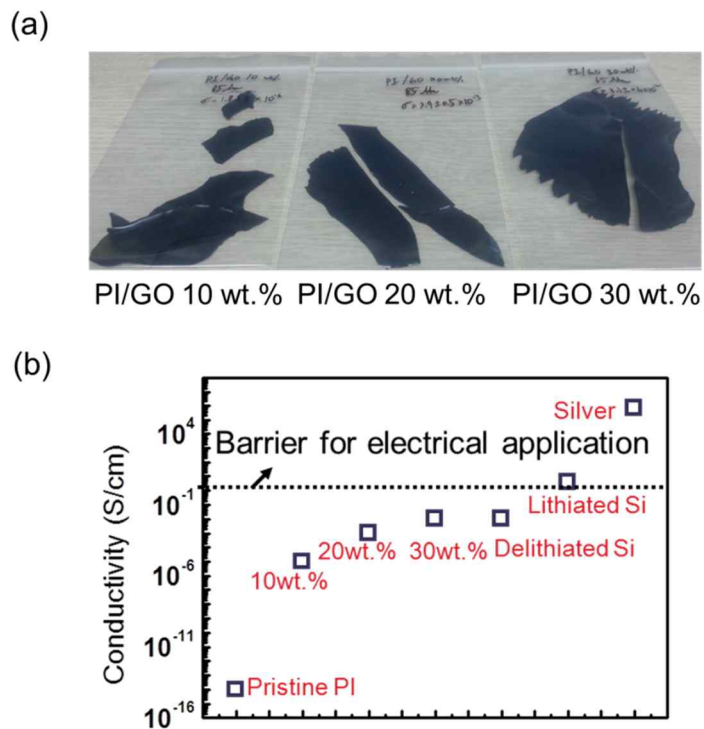


Figure 5.11. (a) conductive PI having different conductivity controlled by GO (b) conductivity of various materials and conductive PI with different GO portion.

wearable electronics are one of the highly rising research fields, so developing novel conducting polymers can open up the possibility of advancement of poorly conductive composite based electronics.

5.3.1. Enhancement of electrochemical performance

Nano-hairy structures on PI/GO (20 wt.%) and PI/GO (30 wt.%) was obtained by CF₄ gas plasma etching process, shown in Figure 5.12 (a) and (b), respectively and Si (300 nm) was deposited on these structures, shown in Fig. 5.12 (c) and (d). The morphologies were very similar to the aforementioned images on PI. Rate-capability test was performed to investigate the liming current value for charge and discharge process (Figure 5.13. (a)). When the C-rate was at C/7.3, charge/discharge for both the samples occurred, however, no electrochemical reaction started at higher C-rates. This implied that the cycling behavior is very dependent on conductivity. When conductivity was higher for PI/GO (30 wt.%), the corresponding capacity was also higher (nearly 1500 mAh/g) than that for PI/GO (20 wt.%), which was around 500 mAh/g at the C-rate of C/7.3. Direct evidence of this capacity difference can be viewed in Figure 5.13 (b), showing the sheet resistance for both the samples. The sheet resistance of PI/GO (30 wt.%) was approximately 30 times lower than that of PI/GO (20 wt.%), inducing a higher capacity.

After the test, the surface of the samples was investigated. With respect to the conductivity difference, the formation of SEI layer was differently identified. In PI/GO (20 wt.%), the nano-hairy PI with a relatively small amount of SEI layer can be observed (see Figure 5.14 (a)), whereas a SEI layer would severely cover the nano-hairy of PI/GO (30 wt.%), see (Figure 5.14 (b)). From this, it can be speculated that, the conductivity of

a substrate largely affects the formation rate of SEI layers, proving the electrically reaction sites. This is the main reason why our Cu deposited nano-hairy structures have micro-scale-thick SEI layer. Moreover, the tips of Si coated nano-hairs aggregated together due to the surface tension, which was further exposed to liquid electrolyte. These agglomerated morphologies could be easily observed in polymer nanostructures when they were subjected to liquid electrolyte to reduce the surface energy. The size of grain (agglomerated tips) of PI/GO (30 wt.%) was very similar to that of the PI/GO (30 wt.%) but has thicker SEI layers.

It can be understood that, the capacity is largely controlled by the conductivity difference with GO dispersed conductive polymer composites. Proper handling of low conductive substances, very slow steps of charge and discharge process are necessary. When a surface is electrically stable, a relatively thick layer of SEI is formed, which further forms group-like grains. For the surface tension, the tips of the nano hairs are aggregated each other, which are expected to be the same as the other nano-hairy structures used in this thesis.

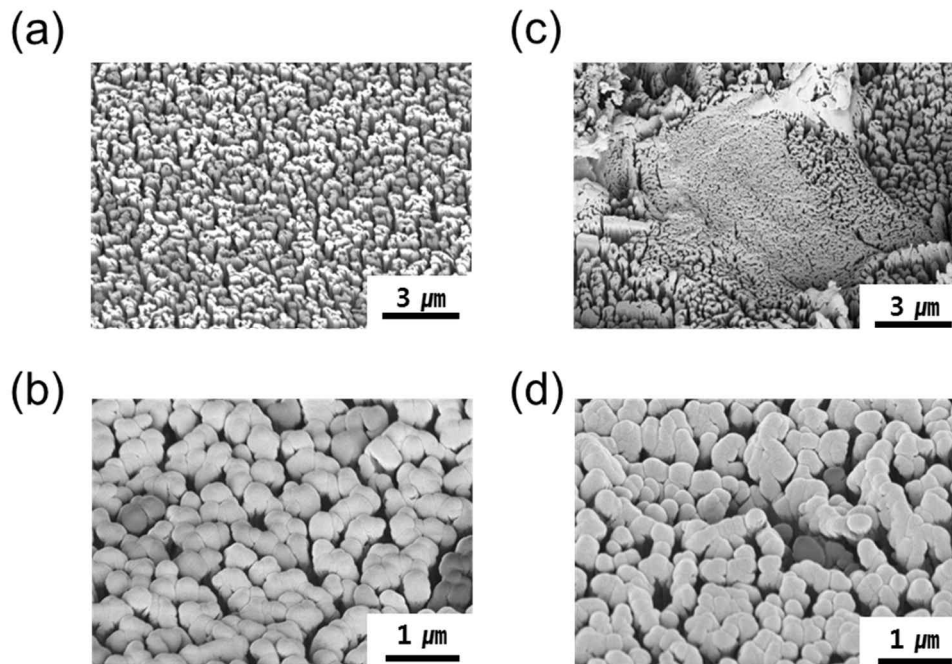


Figure 5.12. (a) Nano-hairy PI/GO (20 wt.%) by CF₄ plasma etching (b) Si deposition on (a) (c) Nano-hairy PI/GO (30 wt.%) by CF₄ plasma etching (d) Si deposition on (c)

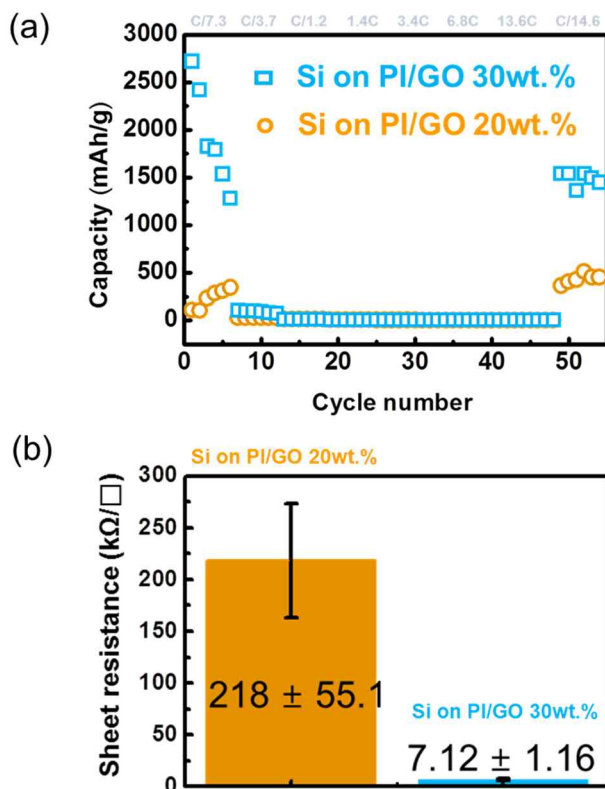


Figure 5.13. (a) Rate capability test for Si on nano-hairy PI/GO (20 wt.%) and PI/GO (30 wt.%) by CF_4 plasma etching (b) sheet resistance of both the samples

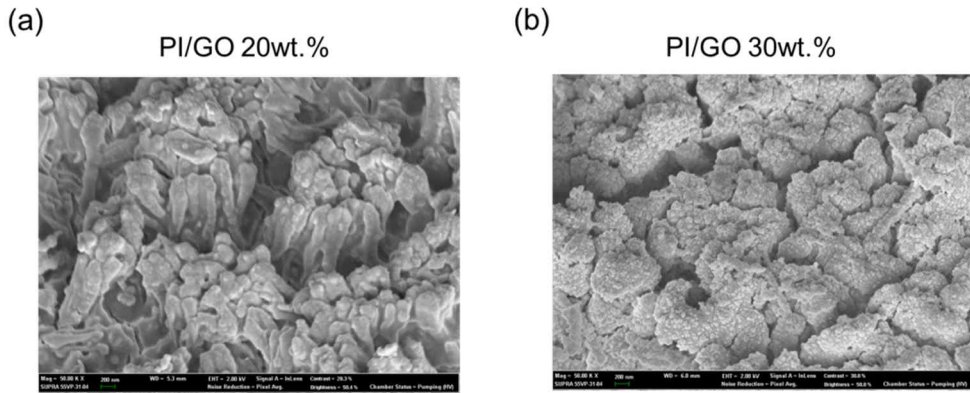


Figure 5.14. Surface morphologies after lithiation of (a) Si on nano-hairy PI/GO (20 wt.%) and PI/GO (30 wt.%).

5.4. Summary

In this chapter, the geometric and electrical characteristics of polyimide substrate were engineered. By introducing O₂ gas, nano-hairy PI was successfully obtained, with diameter 20-30 nm and length 1.8 μm . The aspect ratio of these nano-hairs was 60 compared to 10 of the nano-hairy PI etched by CF₄ gas. Through this structure, an improved electrochemical performance, higher capacity and excellent rate capability could be achieved. In cyclic bending fatigue test for Cu current collector, O₂-nano-hairy Cu displayed a lower change in electrical resistance than CF₄-nano-hairy and pristine PI under 4% strain condition. We also introduced graphene oxide (GO) dispersed conductive polymer composites, having conductivity less than 1 S/cm with respect to a portion of GO. From the results of electrochemical test, Si on nano-hairy conductive PI showed poor cycling performance at higher C-rate, however, the typical capacity of Si was observed in the lower C-rate region. With a higher conductivity of substrate, SEI layer can be thickly grown over the nano-hairy structure. These results give a deeper insight into fabric or polymer (with low conductivity) based Li-ion battery system and understand the limit of charge or discharge current.

CHAPTER 6

Conclusions

6.1. Summary of results

In the current research, we investigated the mechanical degradation of Si thin film anode after lithiation process. Due to a large compressive stress, catastrophic failures, such as circular buckles, telephone cord buckles, cracks and delaminations were generated on the surface. The built up stress (1~1.75 GPa), from the huge volume expansion of Si thin film was released through the various above-mentioned fracture morphologies. We focused on not only these fractures but also the mechanical properties of lithiated Si, e.g. the onset stress and the interface toughness. We analyzed the cross section of circular buckles and telephone cord buckle to measure the thickness. We also calculated the onset stress of both the circular (201 MPa) and telephone cord buckles (124 MPa) and then through statistical approaches estimated the interface toughness from the onset stress. We additionally conducted several measurements to obtain a representative value. The obtained interface toughness is 6.52 ± 0.14 for the circular buckles and 5.89 ± 0.27 for the telephone cord buckles. This interface toughness is close to the reported value in the literature ($5.4 \pm 2.2 \sim 6.9 \pm 1.9$).⁸² The current research

contributes positively to practical designing of Si anode and fracture modeling of lithiated Si.

From this failure analysis, we realized the importance of adhesion between the active material and the substrate. We also compared the characteristics of nanostructured Si on polyimide substrate with those of Si thin film. From the *in-situ* technique, we verified the lithiaion process of nano-hairy amorphous Si, revealing that no mechanical fracture and strain accommodation had occurred. In the half cell test, the nano-hairy Si showed a better cycling performance than the Si thin film. From the mechanical perspective, uniform cracks were formed on the SEI layer of the nano-hairy Si to alleviated the intrinsic stress. An interesting finding in this context is that, the length of the generated micro-cracks are below the critical delamination length, preventing any peel off. This prevented the delamination events, inducing a longer cycling and a higher capacity. Furthermore, we observed a partially peeled off edge delamination between Cu and the PI interface, which signified that the adhesion strength between Si and Cu in the thin film on the PI substrate had improved. Nano-hairy Si anode has a smaller charge transfer resistance and an easier Li⁺ ion diffusion process than that of a Si thin film on pristine PI, resulting in a higher capacity and an excellent rate capability. In addition to this, mechanical resistance is also evaluated for the cyclic deformation with a 2% strain from the current collector level to full pouch battery. Cu on nano-hairy PI showed very stable electric behavior with only less than 10% resistance change compared to over 300% of Cu on pristine PI upto 500,000 cycles. We successfully turned on the back light unit and maintained a voltage of 3.7 V under 3000 bending cycles with a 16mm-bending radius. Even, excellent C-rate was observed under such bent state.

For further improvement of the electrochemical and the mechanical properties, we modified the geometric and electrical characteristics of the polyimide substrate. By

introducing O₂ gas, we successfully obtained very thin (20~30 nm of diameter) and long (approximately 1.8 μm) nano-hairy PI, with an aspect ratio of 60 compared to 10 of the nano-hairy PI etched by CF₄ gas. At this aspect ratio, it was possible to achieve an improved electrochemical performance, higher capacity and excellent rate capability. In the cyclic bending fatigue test for the Cu current collector, O₂-nano-hairy Cu showed a lower change in electrical resistance than the CF₄-nano-hairy and pristine PI under 4% strain condition. We also introduced graphene oxide (GO) dispersed conductive polymer composites having conductivity less than 1 S/cm with respect to a portion of GO. The results of the electrochemical test showed that, Si on nano-hairy conductive PI exhibited a poor cycling performance at higher C-rate but a typical capacity of Si was observed in the lower C-rate region. For a substrate with a higher conductivity, the SEI layer can be thickly grown over the nano-hairy structure. These results allows one to know the limit charge or the discharge current for a fabric or polymer (with low conductivity) based Li-ion battery system.

In conclusion, a new bendable Li-ion battery system has been developed on a polymer substrate with an improvement in the mechanical robustness of the system. The volume-change induced stress and deformation induced stress could also be controlled via the inter space between the nano-hairy structures and uniform micro-cracking. We believe that this new structure can be applied not only to a Si anode but also to other alloying type of anode electrodes, and can open up new applications of batteries.

6.2. Future work and suggested research

In this study, we estimated the interface toughness of lithiated Si on Cu current collector through the circular buckles and telephone cord buckles initiated under the compressive stress by lithium insertion. A careful analysis of these failures revealed that the width of these failures were not very uniform, implying that they were initiated upon dynamic conditions having different stress rate. This is possibly due to different amount of Li inserted into the Si thin film. Therefore, it is necessary to keep the amount of Li balanced with the very slow lithiation process so that reaction between Li and Si takes place all over the area equally. Dependence of charge and discharge rate is another factor to induce different level of intrinsic stress or not. The nano-hairy structure can be applied to various alloying type of anodes and even cathode materials to accommodate the intrinsic and the extrinsic stresses. For practical purposes, the loading mass should be improved so that graphene-based anodes can also be considered equally. With respect to conductive polymer composites, we showed the possible operating conditions in spite of low conductivity. Improvement of conductivity by increasing the amount of graphene oxide is challenging.

Reference

- (1) Ziebarth, J. M.; Saafir, A. K.; Fan, S.; McGehee, M. D. *Adv. Funct. Mater.* **2004**, *14*, 451–456.
- (2) Sekitani, T.; Zschieschang, U.; Klauk, H.; Someya, T. *Nat. Mater.* **2010**, *9*, 1015–1022.
- (3) Takei, K.; Takahashi, T.; Ho, J. C.; Ko, H.; Gillies, A. G.; Leu, P. W.; Fearing, R. S.; Javey, A. *Nat. Mater.* **2010**, *9*, 821–826.
- (4) ABAD, E.; ZAMPOLLI, S.; MARCO, S.; SCORZONI, A.; MAZZOLAI, B.; JUARROS, A.; GOMEZ, D.; ELMI, I.; CARDINALI, G.; GOMEZ, J. *Sensors Actuators B: Chem.* **2007**, *127*, 2–7.
- (5) Heikenfeld, J.; Drzaic, P.; Yeo, J.-S.; Koch, T. *J. Soc. Inf. Disp.* **2011**, *19*, 129–156.
- (6) Chen, Y.-Y.; Lai, H.-Y.; Lin, S.-H.; Cho, C.-W.; Chao, W.-H.; Liao, C.-H.; Tsang, S.; Chen, Y.-F.; Lin, S.-Y. *J. Neurosci. methods* **2009**, *182*, 6–16.
- (7) Palacín, M. R. *Chem. Soc. Rev.* **2009**, *38*, 2565–2575.
- (8) Winter, M.; Brodd, R. *J. Chem. Rev.* **2004**, *104*, 4245–4270.
- (9) Simon, P.; Gogotsi, Y. *Nat. Mater.* **2008**, *7*, 845–854.
- (10) Koo, M.; Park, K.-I.; Lee, S. H.; Suh, M.; Jeon, D. Y.; Choi, J. W.; Kang, K.; Lee, K. *J. Nano Lett.* **2012**, *12*, 4810–4816.
- (11) Hu, L.; Pasta, M.; Mantia, F. L.; Cui, L.; Jeong, S.; Deshazer, H. D.; Choi, J. W.; Han, S. M.; Cui, Y. *Nano Lett.* **2010**, *10*, 708–714.
- (12) Hu, L.; Choi, J. W.; Yang, Y.; Jeong, S.; La Mantia, F.; Cui, L.-F.; Cui, Y. *Proc. Natl. Acad. Sci.* **2009**, *106*, 21490–21494.
- (13) Nam, K. T.; Kim, D.-W.; Yoo, P. J.; Chiang, C.-Y.; Meethong, N.; Hammond,

- P. T.; Chiang, Y.-M.; Belcher, A. M. *science* **2006**, *312*, 885–888.
- (14) Hu, L.; Wu, H.; La Mantia, F.; Yang, Y.; Cui, Y. *Acs Nano* **2010**, *4*, 5843–5848.
- (15) Gwon, H.; Kim, H.-S.; Lee, K. U.; Seo, D.-H.; Park, Y. C.; Lee, Y.-S.; Ahn, B. T.; Kang, K. *Energy & Environ. Sci.* **2011**, *4*, 1277–1283.
- (16) Chen, J.; Liu, Y.; Minett, A. I.; Lynam, C.; Wang, J.; Wallace, G. G. *Chem. Mater.* **2007**, *19*, 3595–3597.
- (17) Morris, R. S.; Dixon, B. G.; Gennett, T.; Raffaelle, R.; Heben, M. J. *J. Power Sources* **2004**, *138*, 277–280.
- (18) Endo, M.; Kim, C.; Nishimura, K.; Fujino, T.; Miyashita, K. *Carbon* **2000**, *38*, 183–197.
- (19) Beaulieu, L. Y.; Eberman, K. W.; Turner, R. L.; Krause, L. J.; Dahn, J. R. *Electrochem. Solid-state Lett.* **2001**, *4*.
- (20) Beaulieu, L. Y.; Hatchard, T. D.; Bonakdarpour, A.; Fleischauer, M. D.; Dahn, J. R. *J. Electrochem. Soc.* **2003**, *150*.
- (21) Kasavajjula, U.; Wang, C.; Appleby, A. J. *J. Power Sources* **2007**, *163*, 1003–1039.
- (22) Maranchi, J. P.; Hepp, A. F.; Evans, A. G.; Nuhfer, N. T.; Kumta, P. N. *J. Electrochem. Soc.* **2006**, *153*.
- (23) Gohier, A.; Laïk, B.; Pereira-Ramos, J.-P.; Cojocaru, C. S.; Tran-Van, P. J. *Power Sources* **2012**, *203*, 135–139.
- (24) Evanoff, K.; Khan, J.; Balandin, A. A.; Magasinski, A.; Ready, W. J.; Fuller, T. F.; Yushin, G. *Adv. Mater.* **2012**, *24*, 533–537.
- (25) Chen, H.; Xiao, Y.; Wang, L.; Yang, Y. *J. Power sources* **2011**, *196*, 6657–6662.

- (26) Wang, B.; Li, X.; Zhang, X.; Luo, B.; Jin, M.; Liang, M.; Dayeh, S. A.; Picraux, S. T.; Zhi, L. *ACS Nano* **2013**, *7*, 1437–1445.
- (27) Wu, H.; Chan, G.; Choi, J. W.; Yao, Y.; McDowell, M. T.; Lee, S. W.; Jackson, A.; Yang, Y.; Hu, L.; Cui, Y. *Nat. Nanotechnol.* **2012**, *7*, 310–315.
- (28) Zhang, S.; Du, Z.; Lin, R.; Jiang, T.; Liu, G.; Wu, X.; Weng, D. *Adv. Mater.* **2010**, *22*, 5378–5382.
- (29) Takamura, T.; Ohara, S.; Uehara, M.; Suzuki, J.; Sekine, K. *J. Power Sources* **2004**, *129*, 96–100.
- (30) Xiao, X.; Liu, P.; Verbrugge, M. W.; Haftbaradaran, H.; Gao, H. *J. Power Sources* **2011**, *196*, 1409–1416.
- (31) Ryu, I.; Choi, J. W.; Cui, Y.; Nix, W. D. *J. Mech. Phys. Solids* **2011**, *59*, 1717–1730.
- (32) Liu, X. H.; Zhong, L.; Huang, S.; Mao, S. X.; Zhu, T.; Huang, J. Y. *ACS Nano* **2012**, *6*, 1522–1531.
- (33) Schmidt, V.; Wittemann, J. V.; Gösele, U. *Chem. Rev.* **2010**, *110*, 361–388.
- (34) Holmes, J. D. *Science* **2000**, *287*, 1471–1473.
- (35) Heitsch, A. T.; Fanfair, D. D.; Tuan, H.-Y.; Korgel, B. A. *J. Am. Chem. Soc.* **2008**, *130*, 5436–5437.
- (36) Menard, E.; Lee, K. J.; Khang, D.-Y.; Nuzzo, R. G.; Rogers, J. A. *Appl. Phys. Lett.* **2004**, *84*, 5398–5400.
- (37) Yoon, J.; Baca, A. J.; Park, S.-I.; Elvikis, P.; Geddes, J. B.; Li, L.; Kim, R. H.; Xiao, J.; Wang, S.; Kim, T.-H. *Nat. Mater.* **2008**, *7*, 907–915.
- (38) Jang, H.; Lee, W.; Won, S. M.; Ryu, S. Y.; Lee, D.; Koo, J. B.; Ahn, S.-D.; Yang, C.-W.; Jo, M.-H.; Cho, J. H. *Nano Lett.* **2013**, *13*, 5600–5607.
- (39) Lee, S.-K.; Jang, H.; Hasan, M.; Koo, J. B.; Ahn, J.-H. *Appl. Phys. Lett.*

2010, *96*.

- (40) Mack, S.; Meitl, M. A.; Baca, A. J.; Zhu, Z.-T.; Rogers, J. A. *Appl. Phys. Lett.* **2006**, *88*.
- (41) Kim, D.-H.; Ahn, J.-H.; Choi, W. M.; Kim, H.-S.; Kim, T.-H.; Song, J.; Huang, Y. Y.; Liu, Z.; Lu, C.; Rogers, J. A. *Science* **2008**, *320*, 507–511.
- (42) Obrovac, M. N.; Christensen, L. *Electrochem. Solid-state Lett.* **2004**, *7*.
- (43) The crystal structural evolution of nano si anode casused by lithium insertinon and extraction at RT, 2000.
- (44) Li, J.; Dahn, J. R. *J. Electrochem. Soc.* **2007**, *154*.
- (45) Hatchard, T. D.; Dahn, J. R. *J. Electrochem. Soc.* **2004**, *151*.
- (46) Okamoto, H. *J. Phase Equilibria Diffus.* **2009**, *30*, 118–119.
- (47) Limthongkul, P.; Jang, Y.-I.; Dudney, N. J.; Chiang, Y.-M. *Acta Mater.* **2003**, *51*, 1103–1113.
- (48) Zamfir, M. R.; Nguyen, H. T.; Moyen, E.; Lee, Y. H.; Pribat, D. *J. Mater. Chem.* **2013**, *1*, 9566.
- (49) Key, B.; Bhattacharyya, R.; Morcrette, M.; Seznéc, V.; Tarascon, J.-M.; Grey, C. P. *J. Am. Chem. Soc.* **2009**, *131*, 9239–9249.
- (50) Wang, J. W.; He, Y.; Fan, F.; Liu, X. H.; Xia, S.; Liu, Y.; Harris, C. T.; Li, H.; Huang, J. Y.; Mao, S. X. *Nano Lett.* **2013**, *13*, 709–715.
- (51) Kim, H.; Chou, C.-Y.; Ekerdt, J. G.; Hwang, G. S. *J. Phys. Chem. C* **2011**, *115*, 2514–2521.
- (52) Key, B.; Morcrette, M.; Tarascon, J.-M.; Grey, C. P. *J. Am. Chem. Soc.* **2010**, *133*, 503–512.
- (53) Sethuraman, V. A.; Chon, M. J.; Shimshak, M.; Winkle, N. V.; Guduru, P. R. *Electrochem. Commun.* **2010**, *12*, 1614–1617.

- (54) Sethuraman, V. A.; Chon, M. J.; Shimshak, M.; Srinivasan, V.; Guduru, P. R. *J. Power Sources* **2010**, *195*, 5062–5066.
- (55) Chon, M. J.; Sethuraman, V. A.; McCormick, A.; Srinivasan, V.; Guduru, P. R. *Phys. Rev. Lett.* **2011**, *107*.
- (56) Sethuraman, V. A.; Winkle, N. V.; Abraham, D. P.; Bower, A. F.; Guduru, P. R. *J. Power Sources* **2012**, *206*, 334–342.
- (57) Liu, X. H.; Zhang, L. Q.; Zhong, L.; Liu, Y.; Zheng, H.; Wang, J. W.; Cho, J.-H.; Dayeh, S. A.; Picraux, S. T.; Sullivan, J. P. *Nano Lett.* **2011**, *11*, 2251–2258.
- (58) Zhao, K.; Pharr, M.; Vlassak, J. J.; Suo, Z. *J. Appl. Phys.* **2011**, *109*.
- (59) Li, J.; Dozier, A. K.; Li, Y.; Yang, F.; Cheng, Y.-T. *J. Electrochem. Soc.* **2011**, *158*, 689.
- (60) Haftbaradaran, H.; Xiao, X.; Gao, H. *Model. Simul. Mater. Sci. Eng.* **2013**, *21*, 074008.
- (61) E Meyers, M. A.; Chawla, K. K. **2009**.
- (62) Freund, L. B.; Suresh, S. *Cambridge: Camb.* 750.
- (63) Anderson, T. L. *Fracture mechanics: fundamentals and applications*; CRC press, 2005.
- (64) Balint, D. S.; Hutchinson, J. W. *J. Appl. Mech.* **2001**, *68*, 725–730.
- (65) Yu, H.-H.; Hutchinson, J. W. *Int. J. Fract.* **2002**, *113*, 39–55.
- (66) Moon, M. W.; Jensen, H. M.; Hutchinson, J. W.; Oh, K. H.; Evans, A. G. *J. Mech. Phys. Solids* **2002**, *50*, 2355–2377.
- (67) Moon, M.-W.; Chung, J.-W.; Lee, K.-R.; Oh, K. H.; Wang, R.; Evans, A. G. *Acta Mater.* **2002**, *50*, 1219–1227.
- (68) Hutchinson, J. W.; Suo, Z. *Adv. Appl. Mech.* **1992**, *29*.
- (69) Hutchinson, J. W. *J. Mech. Phys. Solids* **2001**, *49*, 1847–1864.

- (70) Jensen, H. M.; Sheinman, I. *Int. J. Fract.* **2001**, *110*, 371–385.
- (71) Moon, M.-W.; Lee, K.-R.; Oh, K.-H.; Hutchinson, J. W. *Acta Mater.* **2004**, *52*, 3151–3159.
- (72) Yin, J. Mechanical self-assembly: science and applications, 2010.
- (73) Haftbaradaran, H.; Xiao, X.; Verbrugge, M. W.; Gao, H. *J. Power Sources* **2012**, *206*, 357–366.
- (74) Lee, K.-L.; Jung, J.-Y.; Lee, S.-W.; Moon, H.-S.; Park, J.-W. *J. Power Sources* **2004**, *129*, 270–274.
- (75) Suresh, S. *Fatigue of materials*; Cambridge university press, 1998.
- (76) Hasegawa, M.; Horie, K. *Prog. Polym. Sci.* **2001**, *26*, 259–335.
- (77) Boukamp, B. A. *J. Electrochem. Soc.* **1981**, *128*, 725.
- (78) Yu, C.; Li, X.; Ma, T.; Rong, J.; Zhang, R.; Shaffer, J.; An, Y.; Liu, Q.; Wei, B.; Jiang, H. *Adv. Energy Mater.* **2012**, *2*, 68–73.
- (79) McDowell, M. T.; Lee, S. W.; Ryu, I.; Wu, H.; Nix, W. D.; Choi, J. W.; Cui, Y. *Nano Lett.* **2011**, *11*, 4018–4025.
- (80) Liu, Y.; Chen, T. P.; Fu, Y. Q.; Tse, M. S.; Hsieh, J. H.; Ho, P. F.; Liu, Y. C. *J. Phys. D: Appl. Phys.* **2003**, *36*, 97.
- (81) Soni, S. K.; Sheldon, B. W.; Xiao, X.; Verbrugge, M. W.; Ahn, D.; Haftbaradaran, H.; Gao, H. *J. Electrochem. Soc.* **2012**, *159*, 38.
- (82) Pharr, M.; Suo, Z.; Vlassak, J. *J. Nano Lett.* **2013**, *13*, 5570–5577.
- (83) Kamiya, S.; Furuta, H.; Omiya, M. *Surf. Coatings Technol.* **2007**, *202*, 1084–1088.
- (84) Her, E. K.; Ko, T.-J.; Shin, B.; Roh, H.; Dai, W.; Seong, W. K.; Kim, H.-Y.; Lee, K.-R.; Oh, K. H.; Moon, M.-W. *Plasma Process. Polym.* **2013**, *10*, 481–488.
- (85) Gogolides, E.; Constantoudis, V.; Kokkoris, G.; Kontziamasis, D.;

Tsougeni, K.; Boulousis, G.; Vlachopoulou, M.; Tserepi, A. *J. Phys. D: Appl. Phys.* **2011**, *44*.

(86) Lee, Y. H.; Chen, M.-M. *J. Appl. Phys.* **1983**, *54*, 5966.

(87) Rosli, S. A.; Aziz, A. A.; Hamid, H. A. In *Semiconductor Electronics, 2006. ICSE'06. IEEE International Conference on*; 2006; pp. 856–860.

(88) Jansen, H.; de Boer, M.; Elwenspoek, M. In *Micro Electro Mechanical Systems, 1996, MEMS'96, Proceedings. An Investigation of Micro Structures, Sensors, Actuators, Machines and Systems. IEEE, The Ninth Annual International Workshop on*; 1996; pp. 250–257.

(89) Jansen, H.; de Boer, M.; Legtenberg, R.; Elwenspoek, M. *J. Micromechanics Microengineering* **1995**, *5*.

(90) Leitel, R.; Kaless, A.; Schulz, U.; Kaiser, N. *Plasma Process. Polym.* **2007**, *4*.

(91) Di Mundo, R.; Palumbo, F.; d'Agostino, R. *Langmuir* **2009**, *26*, 5196–5201.

(92) Kim, B. S.; Shin, S.; Shin, S. J.; Kim, K. M.; Cho, H. H. *Nanoscale Res. Lett.* **2011**, *6*, 1–10.

(93) Yin, J.; Wada, M.; Yamamoto, K.; Kitano, Y.; Tanase, S.; Sakai, T. *J. Electrochem. Soc.* **2006**, *153*, 472.

(94) Han, G.-B.; Ryou, M.-H.; Cho, K. Y.; Lee, Y. M.; Park, J.-K. *J. Power Sources* **2010**, *195*, 3709–3714.

(95) Han, G.-B.; Lee, J.-N.; Choi, J. W.; Park, J.-K. *Electrochimica Acta* **2011**, *56*, 8997–9003.

(96) Faulhaber, S.; Mercer, C.; Moon, M.-W.; Hutchinson, J. W.; Evans, A. G. *J. Mech. Phys. Solids* **2006**, *54*, 1004–1028.

(97) Hwang, T. H.; Lee, Y. M.; Kong, B.-S.; Seo, J.-S.; Choi, J. W. *Nano Lett.* **2012**, *12*, 802–807.

- (98) Qu, J.; Li, H.; Henry, J. J.; Martha, S. K.; Dudney, N. J.; Xu, H.; Chi, M.; Lance, M. J.; Mahurin, S. M.; Besmann, T. M.; Dai, S. *J. Power Sources* **2012**, *198*, 312–317.
- (99) Chockla, A. M.; Bogart, T. D.; Hessel, C. M.; Klavetter, K. C.; Mullins, C. B.; Korgel, B. A. *J. Phys. Chem. C* **2012**, *116*, 18079–18086.
- (100) Song, T.; Xia, J.; Lee, J.-H.; Lee, D. H.; Kwon, M.-S.; Choi, J.-M.; Wu, J.; Doo, S. K.; Chang, H.; Park, W. I.; Zang, D. S.; Kim, H.; Huang, Y.; Hwang, K.-C.; Rogers, J. A.; Paik, U. *Nano Lett.* **2010**, *10*, 1710–1716.
- (101) Cui, L.-F.; Ruffo, R.; Chan, C. K.; Peng, H.; Cui, Y. *Nano Lett.* **2008**, *9*, 491–495.
- (102) Maranchi, J. P.; Hepp, A. F.; Kumta, P. N. *Electrochim. Solid-state Lett.* **2003**, *6*, 198.
- (103) Guo, J.; Sun, A.; Chen, X.; Wang, C.; Manivannan, A. *Electrochimica Acta* **2011**, *56*, 3981–3987.
- (104) Kim, G.; Jo, C.; Kim, W.; Chun, J.; Yoon, S.; Lee, J.; Choi, W. *Energy & Environ. Sci.* **2013**, *6*, 2932.
- (105) Chan, C. K.; Ruffo, R.; Hong, S. S.; Cui, Y. *J. Power Sources* **2009**, *189*, 1132–1140.
- (106) Kim, S.-P.; Duin, A. C. T. van; Shenoy, V. B. *J. Power Sources* **2011**, *196*, 8590–8597.
- (107) Markovich, E.; Salitra, G.; Levi, M. D.; Aurbach, D. *J. Power sources* **2005**, *146*, 146–150.
- (108) Fu, L. J.; Endo, K.; Sekine, K.; Takamura, T.; Wu, Y. P.; Wu, H. Q. *J. Power Sources* **2006**, *162*, 663–666.
- (109) Aurbach, D.; Markovsky, B.; Weissman, I.; Levi, E.; Ein-Eli, Y.

Electrochimica Acta **1999**, *45*, 67–86.

- (110) Vetter, J.; Novak, P.; Wagner, M. R.; Veit, C.; Möller, K.-C.; Besenhard, J. O.; Winter, M.; Wohlfahrt-Mehrens, M.; Vogler, C.; Hammouche, A. *J. Power sources* **2005**, *147*, 269–281.
- (111) Kim, B.-J.; Cho, Y.; Jung, M.-S.; Shin, H.-A.-S.; Moon, M.-W.; Han, H. N.; Nam, K. T.; Joo, Y.-C.; Choi, I.-S. *Small* **2012**, *8*, 3300–3306.
- (112) Li, Q.; Kim, K.-S. *Proc. R. Soc. A: Math. Phys. Eng. Sci.* **2008**, *464*, 1319–1343.
- (113) Her, E. K.; Ko, T.-J.; Shin, B.; Roh, H.; Dai, W.; Seong, W. K.; Kim, H.-Y.; Lee, K.-R.; Oh, K. H.; Moon, M.-W. *Plasma Process. Polym.* **2013**, *10*, 401–401.
- (114) Kohandehghan, A.; Kalisvaart, P.; Kupsta, M.; Zahiri, B.; Amirkhiz, B. S.; Li, Z.; Memarzadeh, E. L.; Bendersky, L. A.; Mitlin, D. *J. Mater. Chem.* **2013**, *1*, 1600–1612.
- (115) Wang, W.; Kumta, P. N. *Acs Nano* **2010**, *4*, 2233–2241.
- (116) Gohier, A.; Laïk, B.; Kim, K.-H.; Maurice, J.-L.; Pereira-Ramos, J.-P.; Cojocaru, C. S.; Van, P. T. *Adv. Mater.* **2012**, *24*, 2592–2597.
- (117) Fan, Y.; Zhang, Q.; Lu, C.; Xiao, Q.; Wang, X.; kang Tay, B. *Nanoscale* **2013**, *5*, 1503–1506.
- (118) Chen, X.; Gerasopoulos, K.; Guo, J.; Brown, A.; Wang, C.; Ghodssi, R.; Culver, J. N. *ACS nano* **2010**, *4*, 5366–5372.
- (119) Bang, B. M.; Kim, H.; Song, H.-K.; Cho, J.; Park, S. *Energy & Environ. Sci.* **2011**, *4*, 5013–5019.
- (120) Liu, N.; Wu, H.; McDowell, M. T.; Yao, Y.; Wang, C.; Cui, Y. *Nano Lett.* **2012**, *12*, 3315–3321.
- (121) Chen, H.; Dong, Z.; Fu, Y.; Yang, Y. *J. Solid State Electrochem.* **2010**, *14*,

1829–1834.

- (122) Chan, C. K.; Patel, R. N.; O'Connell, M. J.; Korgel, B. A.; Cui, Y. *ACS nano* **2010**, *4*, 1443–1450.
- (123) Cho, Y. J.; Kim, H. S.; Im, H.; Myung, Y.; Jung, G. B.; Lee, C. W.; Park, J.; Park, M.-H.; Cho, J.; Kang, H. S. *J. Phys. Chem. C* **2011**, *115*, 9451–9457.
- (124) Ge, M.; Rong, J.; Fang, X.; Zhou, C. *Nano Lett.* **2012**, *12*, 2318–2323.
- (125) Nguyen, H. T.; Zamfir, M. R.; Duong, L. D.; Lee, Y. H.; Bondavalli, P.; Pribat, D. *J. Mater. Chem.* **2012**, *22*, 24618–24626.
- (126) Chen, X.; Gerasopoulos, K.; Guo, J.; Brown, A.; Wang, C.; Ghodssi, R.; Culver, J. N. *Adv. Funct. Mater.* **2011**, *21*, 380–387.
- (127) Geim, A. K. *science* **2009**, *324*, 1530–1534.
- (128) Eda, G.; Fanchini, G.; Chhowalla, M. *Nat. Nanotechnol.* **2008**, *3*, 270–274.
- (129) Geim, A. K.; Novoselov, K. S. *Nat. Mater.* **2007**, *6*, 183–191.
- (130) Wang, G.; Shen, X.; Yao, J.; Park, J. *Carbon* **2009**, *47*, 2049–2053.
- (131) Park, O.-K.; Hahm, M. G.; Lee, S.; Joh, H.-I.; Na, S.-I.; Vajtai, R.; Lee, J. H.; Ku, B.-C.; Ajayan, P. M. *Nano Lett.* **2012**, *12*, 1789–1793.

요약(국문초록)

최근 전자제품이 소형화, 고집적화됨에 따라 이를 구동하기위해 고용량 전극물질이 반드시 필요하다. 많은 음극 전극재중에서 합금 (alloying) 유형의 음극재료들이 현재 상용화된 음극전극보다 질량당, 부피당 용량이 높기 때문에 많은 관심을 받고있다. 하지만, 이런 합금유형의 음극재는 충방전과정에서 매우 큰 체적변화로부터 내부응력이 발생하는 단점을 가지고 있다. 이러한 내부응력은 기계적 열화현상을 유도함으로써 전기화학적 용량을 급격하게 저해하는 주요 원인이 된다. 리튬이온배터리가 구부림, 비틀림, 그리고 늘림과 같은 외부의 변형에 노출에도 기계적인 고장 (mechanical failure)을 유발한다. 그러므로 내,외부로 발생되는 응력을 잘 해소하는 것이 구부림이 가능한 리튬이온배터리의 성능을 향상시키는 방법이 된다.

본 연구에서는 가장 체적변화가 심하고 깨짐성이 강한 실리콘을 사용하였다. 그 이유는 가장 기계적 성질이 취약한 물질의 단점을 해결하게되면 그 밖의 다양한 음극재료도 바로 활용가능하기 때문이다.

실리콘 박막 음극전지의 충,방전과정으로부터 용량저하를 유발하는 버클(buckle), 박리와 같은 기계적인 failure가 발생하는 것을 관찰하였다. 그 중 버클에 대한 추가 분석을 통해 리튬 실리사이드와 구리 집전체와의 접착력이 원형버클로부터는 $6.52 \pm 0.14 \text{ J/m}^2$ 그리고 전화줄형 버클 (telephone cord buckle)로부터는 $5.89 \pm 0.27 \text{ J/m}^2$ 라는 것을 구하였다.

실리콘과 구리 집전체상의 접착력을 향상시킴과 동시에 내부, 외부응력을 효과적으로 해소하기위해서 폴리이미드 (polyimide, PI) 기판상에 나노사이즈의 머리털과 유사한 (nano-hairy) 구조를 도입하여 기계적으로 안정한 리튬이온전지용 실리콘 음극전극을 제작하였다. 실시간 리튬-실리콘간 반응을

통해 비결정질 실리콘의 충전양상을 파악하였다. 이 거동을 통해 충전시 실리콘의 체적변화가 실리콘 나노구조체간 이격공간과 폴리머 나노와이어의 유연한 성질로부터 효과적으로 완화되는 것을 확인하였다. 이를 반쪽전지 실험을 통해서 확인한 결과 이 구조가 박막형 전극에 비해 용량이 더 높고 수명이 긴 (100번째 cycle에서 1573 mAh/g) 싸이클링 거동을 확인할 수 있었다. 또한, 율속특성시험을 통해서도 전류변화에 대한 충,방전 용량이 높고 초기 용량으로의 회복율도 95% 가 될 정도로 우수하였다. 이는 나노실리콘 구조체를 덮고있는 SEI (solid-electrolyte interphase)층이 임계박리길이 미만의 일정한 균열 길이를 갖는 마이크로 사이즈의 크랙 (crack)을 형성하면서 내부의 응력을 효과적으로 해소하면서 박리를 예방하였기 때문이다.

변형 및 구부림이 가능한 전자제품에 탑재될 배터리로써의 적용에 앞서 본 구조를 채택한 구리 집전체와 풀셀 (full cell)의 기계적인 이동변형 및 반복굽힘에 따른 저항능력을 평가하였다. 나노사이즈의 머리털구조상의 구리 집전체는 500,000번의 싸이클에도 저항 증가율이 10% 미만으로 거의 변하지 않는 반면, 박막형 구리 집전체는 300% 넘는 저항 증가율을 보였다. 또한, 풀셀을 통한 3,000 번의 반복굽힘 평가 결과에서도 나노사이즈의 머리털구조에서는 충전된 3.7V가 열화현상 없이 지속적으로 유지됨을 확인하였다.

또한, 폴리이미드 기판의 구조적, 전기적 성질을 변화시킴으로써 전기화학적 및 기계적 측면에서의 거동을 살펴보았다. 산소 (O_2) 플라즈마 식각 공법을 통한 나노구조체가 사불화탄소 (CF_4) 플라즈마 식각 공법을 통한 나노구조체보다도 얇고 긴 종횡비율이 60이 되는 나노구조체를 얻을 수 있었다. 이의 전기화학적 성능평가를 실시한 결과, 기존의 성능보다 우수함을 확인하였는데 이는 표면적이 크게 증가하였기 때문으로 사료된다. 구리 집전체의 기계적 이동변형 시험에서도 보다 가혹한 조건(4% 변형률)에서 기존의 나노구조체보다도 낮은 증가폭의 저항증가율을 보였다. 또한, 그라핀 옥사이드가 분산된 전도성 폴리이미드 기판을

통해 집전체충을 생략하는 공정 조건을 형성하여 이의 전기화학적 성능을 평가한 결과 낮은 충방전 전류조건에서는 기존과 유사한 거동을 보임을 확인하였으나 높은 충방전 전류조건에서는 충방전이 잘 되지 않는 것을 확인하였다. 이는 전도성 폴리머 기판의 전기전도도가 1 S/cm 미만으로 매우 낮기 때문이다. 그러나 이는 오히려 섬유기반 혹은 폴리머 기반의 전기전도도가 상대적으로 낮은 분야에서의 리튬이온전지의 한계 충방전 조건을 이해할 수 있는 척도라고 판단된다.

본 연구에서는 폴리머 기판상에 실리콘 음극을 직접 매립하여 기계적 변형(구부림)에서도 안정적인 전기화학적 거동을 보이는 리튬이온전지를 개발하였다. 이는 기존에 실리콘에서 보고되었던 다양한 기계적 열화현상이 새롭게 제안된 폴리머 나노구조체를 도입함으로써 효과적으로 개선되었기 때문이다. 이 나노구조체의 개발은 실리콘 음극재뿐만 아니라 큰 체적변화를 동반하는 합금유형의 어떤 음극재에도 적용 가능하게 하였다. 본 연구는 이를 통해 다양한 재료의 선택을 통해 폴리머 기판 기반의 배터리를 설계하는데에 큰 기여를 한 것으로 판단된다.

표제어: 실리콘 음극재, 플렉시블 배터리, 폴리머 나노스트럭처링, 굽힘 피로, 계면접착력

학 번: 2008-22861

Min-Suk Jung

Research area

Highly bendable battery electrodes using Silicon

Enhancement of metal electrodes for flexible devices

Design and fabrication of nano-structures of metals and polymers

Improvement of reliability for electrochemical migration

Publication

1. M.-S. Jung, J.-H. Seo, M. -W. Moon, J. -W. Choi, Y. C. Joo and I.- S. Choi, “Bendable Li-Ion Battery with Nano-Hairy Electrode: Direct Integration Scheme on Polymer Substrate, *Advanced Energy Materials*, under revision (2014)
2. M.-S. Jung, S. -B. Lee, H.-Y. Lee, C. -S. Ryu, Y. -G Ko, H. -W Park, and Y. C. Joo “Improvement of Electrochemical Migration Resistance by Cu/Sn Intermetallic Compound Barrier on Cu in Printed Circuit Board”, *IEEE TRANSACTIONS ON DEVICE AND MATERIALS RELIABILITY*, **14**, (2014), 382
3. B. -J. Kim, Y. -G. Jo, M.-S. Jung, H.-A.-S Shin, M. -W. Moon, H. -N. Han, K. -T. Nam., Y. C. Joo and I.- S. Choi, “Fatigue-Free, Electrically Reliable

- Copper electrode with Nanohole Array”, *small*, **21**, (2012), 3300
4. S. –B. Lee, H.-Y. Lee, **M.-S. Jung**, Y. –B Park, and Y. –C. Joo, Effect of the Composition of Sn-Pb Alloys on the Microstructure of Filaments and the Electrochemical Migration Characteristics, *Met. Mater. Int.*, **17**, (2011), 617
5. S. –B. Lee, **M.-S. Jung**, H.-Y. Lee, T. Kang, and Y. –C. Joo, “Effect of Bias Voltage on the Electrochemical Migration Behaviors of Sn and Pb”, *IEEE TRANSACTIONS ON DEVICE AND MATERIALS RELIABILITY*, **9**, (2009), 483

Presentation

1. **M.-S. Jung**, M.-W. Moon, J.-H. Seo. Y.-C. Joo, I.-S. Choi, “Robust Si anode design for Li-ion battery on polyimide substrate: villus-like polymer/si core/shell hybrid nanostructure”, Electrochemical Society, San Fransisco, USA (2013)
2. **M.-S. Jung**, H.-A.-S Shin, I.-S. Choi, “Directional and Aligned Growth of Metal Filament for Individual Wiring Using Electric Field”, International Symposium on Nature-Inspired Technology, Gangwon-do (2013)
3. **M.-S. Jung**, M.-W. Moon, J.-H. Seo. Y.-C. Joo, I.-S. Choi, “Nature-inspired Robust Si Anode Design for Li-ion Battery on Polyimide substrate: Polymer/Si Core/Shell Hybrid Nanohairy Structure”, Korean Conference on Semiconductors, Jeju (2013)
4. **M.-S. Jung**, M.-W. Moon, Y.-C. Joo, I.-S. Choi, “Novel Nanostructured Si

anode Behavior on Nanorod Array Polymer Substrate”, Electrochemical society, Hawaii (2012)

5. **M.-S. Jung**, M.-W. Moon, Y.-C. Joo, I.-S. Choi, “Novel Nanostructured Si anode on Nanorod Array Polymer Substrate”, The Korean Institute of Metals and Materials, Chang-Won, Korea (2012)

6. **M.-S. Jung**, M.-W. Moon, Y.-C. Joo, I.-S. Choi, “Nanostructured Si anode Behavior on Nanorod Array Polymer Substrate”, The Korean Institute of Metals and Materials, Heongsung, Korea (2012)

7. **M.-S. Jung**, S.-B. Lee, R. Prasad, I.-S. Choi, Y.-C. Joo “Functional Nanostructured Filament Grown by Electrochemical Migration Method &Electroplating”, Boston, USA (2011)

8. **M.-S. Jung**, S.-B. Lee, H.-Y. Lee, C. –S. Ryu, Y.-G. Ko, H.-S. Min, Y.-C. Joo, “Alternative Surface Finish of Electrochemical Migration Resistance by Very Thin Sn Coating on Cu in Printed Circuit Board”, The Korean Microelectronics and Packaging Society, Jeju, Korea (2011)

9. **M.-S. Jung**, J. –H. Lee, S.-B. Lee, H.-Y. Lee, C. –S. Ryu, Y.-G. Ko, H.-S. Min, Y.-C. Joo, “Improvement of Electrochemical Migration Resistance by Immersion Sn Coating on Cu electrode in Printed Circuit Board”, Electrochemical society, Vancouver, USA (2010)

10. **M.-S. Jung**, J. –H. Lee, S.-B. Lee, H.-Y. Lee, C. –S. Ryu, Y.-G. Ko, H.-S. Min, Y.-C. Joo, “Improvement of Electrochemical Migration Resistance by

Inter-metallic Compound Barrier on Cu Electrode in Printed Circuit Board”,
Korean Conference on Semiconductors, Daegu, (2010)

11. **M.-S. Jung**, S.-B. Lee, H.-Y. Lee, Y.-C. Joo, “Electrochemical Migration Resistance for Cu Electrode by Sn Barrier on Printed Circuit Board”, The Korean Microelectronics and Packaging Society, Seoul, Korea (2009)

12. **M.-S. Jung**, S.-B. Lee, H.-Y. Lee, Y.-C. Joo, “Improvement of Electrochemical Migration Resistance of Cu Electrode by Protective Sn Coating for Printed Circuit Board”, The Korean Institute of Metals and Materials, Chang-Won, Korea (2009)

Patent

1. **M.-S. Jung**, M.-W. Moon, Y.-C. Joo, I.-S. Choi, “Anode electrode for secondary battery and method of manufacturing the same”, PCT(USA), Korea, 1020140052579

2. **M.-S. Jung**, B.-J. Kim, M.-W. Moon, Y.-C. Joo, I.-S. Choi, “Member for flexible device and method of fabricating the same”, PCT(USA), Korea, 1020120118694

3. **M.-S. Jung**, M.-W. Moon, S.-H. Lee, Y.-C. Joo, I.-S. Choi, “Anode of lithium secondary battery and manufacturing method thereof”, Korea, 1011873470000

4. **M.-S. Jung**, H.-W. Park, S.-B. Lee, H.-Y. Lee, C. -S. Ryu, Y.-G. Ko, H.-S. Min, Y.-C. Joo, “Printed circuit substrate and method of manufacturing the

same”, USA, Japan, Korea, 101097670000